



Title	Fragmentation of Primordial Filamentary Clouds Under Far-Ultraviolet Radiation
Author(s)	Bessho, Shinji
Citation	大阪大学, 2012, 博士論文
Version Type	VoR
URL	<a href="https://hdl.handle.net/11094/27470">https://hdl.handle.net/11094/27470</a>
rights	
Note	

*The University of Osaka Institutional Knowledge Archive : OUKA*

<https://ir.library.osaka-u.ac.jp/>

The University of Osaka

Fragmentation of Primordial  
Filamentary Clouds Under  
Far-Ultraviolet Radiation

Shinji Bessho

Department of Earth Space Science

Graduate School of Science

Osaka University, Osaka, JAPAN

1-1 Machikaneyama-cho, Toyonaka, Osaka, 560-0043, Japan

[bessho@vega.ess.sci.osaka-u.ac.jp](mailto:bessho@vega.ess.sci.osaka-u.ac.jp)

Submitted : November 2012

Fragmentation of Primordial  
Filamentary Clouds Under  
Far-Ultraviolet Radiation

(紫外線照射下での棒状ガス雲の分裂)

# Abstract

Filamentary clouds are one of the possible origins of stars and other astronomical objects. A filamentary cloud is expected to fragment into multiple clouds. These clouds are expected to become stars or other astronomical objects. In this thesis, we investigate the collapse and fragmentation of the primordial filamentary clouds under external radiation. Especially, the impact of photodissociation of hydrogen molecules in the collapsing cloud is investigated.

First, we use one-zone model. Dynamical and thermal evolution of the collapsing filamentary clouds is calculated by solving the virial equation and energy equation taking into account non-equilibrium chemical reactions. We assume that the filamentary cloud fragments when the timescale of density evolution becomes longer than the timescale of fragmentation. We also assume that the external radiation turns on when the filamentary cloud forms. With the external radiation, for the filamentary cloud with moderate line mass and with low initial density ( $n_0 \leq 10^2 \text{cm}^{-3}$ ), cooling is negligible since main coolant, hydrogen molecules, is photodissociated. In this case, temperature increases to suppress the collapse in the early stage, and the filamentary cloud fragments into very massive clouds ( $\sim 10^{4-5} M_\odot$ ). Thermal evolution of the filamentary cloud with high initial density ( $n_0 > 10^2 \text{cm}^{-3}$ ) is found to be hardly affected by the external dissociating radiation. This is because the filamentary cloud with high initial density shields itself from the external radiation. In such a case, fragment mass is smaller ( $\leq 500 M_\odot$ ) than the case with low initial density. We also derive analytic criterion for the filamentary clouds to fragment into very massive clouds.

Second, we investigate collapse and fragmentation by using the one-dimensional model. We

solve the hydrodynamical equation with respect to the radial direction instead of the virial equation in the one-zone model. As a result, it is also found that very massive fragments ( $\sim 10^{4-5}M_{\odot}$ ) forms in the case with low initial density ( $n_0 \leq 10^2\text{cm}^{-3}$ ) as in the one-zone model. Hence, formation of very massive fragments can be regarded as a robust result.

It is found that fragment mass becomes smaller under the external dissociating radiation in the cases with line mass large enough to collapse without fragmentation during adiabatic phase. However, when the filamentary cloud fragments during adiabatic phase, fragment mass becomes larger under the external dissociating radiation.

# Contents

<b>Abstract</b>	<b>i</b>
<b>Acknowledgements</b>	<b>vi</b>
<b>1 Introduction</b>	<b>1</b>
<b>2 Model for the filamentary clouds</b>	<b>7</b>
2.1 Basic equations . . . . .	7
2.2 External radiation . . . . .	9
2.3 Condition for fragmentation of the filamentary cloud . . . . .	12
2.4 Parameters and initial conditions . . . . .	14
<b>3 Numerical results I : uniform one-zone model</b>	<b>17</b>
3.1 Numerical results . . . . .	17
3.1.1 Cases without the external radiation . . . . .	17
3.1.2 Cases with the external radiation . . . . .	21
3.1.3 Fragment mass . . . . .	27
3.2 Analytic investigation . . . . .	27
3.2.1 Cooling criterion 1 : whether cooling is effective or not . . . . .	28
3.2.2 Equilibrium fraction of $H_2$ . . . . .	29

3.2.3	Cooling criterion 2 : whether cooling becomes effective when formation and photodissociation of H <sub>2</sub> balance . . . . .	30
3.2.4	Cooling criterion 3 : whether cooling is effective with adiabatically increasing temperature . . . . .	31
3.3	Discussion . . . . .	32
3.4	Summary of uniform one-zone model . . . . .	33
3.5	Problem of uniform one-zone model . . . . .	34
<b>4</b>	<b>Numerical results II : rarefied filament model</b>	<b>37</b>
4.1	Modification to the model . . . . .	38
4.2	Numerical results . . . . .	38
4.2.1	Cases without the external radiation . . . . .	38
4.2.2	Case with the external radiation . . . . .	40
4.2.3	Fragment mass . . . . .	42
4.3	Summary of the rarefied filament model . . . . .	43
4.4	Problems of rarefied filament model . . . . .	45
<b>5</b>	<b>Numerical results III : one-dimensional model</b>	<b>47</b>
5.1	Modification to the model . . . . .	47
5.1.1	Basic equations . . . . .	47
5.1.2	External radiation . . . . .	49
5.1.3	Fragmentation of the filamentary cloud . . . . .	49
5.1.4	Parameters and initial conditions . . . . .	50
5.2	Numerical results . . . . .	50
5.2.1	Cases without the external radiation . . . . .	50
5.2.2	Cases with the external radiation . . . . .	54
5.2.3	Property of the filamentary cloud at fragmentation . . . . .	58
5.2.4	Fragment mass . . . . .	61

5.3	Summary of the one-dimensional model . . . . .	64
5.4	One unresolved question . . . . .	65
<b>6</b>	<b>Criterion for increase of fragment mass</b>	<b>67</b>
6.1	Whether the filament reaches the loitering point . . . . .	67
6.2	Effect of sub-fragmentation . . . . .	70
6.3	Summary . . . . .	71
6.4	Discussion . . . . .	72
6.4.1	Application to cosmological simulation . . . . .	72
6.4.2	Thermal evolution of filament and sphere after the loitering point . . .	72
<b>7</b>	<b>Conclusions</b>	<b>75</b>
<b>A</b>	<b>On the formation and fragmentation of the filamentary cloud</b>	<b>77</b>
A.1	The density profile and line mass of the isothermal equilibrium filamentary cloud	77
A.2	Formation of the filamentary cloud . . . . .	80
A.2.1	Density perturbation . . . . .	80
A.2.2	Sheet-like cloud . . . . .	80
A.3	Dispersion relation for the filamentary cloud . . . . .	83
<b>B</b>	<b>Line cooling and Continuum processes</b>	<b>87</b>
B.1	H lines . . . . .	87
B.2	H <sub>2</sub> lines . . . . .	89
B.3	HD lines . . . . .	90
B.4	Continuum processes . . . . .	90
B.4.1	Bound-Free Absorption and Free-bound Emission(a1 – a4, a9 – a12) . .	91
B.4.2	Free-Free Absorption/Emission(a5, a6) . . . . .	93
B.4.3	H <sub>2</sub> Collision-Induced Absorption/Emission(a7, a8) . . . . .	94
B.4.4	Scattering(s1, s2) . . . . .	94

<b>C</b>	<b>The effect of radiative transfer in the uniform filamentary cloud</b>	<b>95</b>
<b>D</b>	<b>Mean intensity of the external radiation</b>	<b>97</b>
	D.1 Model . . . . .	97
	D.2 The UV flux at a halo . . . . .	99
	D.3 Results . . . . .	100
<b>E</b>	<b>The integral value of Eq.(2.15)</b>	<b>103</b>
<b>F</b>	<b>Self-shielding factor</b>	<b>105</b>
<b>G</b>	<b>Test of numerical code for one-dimensional hydrodynamical calculations</b>	<b>109</b>
<b>H</b>	<b>Self-shielding function of Wolcott-Green et al. (2011)</b>	<b>111</b>
<b>I</b>	<b>Virial equation for uniform sphere</b>	<b>113</b>
	<b>Bibliography</b>	<b>117</b>

# Acknowledgements

I would like to extend my gratitude to Assistant Professor Toru Tsuribe for useful discussions. I could not have completed my work and written this thesis without his support. I also thank Professor Fumio Takahara for fruitful discussions and continuous encouragements, the present and past members of the Theoretical Astrophysics Group in the Osaka University for fruitful discussions and pleasant talks, and my family and friends for supporting me throughout my life.

# Chapter 1

## Introduction

It is accepted that the density perturbations collapse and cool due to hydrogen molecules ( $\text{H}_2$ ) to form so-called population III (pop III) stars (Bromm et al. 1999, 2002; Abel et al. 2000, 2002; Yoshida et al. 2008). Pop III stars are expected to form in pregalactic clouds with a typical mass  $\sim 10^6 M_\odot$  (Tegmark et al. 1997). If popIII star is a massive star, it is expected to cause feedbacks via supernovae and radiation. The former may spread metals made by nuclear fusion and sweep the neighboring gas by shock (e.g., Heger et al. 2003). As the latter, there are two types of the radiative feedbacks, which are ionization and dissociation (Whalen et al. 2004; Susa et al. 2009; Hasegawa et al. 2009a, 2009b). Ionization of hydrogen atoms (H) provides strong heating which causes evaporation of clouds. However, due to large opacity, ionizing photons tend to be prevented from spreading, and photoionization would occur mainly within halos. On the other hand, photodissociation of  $\text{H}_2$  would occur even out of halos (Kitayama et al. 2004). Thus, it is expected that there are some regions which are not photoionized but photodissociated. We investigate gravitational collapse and fragmentation of primordial clouds in such a region.

Since  $\text{H}_2$  is main coolant in the early universe, if  $\text{H}_2$  molecules are photodissociated, a collapsing primordial cloud loses its cooling ability and it heats adiabatically up to high temperature ( $\sim 10^4\text{K}$ ) where atomic cooling becomes effective. In such a case, it is suggested that

high mass objects ( $\sim 10^{4-5} M_{\odot}$ ) may form since the Jeans mass ( $M_J \propto T^{3/2} \rho^{-1/2}$ ) is large (e.g., Bromm & Loeb 2003). However, the collapsing cloud is possible to fragment into many smaller clumps to form a star cluster when cloud suffers photodissociation of  $H_2$  (Omukai & Yoshii 2003). Whether mass of stars and astronomical object becomes larger or smaller under the dissociating radiation is still open question. In order to understand the actual final outcome and their initial mass function, detailed investigations of thermal and dynamical evolution of collapsing clouds are required.

The evolution of spherical clouds under the external dissociating radiation was investigated by Omukai (2001). He calculated the evolution of the central region of a collapsing sphere, assuming free-fall collapse. Starting from  $n_0 = 8.9 \times 10^{-2} \text{cm}^{-3}$ , the cloud collapses adiabatically in the early stage,  $n \leq 10^2 \text{cm}^{-3}$ . After this stage, thermal evolution of the cloud is divided into two types of tracks. When the external radiation is very strong (e.g, with the intensity larger than  $10^{-18} \text{erg cm}^{-2} \text{s}^{-1} \text{Hz}^{-1} \text{sr}^{-1}$  at 13.6eV for thermal radiation of  $10^4 \text{K}$ ),  $H_2$  is photodissociated enough to suppress  $H_2$  cooling. In this case, main coolant is provided by hydrogen atom. On the other hand, if the intensity of the external radiation is moderate, sufficient amount of  $H_2$  forms and it shields itself from the external radiation (photodissociation rate is proportional to column density of  $H_2$  to  $-0.75$ th power). The cloud cools mainly through  $H_2$  cooling. Susa (2007) investigated more realistic evolution of a spherical cloud under the UV radiation from a single light source with three-dimensional calculations. He investigated whether or not clouds collapse for parameters such as the distance from the light source and the density when the light source turns on.

As for formation of the spherical clouds investigated above, a filamentary cloud is a possible origin. Filamentary clouds are commonly expected during the way to form the stars. For example, when sheet-like cloud forms, the sheet-like cloud tends to fragment into the filamentary clouds (Miyama et al. 1987a, b). In cosmological simulations of first star formation, the filamentary structure often forms from density perturbation with  $\geq 10^6 M_{\odot}$  (Abel et al. 1998; Bromm et al. 1999; Greif et al. 2008). These filamentary clouds are expected to produce

spherical clouds by fragmentation (Nagasawa 1987; Inutsuka & Miyama 1997)<sup>1</sup>. Thus, in order to understand the origin and property of a collapsing spherical cloud, it is useful to investigate the evolution of the filamentary clouds. Previous works about fragmentation of the primordial filamentary clouds include one-zone models (Uehara et al. 1996; Flower 2002; Omukai & Yoshii 2003) and one-dimensional models (Nakamura & Umemura 1999, 2001, 2002; Uehara & Inutsuka 2000). Among these studies, Uehara et al. (1996), Omukai & Yoshii (2003), and Nakamura & Umemura (1999, 2001) considered only H<sub>2</sub> as a coolant, and the others considered deuterated hydrogen molecules (HD) as well as H<sub>2</sub>. If the initial fraction of H<sub>2</sub> is lower than 10<sup>-3</sup>, H<sub>2</sub> becomes main coolant and fragment mass is 1 – 500M<sub>⊙</sub>. On the other hand, if the initial fraction of H<sub>2</sub> is higher than 3 × 10<sup>-3</sup>, the filamentary cloud with low initial density ( $n_0 < 10^4 \text{cm}^{-3}$ ) cools mainly owing to HD cooling since H<sub>2</sub> promotes formation of HD with higher cooling rate. In this case, fragment mass is 1 – 140M<sub>⊙</sub>. When HD becomes main coolant, the filamentary clouds cool down to lower temperature (e.g., ~ 40K) and fragment into less massive fragments than when H<sub>2</sub> is main coolant. However, all of these previous papers except for Omukai & Yoshii (2003) did not consider the effect of the external dissociating radiation.

Omukai & Yoshii (2003) investigated fragmentation of the filamentary cloud under UV radiation using a one-zone model. Based on the results by Nakamura & Umemura (2001), they assumed that the filamentary cloud fragments when its density becomes 100 times higher than the loitering point where temperature is a local minimum in  $\rho - T$  plane owing to H<sub>2</sub> cooling. The filamentary cloud needs higher density in order to shield itself from the stronger external radiation. Thus, the density at the loitering point is higher with the stronger radiation. They concluded that the fragment mass is smaller under the stronger UV radiation. However, the condition for fragmentation given by Nakamura & Umemura (2001) was considered for the cases without the external radiation. Thus, it is not clear that this condition for fragmentation is applicable to the case with the external dissociating radiation. Furthermore,

---

<sup>1</sup>As for formation and fragmentation, we review in Appendix A.

if the filamentary cloud loses enough amount of  $\text{H}_2$  owing to photodissociation, temperature increases and pressure gradient force is expected to become stronger. In such a case, dynamical time is expected to become longer than the timescale of fragmentation, and fragmentation is possible to occur during efficiently adiabatic phase. Thus, fragment mass is expected to become larger under the external radiation. However, Omukai & Yoshii (2003) did not consider this possibility.

In this thesis, we investigate the effect of photodissociating radiation on the thermal and dynamical evolution of the collapsing filamentary cloud and on the resulting fragment mass. We investigate whether or not the external radiation increases fragment mass. Instead of assuming free-fall collapse as Omukai & Yoshii (2003), we treat the pressure effect explicitly by solving the virial equation or one-dimensional hydrodynamics taking into account the effect of pressure gradient force. This is important especially with the insufficient cooling as a result of efficient photodissociation. As for the condition for fragmentation, we assume that the filamentary cloud fragments when the timescale of fragmentation becomes shorter than the timescale of density evolution. Previous and our studies are summarized in Table.1.1 and 1.2.

We consider the simplest case where the dissociating radiation is isotropic. As for the intensity of the external radiation originating from halos forming pop IIIs, we refer to the result by Dijkstra et al. (2008) who investigated the mean intensity of the external dissociating radiation in the universe at redshift  $z \sim 10$ . We assume that the external radiation turns on when the filamentary cloud forms ( $n \geq 10\text{cm}^{-3}$ ) in Chapters 3, 4 and 5.

We explain model for the filamentary cloud in Chapter 2. In Chapter 3 and 4, we investigate collapse and fragmentation of the primordial filamentary cloud under the external radiation with one-zone models. In Chapter 5, we investigate with one-dimensional model. In Chapter 6, we discuss the origin of difference between our results and Omukai & Yoshii (2003). Chapter 7 is devoted to conclusion and future prospects.

	Without HD	With HD
Uniform model	Uehara et al. (1996)	Flower (2002)
One-dimensional model	Nakamura & Umemura (1999, 2001)	Uehara & Inutsuka (2001) Nakamura & Umemura (2002)

**Table 1.1:** Papers which investigated fragmentation of filamentary clouds without the external radiation

	Without Pressure	With Pressure
Uniform model	Omukai & Yoshii (2003)	Bessho & Tsuribe (2012a)
One-dimensional model	—	Bessho & Tsuribe (2012b)

**Table 1.2:** Papers which investigated fragmentation of filamentary clouds with the effect of the external dissociating radiation



# Chapter 2

## Model for the filamentary clouds

We introduce a model for a filamentary cloud. In this chapter, we mainly introduce uniform one-zone model. This simple one-zone model gives us clear conclusion. The results of the uniform one-zone model are shown in Chapter 3. In Chapters 4 and 5, we introduce more realistic models. We introduce modification to the uniform model at the beginning of Chapter 4 and 5.

We describe some assumptions which are also assumed in the later chapters. We assume that the filamentary cloud is infinitely long and axisymmetric without rotation. Magnetic field and turbulence are neglected. We do not consider dark matter for simplicity. In the case with high initial density, baryon density is expected to dominate dark matter density and it will give a good approximation. In the case with the low initial density, we will underestimate the effect of dark matter (e.g., large infall velocity owing to dark matter gravity).

### 2.1 Basic equations

We assume that the filamentary clouds are uniform. We solve the virial equation for the dynamical evolution in the cylindrical radial direction (Uehara et al. 1996). The virial equation

for the filamentary cloud of unit length with volume  $V$  is

$$\frac{1}{2} \frac{d^2 I}{dt^2} = 2\Psi + 2\Pi - Gl^2, \quad (2.1)$$

where  $G$  is gravitational constant,  $l$  is the line mass (mass per unit length) of the filamentary cloud,

$$I = \int_V \rho r^2 dV \quad (2.2)$$

is the inertial moment per unit length with density  $\rho$  and radius  $r$ ,

$$\Psi = \int_V \frac{1}{2} \rho v^2 dV \quad (2.3)$$

is the kinetic energy per unit length with the velocity  $v$ , and

$$\Pi = \int_V P dV \quad (2.4)$$

is the integrated pressure per unit length with local pressure  $P$ . By substituting Eqs.(2.2)-(2.4) into Eq.(2.1), we have

$$\frac{d^2 R}{dt^2} = -\frac{2G}{R} \{l - l_c(T)\}, \quad (2.5)$$

where  $R$  is the radius of the filamentary cloud,  $T$  is temperature, and  $l_c(T)$  is the critical line mass for the hydro-static isothermal filamentary cloud defined as

$$l_c(T) \equiv \frac{2k_B T}{\mu m_H G} \quad (2.6)$$

(Ostriker 1964; see Appendix A) with Boltzmann constant  $k_B$ , mean molecular weight  $\mu$ , and mass of a hydrogen atom  $m_H$ .

For the thermal evolution, we solve energy equation

$$\frac{du}{dt} = -P \frac{d}{dt} \frac{1}{\rho} - \frac{\Lambda_{\text{radi}}}{\rho} - \frac{\Lambda_{\text{chem}}}{\rho}, \quad (2.7)$$

where  $u$  is thermal energy per unit mass

$$u = \frac{1}{\gamma_{\text{ad}} - 1} \frac{k_B T}{\mu m_H} \quad (2.8)$$

with adiabatic exponent  $\gamma_{\text{ad}}$ . The first term of the right hand side in Eq.(2.7) denotes adiabatic heating. The radiative cooling rate  $\Lambda_{\text{radi}}$  per unit volume includes lines of H, lines of H<sub>2</sub>, lines of HD, and continuum (see appendix B in detail). For the radiative cooling, the effect of radiative transfer is included according to Susa et al. (1996) (see Appendix C). The symbol  $\Lambda_{\text{chem}}$  represents heating/cooling rate associated with chemical reactions. Equation of state for ideal gas

$$P = \frac{\rho k_B T}{\mu m_H} \quad (2.9)$$

is assumed.

We consider non-equilibrium chemical reactions by solving equations

$$\frac{df_i}{dt} = \sum_{j, k} k_{ijk} f_j f_k n + \sum_j k_{ij} f_j, \quad (2.10)$$

where  $n$  is number density of all nuclei,  $k_{ijk}$  and  $k_{ij}$  are reaction rates for formation and destruction of species  $i$ , and  $f_i$  is the fraction of species  $i$ . We consider the following fourteen species : H, H<sup>+</sup>, H<sup>-</sup>, H<sub>2</sub>, H<sub>2</sub><sup>+</sup>, He, He<sup>+</sup>, He<sup>++</sup>, D, D<sup>+</sup>, D<sup>-</sup>, HD, HD<sup>+</sup>, and e<sup>-</sup>. We consider 35 reactions concerned with H and He taken from Omukai (2001) and 18 reactions concerned with H and D taken from Nakamura & Umemura (2002). We also consider photodestruction of species D, D<sup>-</sup>, and HD<sup>+</sup> (we refer to Galli & Palla 1998 for D and HD<sup>+</sup> and Frolov 2004 for D<sup>-</sup>). Eq.(2.10) is solved numerically with implicit integrator.

## 2.2 External radiation

We assume that the external dissociating radiation to be isotropic. As for the mean intensity of the dissociating radiation, we consider one at  $z \sim 10$ . Estimated from the surrounding star-forming halos, the probability distribution of the mean intensity of the dissociating radiation was investigated by Dijkstra et al. (2008) (see Appendix D). We adopt mean intensities whose probabilities are  $\sim 0.4$ <sup>1</sup> and  $\sim 0.06$  in Dijkstra et al. (2008). Moreover, we assume that the

<sup>1</sup>0.4 is the highest probability.

external radiation is thermal radiation from  $120M_{\odot}$  stars and their surface temperature ( $T_{\text{sur}} = 95719\text{K}$ ) is determined according to Schaerer (2002). We also assume that the ionization photon does not reach the filamentary clouds from light sources and that the external dissociating radiation turns on when the filamentary cloud forms.

The photodissociation reaction of  $\text{H}_2$  is given by,



(Solomon process) where  $\gamma$  is photon with  $12.4\text{eV}$  and  $\text{H}_2^*$  represents  $\text{H}_2$  in excited state. The reaction rate of photodissociation of  $\text{H}_2$  is given by

$$k_{2\text{step}} = 1.4 \times 10^9 J_{\nu} \text{ s}^{-1}, \quad (2.12)$$

where  $J_{\nu}$  is local mean intensity of the dissociating radiation. When we calculate this photodissociation reaction, we consider the extinction of photon by dissociation of  $\text{H}_2$  and absorption by continuum processes. During penetrating the filamentary cloud from the surface to the center, the intensity of the dissociating radiation decreases owing to dissociation of  $\text{H}_2$  and absorption by continuum processes. In this chapter, the effect of radiative transfer of dissociation photon is approximated in term of the product of shield function as  $J_{\nu} = f_{\text{sh}} f_{\text{con}} J_{\nu,0}$ , where  $f_{\text{sh}}$  is self-shielding function due to  $\text{H}_2$ ,  $f_{\text{con}}$  is decreasing rate associated with absorption by continuum processes, and  $J_{\nu,0}$  is the mean intensity of the dissociating radiation at the surface of the filamentary cloud.

First, we consider the photon decreasing rate,  $f_{\text{con}}$ , associated with the absorption of dissociation photon by continuum processes. Radiative transfer equation along the  $s$ -direction is given by

$$\frac{dI_{\nu}}{ds} = -k_{\nu} I_{\nu} + j_{\nu}, \quad (2.13)$$

where  $I_{\nu}$  is the intensity of the radiation of frequency  $\nu$ ,  $k_{\nu}$  is the total opacity associated with continuum processes, and  $j_{\nu}$  is emissivity (see Appendix B). We focus on the dissociation

photons with 12.4eV. For simplicity, we assume that the scattered photons are absorbed immediately. We also assume  $j_\nu = 0$  since  $j_\nu$  mainly consists of lines and continuum with lower energy than 12.4eV. We consider the ray tracing in various directions. Using the length  $R/\sin\theta$  from the surface to the center of the filamentary cloud with angle  $\theta$  from the axis of the filamentary cloud, the intensity of the external radiation at the center ( $r = 0$ ) is given by

$$I_\nu(0) = J_{\nu,0} \exp\left(-\frac{k_\nu R}{\sin\theta}\right). \quad (2.14)$$

Hence,  $f_{\text{con}}J_{\nu,0}$  is given by

$$f_{\text{con}}J_{\nu,0} = \frac{J_{\nu,0}}{4\pi} \int_0^{2\pi} d\phi \int_0^\pi d\theta \sin\theta \exp\left(-\frac{k_\nu R}{\sin\theta}\right). \quad (2.15)$$

The integral of the right hand side in Eq.(2.15) is calculated using the fitting formulae given in Appendix E. In typical results shown in the following chapters, the value of  $f_{\text{con}}$  is found to be larger than 0.97 during the collapse in low density regime ( $n \leq 10^2 \text{cm}^{-3}$ ), where the photodissociation of  $\text{H}_2$  is effective. The absorption in the low density cloud has only a minor effect.

Second, we consider self-shielding function,  $f_{\text{sh}}$ . This function represents degree of photodissociation as function of column density of  $\text{H}_2$ ,  $N_{\text{H}_2}$ , and is given by

$$f_{\text{sh}} = \min\left[1, \left(\frac{N_{\text{H}_2}}{10^{14} \text{cm}^{-2}}\right)^{-3/4}\right] \quad (2.16)$$

(Draine & Bertoldi 1996; see Appendix F). To estimate the effective column density in the filamentary cloud, we estimate average in angle of the length between the surface and the center. Using the length  $R/\sin\theta$  from the surface to the center of the filamentary cloud in the direction with angle  $\theta$  from the axis of the filamentary cloud, effective column density of the filamentary cloud is estimated as

$$N_{\text{H}_2} = \frac{1}{4\pi} \int_0^{2\pi} d\phi \int_0^\pi d\theta \sin\theta \frac{R}{\sin\theta} n_{\text{H}_2} = \frac{\pi}{2} n_{\text{H}_2} R, \quad (2.17)$$

where  $n_{\text{H}_2}$  is number density of  $\text{H}_2$ . Since  $R \propto n^{-1/2}$  in the filamentary cloud, effective column density increases during collapse as  $N_{\text{H}_2} \propto n_{\text{H}_2} R \propto n^{1/2}$ . Finally, the photodissociation reaction

rate of H<sub>2</sub> is given by

$$k_{2\text{step}} = 1.4 \times 10^9 f_{\text{con}} f_{\text{sh}} J_{\nu,0} \text{ s}^{-1}. \quad (2.18)$$

## 2.3 Condition for fragmentation of the filamentary cloud

Nagasawa (1987) derived dispersion relation of dynamically equilibrium isothermal filamentary cloud (see Appendix A). Figure 2.1 shows the dispersion relation for the filamentary cloud. The most unstable wavelength is approximately given by

$$\lambda_{\text{max}} = \frac{2\pi}{k_{\text{max}}} \sim 2\pi R, \quad (2.19)$$

where  $k_{\text{max}}$  is wave number for the most unstable mode. The largest growth rate is given by

$$\omega_{\text{max}} = 0.339\sqrt{4\pi G\rho}. \quad (2.20)$$

Even in the case where a filamentary cloud collapses dynamically, above characteristic scales are not modified largely (Inutsuka & Miyama 1992). Wavelength of the fastest growing mode is same order as the diameter of the filamentary cloud. If the filamentary cloud collapses, its diameter changes and wave length of the fastest growing mode becomes shorter during collapse. If collapse is fast, perturbations have short lives in the most unstable state. On the other hand, if the fastest growing mode has time enough to grow before the filamentary cloud collapses, fragmentation is expected to occur. Thus, in this thesis, the filamentary cloud is assumed to fragment when dynamical time ( $\rho/\dot{\rho}$ ) is longer than time for the fastest growing mode to grow to non-linear,  $1/\omega_{\text{max}}$ . This condition has been also adopted by some papers (Uehara et al. 1996; Nakamura & Umemura 1999, 2001, 2002).

Using the wave length of the fastest growing mode  $\lambda_{\text{max}}$  at the moment of fragmentation, fragment mass is estimated as

$$M_{\text{frag}} \equiv \lambda_{\text{max}} l \sim 2\pi Rl \quad (2.21)$$

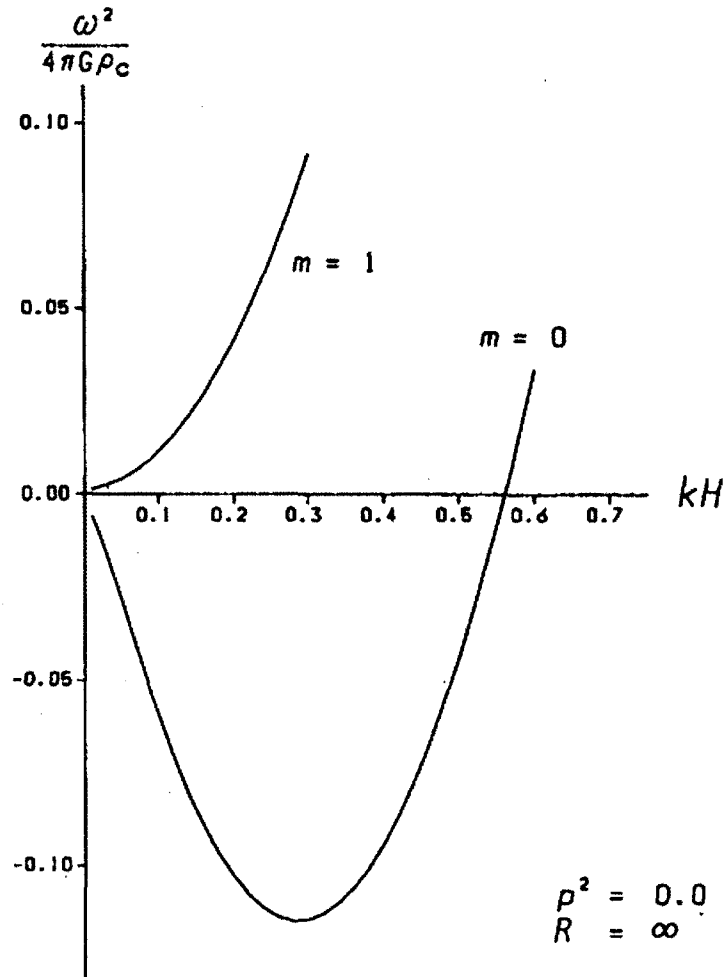


**Figure 2.1:** Dispersion relation of the dynamically equilibrium isothermal filamentary cloud in the case of  $m = 0$  (axisymmetric perturbation), 1 (non-axisymmetric perturbation). The symbol  $H$  is defined as  $H = c_s / \sqrt{4\pi G \rho}$ . This figure is taken from Nagasawa (1987).

(Narita, Miyama, & Hayashi 1987a, b; Larson 1985; Uehara et al. 1996). According to Eq.(2.21), fragment mass is proportional to the radius of the filamentary clouds at the moment of fragmentation. If fragmentation occurs after the filamentary cloud collapses to a small radius with high density, the fragment mass is small.

## 2.4 Parameters and initial conditions

In this thesis, we treat three physical quantities as parameters. The first one is the initial number density  $n_0$ , the second one is the normalized intensity of the external radiation,

$$J_{21} \equiv \frac{J_{h\nu=13.6\text{eV},0}}{10^{-21}\text{erg cm}^{-2}\text{s}^{-1}\text{Hz}^{-1}\text{sr}^{-1}}, \quad (2.22)$$

and the third one is the line mass parameter,

$$f \equiv \frac{\pi G \rho_0 \mu m_{\text{H}}}{2k_{\text{B}}T_0} R_0^2 = \frac{l}{l_c(T_0)} \quad (2.23)$$

with initial density  $\rho_0$ , initial temperature  $T_0$ , and initial radius  $R_0$ . The reason why we choose these three quantities is as follows: for dynamical evolution, the line mass parameter  $f$  is important. In the view point of thermal evolution, initial density  $n_0$  is important. The intensity  $J_{21}$  and  $n_0$  are necessary to study the effect of dissociation photon.

We consider cases with  $\log_{10} n_0 = 1, 1.5, 2, 2.5, 3, 3.5, 4, 4.5, 5, 5.5,$  and  $6$  for  $n_0$  and  $f = 1.25, 1.5, 1.75, 2, 2.25, 2.5, 2.75,$  and  $3$  for  $f$ . The typical value of  $f$  is 2. This value is realized when the sheet-like gas fragments in the fastest growing mode (Miyama et al. 1987a). For  $J_{21}$ , we consider  $J_{21} = 1, 6.5,$  and  $10$ . As the intensity at  $z \sim 10$ , the case with  $J_{21} = 1$  demonstrates the weak external radiation (Dijkstra et al. 2008),  $J_{21} = 6.5$  corresponds to the average intensity, and  $J_{21} = 10$  represents strong radiation case whose probability is 0.06.

We assume that radial infall velocity at the surface of the filamentary cloud equals to the sound speed. If the filamentary clouds form from the sheet-like cloud, gravitational force is comparable to pressure gradient force in the filamentary cloud. Thus, the infall velocity

when the filamentary cloud forms is expected to be in the same order as the sound speed, i.e.,  $v = -\alpha c_s$  with a numerical coefficient  $\alpha \sim O(1)$  which depends on the details of fragmentation. As a typical value, we set  $\alpha = 1$  according to Nakamura & Umemura (2002).

In Chapters 3-5, the filamentary cloud is assumed to form from a cloud which experiences  $H_2$  cooling without UV radiation. We also assume that the external radiation turns on when the filamentary clouds form. For the thermal evolution, the initial values of temperature,  $T_0$ , and fraction of  $H_2$ ,  $f_{H_2}$ , are important. We adopt typical values for them as  $T_0 = 300K$  and  $f_{H_2} = 10^{-4}$ . As the value of  $f_{H_2}$ ,  $f_{H_2} \sim 10^{-4} - 10^{-3}$  is typically seen in cosmological simulations without the external radiation (e.g., Abel et al. 1998). We discuss initial  $H_2$  fraction with the effect of the dissociating radiation in §3.3. Fraction of He,  $f_{He}$ , is set to be 0.0825 which corresponds to the mass fraction  $Y_p = 0.244$  (Izotov & Thuan 1998). Initial fraction of electron,  $f_e$ , is set to be  $10^{-4}$  according to Uehara et al. (1996). We adopt this value of  $f_e$  in order for electron not to change  $f_{H_2}$  artificially in the early stage of collapse<sup>2</sup>. Initial fraction of proton is determined from the charge conservation. We assume that  $D/H = 4 \times 10^{-5}$ , which is consistent with observations of the deuterium Ly $\alpha$  feature in the absorption spectra of high-redshift quasars (e.g., O’Meara et al. 2001). Fraction of other species is set to be zero at the initial state.

---

<sup>2</sup>Electron helps  $H_2$  formation via  $H^-$  channel.



# Chapter 3

## Numerical results I : uniform one-zone model

In this chapter, we show numerical results for the uniform one-zone model of a filamentary cloud which was mentioned in Chapter 2. Comparing results in the cases with and without the external radiation, the effect of the external radiation is clarified. The contents in this chapter are based on Bessho & Tsuribe (2012a).

### 3.1 Numerical results

#### 3.1.1 Cases without the external radiation

In order to clarify the effect of the external radiation, at first, we show the numerical results in the cases without the external radiation.

##### Low initial density and large line mass

First, we show the case with low initial density and large line mass (figure 3.1;  $(f, n_0, J_{21}) = (3, 10\text{cm}^{-3}, 0)$ ). From the early stage of collapse, adiabatic heating rate is a little higher

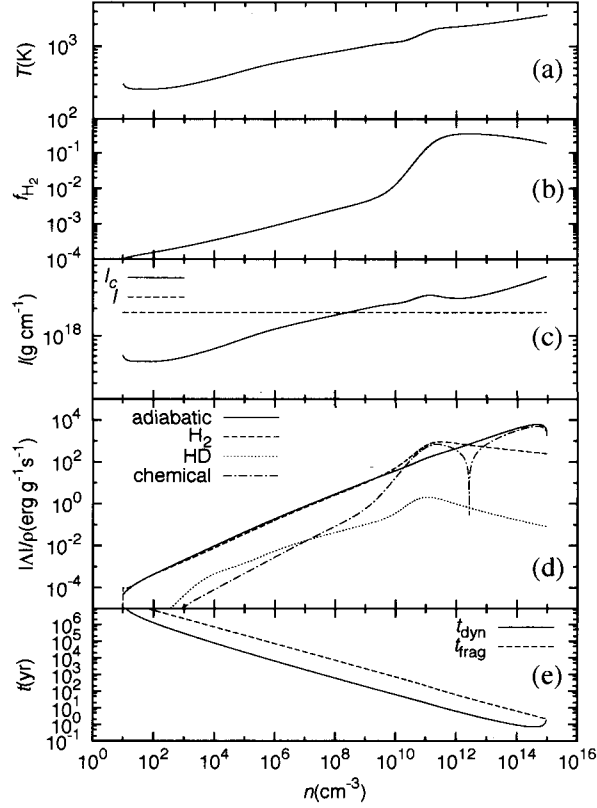


**Figure 3.1:** Evolution of the temperature (a),  $f_{\text{H}_2}$  (b),  $l$  and  $l_c$  (c), the heating and cooling rate (d), and  $t_{\text{dyn}}$  and  $t_{\text{frag}}$  (e), respectively, as a function of the density for the case with  $(f, n_0, J_{21}) = (3, 10\text{cm}^{-3}, 0)$ . Labels "adiabatic" denotes the adiabatic heating, "H<sub>2</sub>" does the H<sub>2</sub> line cooling, "HD" does the HD line cooling, and "chemical" does the chemical heating or cooling. The continuum cooling is not shown because it is not effective. This figure is taken from Bessho & Tsuribe (2012a).

than  $\text{H}_2$  cooling rate and temperature gradually increases. At  $n \sim 10^8 \text{cm}^{-3}$ ,  $l_c$  overcomes  $l$ , and collapse of the filamentary cloud begins to be decelerated. Above  $n \sim 10^8 \text{cm}^{-3}$ , the three-body reaction becomes efficient and  $\text{H}_2$  fraction increases to  $\sim 0.4$ . At  $n \sim 10^{10} \text{cm}^{-3}$ , although  $\text{H}_2$  cooling is still effective, chemical heating associated with the three-body reaction of  $\text{H}_2$  formation also becomes effective. Thus, temperature continues to increase. When the density reaches  $n \sim 10^{11} \text{cm}^{-3}$ , temperature stops increasing owing to sufficient cooling with a large fraction of  $\text{H}_2$ . The filamentary cloud becomes optically thick to  $\text{H}_2$  line emissions at  $n \sim 10^{12} \text{cm}^{-3}$ . Around this density, temperature increases again and it eventually exceeds 2000K. Such a high temperature state causes collisional dissociation of  $\text{H}_2$ . Since chemical cooling associated with this dissociation cannot dominate adiabatic heating, temperature is kept high enough to decelerate collapse. As a result, the filamentary cloud fragments when density reaches  $n \sim 10^{15} \text{cm}^{-3}$ . Several authors pointed out that  $\text{H}_2$  collision-induced emission becomes effective at  $n \sim 10^{15} \text{cm}^{-3}$  (Omukai & Nishi 1998; Ripamonti & Abel 2004; Yoshida et al. 2006). However, in the case in figure 3.1, since temperature is high ( $\sim 3000\text{K}$ ), 80% of  $\text{H}_2$  is dissociated and cooling rate of  $\text{H}_2$  collision-induced emission is smaller than adiabatic heating rate by two orders of magnitude. Since the density of the filamentary cloud at fragmentation is very high ( $n \sim 10^{15} \text{cm}^{-3}$ ), fragment mass is small ( $\sim 0.1M_\odot$ ).

In summary, the evolution of the low density models with large line mass is affected largely by radiative cooling and chemical heating/cooling associated with  $\text{H}_2$ . In this sense, our result is qualitatively the same as the previous results of Uehara et al. (1996) and Nakamura & Umemura (1999, 2001, 2002).

### High initial density and small line mass

Next, we show the case with high initial density and small line mass (figure 3.2;  $(f, n_0, J_{21}) = (1.25, 10^6 \text{cm}^{-3}, 0)$ ). Adiabatic heating dominates cooling a little after the early stage of the collapse,  $n \leq 3 \times 10^6 \text{cm}^{-3}$ . Collapse is accelerated only in the early stage of collapse ( $n \leq 2 \times 10^6 \text{cm}^{-3}$ ) and not after that. Since acceleration is limited in the short density range,

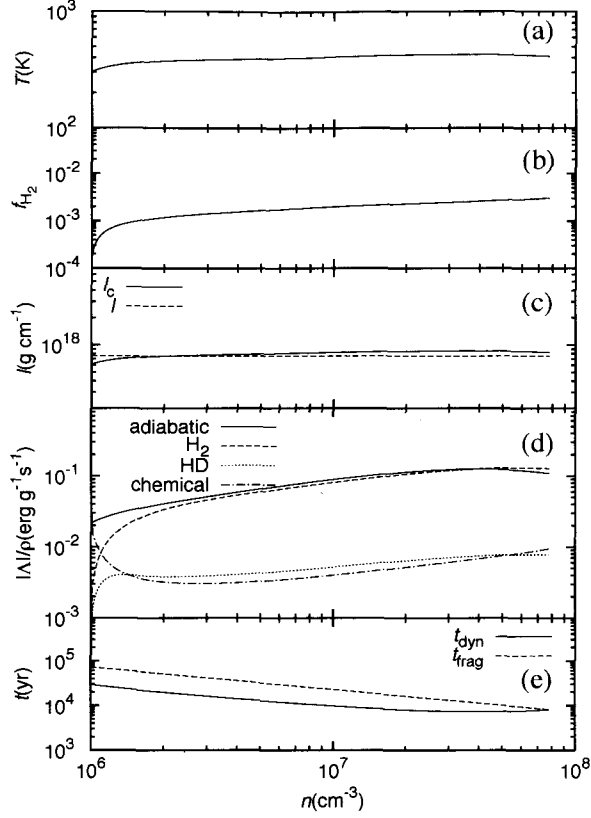


**Figure 3.2:** Same as figure 3.1, but  $(f, n_0, J_{21}) = (1.25, 10^6 \text{cm}^{-3}, 0)$ . This figure is taken from Bessho & Tsuribe (2012a).

collapse of the filamentary cloud is limited at lower density ( $n \sim 10^8 \text{cm}^{-3}$ ) and fragment mass is larger ( $\sim 90 M_\odot$ ) than the case in figure 3.1. Different from the case in figure 3.1,  $\text{H}_2$  cooling never dominates in this case.

We show fragment mass for various  $n_0$  and  $f$  (figure 3.3). All lines are similar to each other and can be approximated as  $M_{\text{frag}} \sim 230 n_0^{-0.03} f^{-5.1}$  with an error at most factor 4 at  $f = 3$ . This approximate function agrees with numerical results at low  $f$  ( $< 2$ ). The fragment mass is determined mainly by  $f$ . This tendency agrees with the result of Uehara et al. (1996). Nakamura & Umemura (2002) suggested that fragment mass depends mainly on

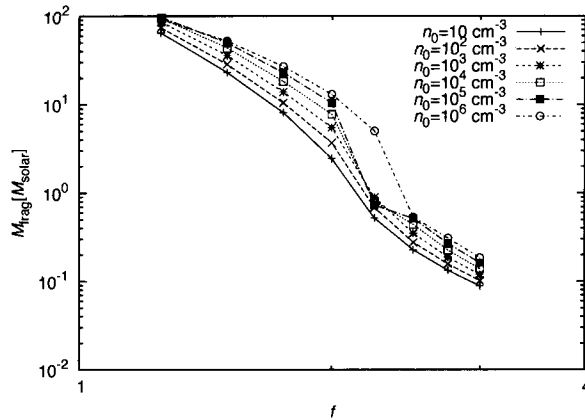


**Figure 3.3:** Fragment mass in the cases without the external radiation with various of  $n_0$  and  $f$ . In the cases with  $f = 2.5$  and  $n_0 \leq 10^5 \text{ cm}^{-3}$ ,  $\text{H}_2$  forms by three body reaction and cools cloud strongly. Since cooling helps collapse, the filamentary clouds collapse up to high density ( $\sim 10^{13} \text{ cm}^{-3}$ ) and the fragment mass becomes small ( $< 1M_\odot$ ). This figure is taken from Bessho & Tsuribe (2012a).

$n_0$ . Our results disagree with that of Nakamura & Umemura (2002). This difference comes from simplicity that the filamentary cloud is assumed to be uniform in the present model. In the uniform model, virial temperature is determined by the line mass of the whole cloud ( $fl_c$ )<sup>1</sup>. On the other hand, the evolution of the more realistic non-uniform filamentary cloud includes run-away characteristics of the flow. The improved model with the effect of run-away collapse is introduced in Chapter 4 (the one-dimensional model is considered in Chapter 5).

### 3.1.2 Cases with the external radiation

We showed the results in the case without the external dissociating radiation in previous subsection. Next, we show the results with the external radiation. Comparing with previous

<sup>1</sup>Since collapse of the uniform filamentary cloud is homologous, virial temperature is determined by whole line mass, that is  $fl_c$ . On the other hand, in the more realistic case, since collapse of the filamentary cloud is in run-away fashion, virial temperature is determined by mass of the central region. The mass of the central region mainly depends on  $n_0$ .

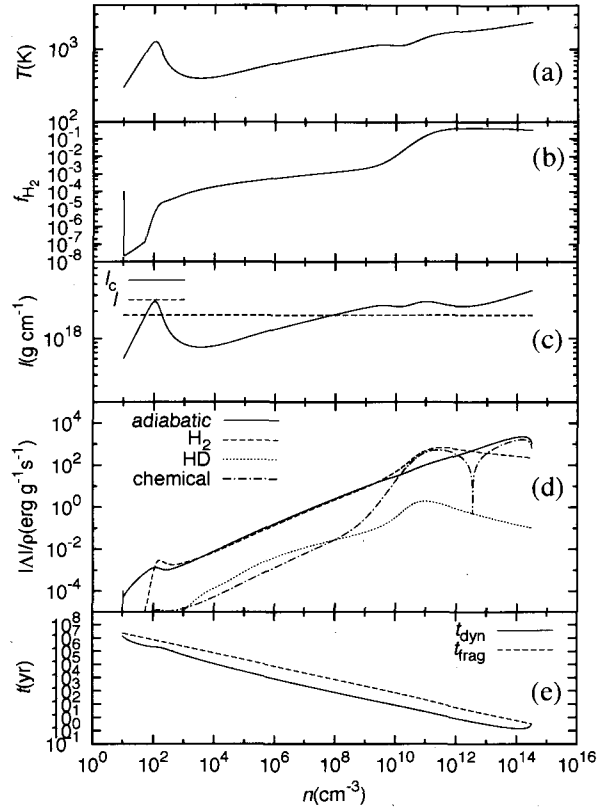


**Figure 3.4:** Same as figure 3.1, but  $(f, n_0, J_{21}) = (3, 10\text{cm}^{-3}, 10)$ . This figure is taken from Bessho & Tsuribe (2012a).

subsection, we clarify the effect of the external radiation.

### Low initial density and large line mass with strong radiation

First, we show the case with low initial density, large line mass, and strong external radiation (figure 3.4;  $(f, n_0, J_{21}) = (3, 10\text{cm}^{-3}, 10)$ ). This case in figure 3.4 corresponds to the case in figure 3.1 with the external radiation. Because of low initial density, the filamentary cloud may suffer photodissociation in the early stage of collapse. In figure 3.4, it is seen that  $f_{\text{H}_2}$  decreases at the start of collapse ( $n \sim 10\text{cm}^{-3}$ ) owing to photodissociation and adiabatic

heating dominates from the early stage of collapse. Cylindrical collapse is decelerated at  $n \sim 10^2 \text{cm}^{-3}$  since temperature increases. However, this deceleration is temporary and the filamentary cloud does not fragment at this point. Instead, it continues to collapse and shields itself from the dissociation photon. Then,  $f_{\text{H}_2}$  begins to increase at  $n \sim 10^2 \text{cm}^{-3}$ . After that,  $\text{H}_2$  cooling becomes efficient and the evolution becomes similar to that in figure 3.1. As a result, the filamentary cloud collapses until it becomes optically thick to  $\text{H}_2$  lines, and it fragments into the low mass clumps with  $0.14M_{\odot}$ . In this case, the external radiation affects thermal evolution in the early stage and does not change fragment mass because of large line mass.

### Low initial density and small line mass with strong radiation

Next, we show the case with low initial density, small line mass, and strong external radiation (figure 3.5;  $(f, n_0, J_{21}) = (1.25, 10 \text{cm}^{-3}, 10)$ ). In this case, the filamentary cloud fragments at lower density than in figure 3.4 because of small line mass. In the early phase, the external radiation photodissociates  $\text{H}_2$  since dissociation photon penetrates the filamentary cloud with low column density. The early photodissociation suppresses  $\text{H}_2$  cooling. As a result, temperature increases adiabatically until fragmentation. Since collapse is terminated and fragmentation occurs at low density ( $\sim 34 \text{cm}^{-3}$ ), fragment mass is very large ( $\sim 10^5 M_{\odot}$ ).

The different results between the cases with (figure 3.4) and without the external radiation (figure 3.1) originates from whether or not  $\text{H}_2$  is dissociated by the external radiation in the early stage. It is found that the filamentary clouds with low  $f$  ( $< 2.5$ ) evolve adiabatically and fragment into very massive clumps if  $\text{H}_2$  is photodissociated sufficiently enough to suppress  $\text{H}_2$  cooling.

The difference between results of figure 3.4 and figure 3.5 is originated from the different value of line mass. In both case, since the initial density is low,  $\text{H}_2$  is dissociated and the filamentary clouds evolve adiabatically in the early stage. Since line mass for the case in figure 3.5 is smaller, a slight increase of temperature is sufficient to suppress collapse. On the other hand, since the line mass for the case in figure 3.4 is larger, a slight increase of temperature

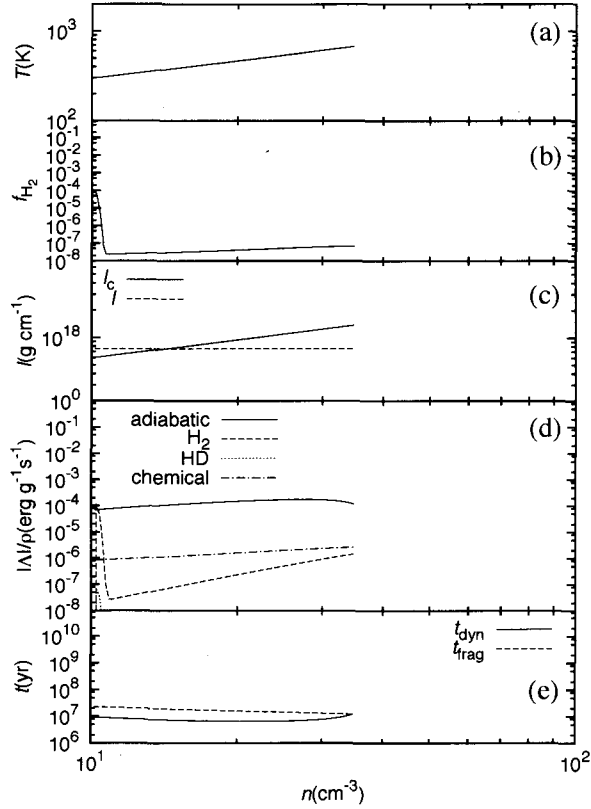


**Figure 3.5:** Same as figure 3.1, but  $(f, n_0, J_{21}) = (1.25, 10\text{cm}^{-3}, 10)$ . This figure is taken from Bessho & Tsuribe (2012a).

is not sufficient to suppress collapse. Hence, in the case in figure 3.4, the filamentary cloud does not fragment in the early stage of collapse and sufficient amount of  $\text{H}_2$  forms eventually to cool the filamentary cloud. A critical line mass to shield themselves from the dissociation photon is discussed analytically in §3.2.4.

### High initial density and small line mass with strong radiation

Finally, we show the case with high initial density, small line mass, and strong external radiation (figure 3.6;  $(f, n_0, J_{21}) = (1.25, 10^6\text{cm}^{-3}, 10)$ ). This case in figure 3.6 corresponds to the

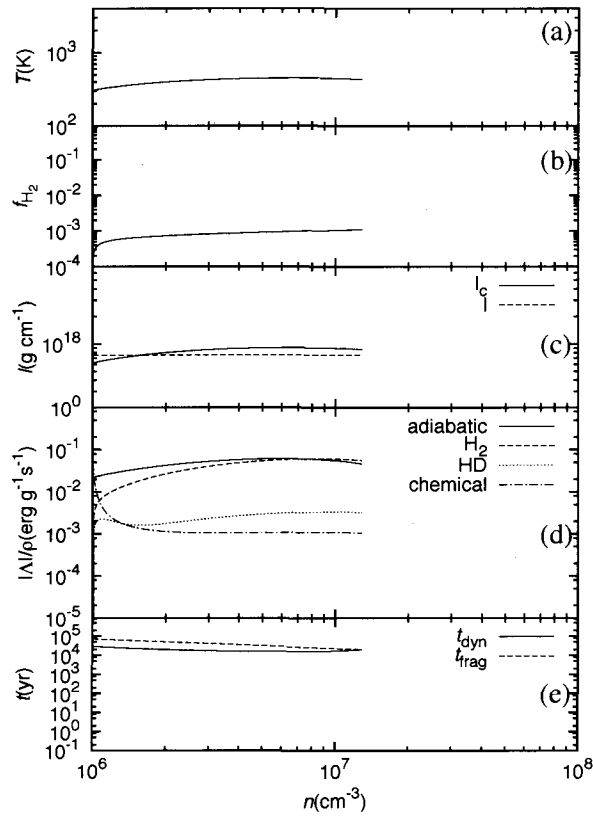


**Figure 3.6:** Same as figure 3.1, but  $(f, n_0, J_{21}) = (1.25, 10^6 \text{cm}^{-3}, 10)$ . This figure is taken from Bessho & Tsuribe (2012a).

case in figure 3.2 with the external radiation. Because of high initial density, the filamentary cloud may not suffer photodissociation. This is because the initial density is high enough to shield the filamentary cloud from dissociation photon. The filamentary cloud fragments into the slightly more massive fragments ( $230M_{\odot}$ ) than in the case without the external radiation (figure 3.2). This is because  $\text{H}_2$  is photodissociated a little and higher temperature suppresses collapse at smaller density than in figure 3.2.

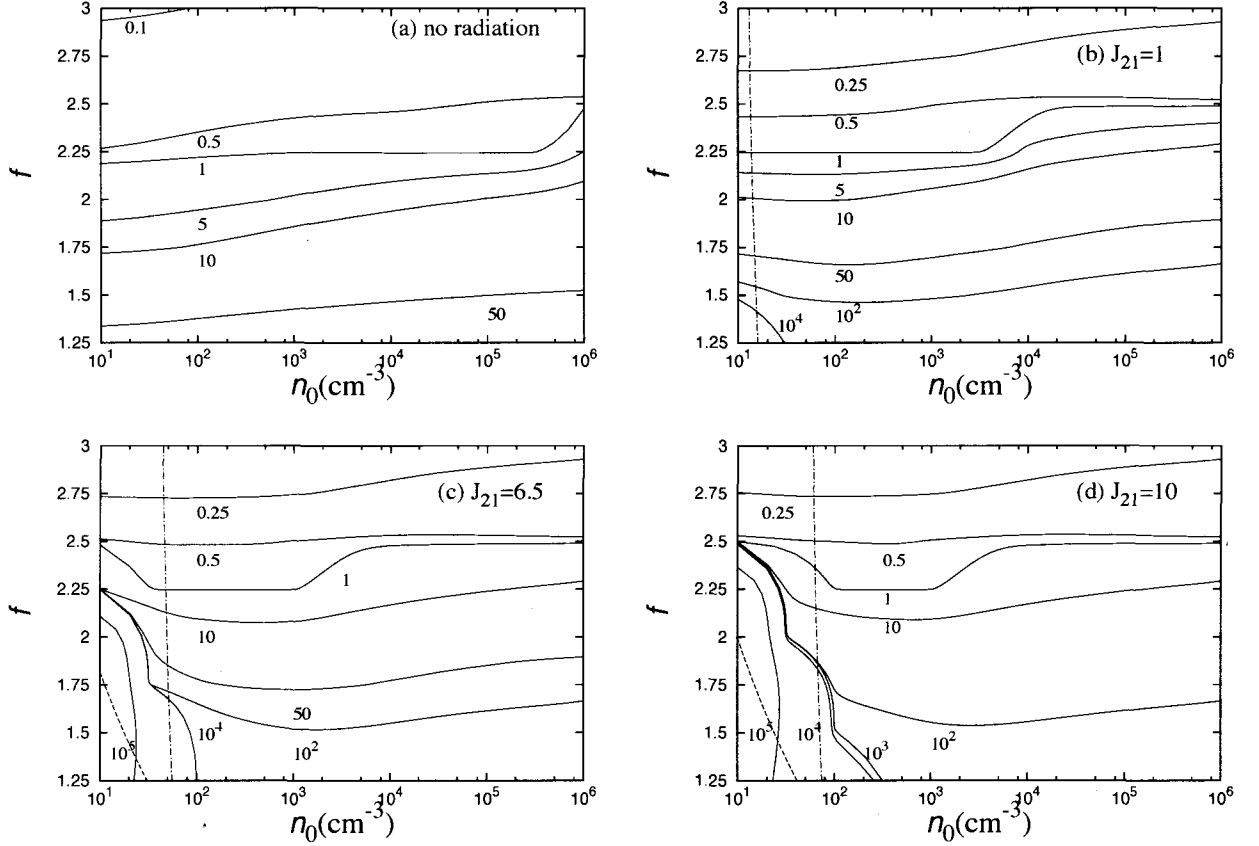


**Figure 3.7:** The contours maps for the fragment mass in  $n_0 - f$  plane for the case with (a)  $J_{21} = 0$ , (b)  $J_{21} = 1$ , (c)  $J_{21} = 6.5$ , and (d)  $J_{21} = 10$ . The number attached to each solid line is mass of fragment in units of  $M_{\odot}$ . The dashed line and the dot-dashed line denote Eq.(3.17) and Eq.(3.13), respectively. The region on right of the dash-dotted line satisfies  $t_{\text{cool}} > t_{\text{ff}}$ . This figure is taken from Bessho & Tsuribe (2012a).

### 3.1.3 Fragment mass

We show the effect of the external dissociating radiation on fragment mass in figure 3.7 which shows the fragment mass for all the parameters by using contours maps in  $n_0 - f$  plane. Results for different values of  $J_{21} = 0, 1, 6.5,$  and  $10$  are presented in different diagrams. Solid lines in each diagram of figure 3.7 represent constant fragment mass. The dotted line and the dash-dotted line will be introduced in §3.2. In diagram (b) with  $J_{21} = 1$ , the region with large fragment mass ( $> 10^4 M_\odot$ ) is found in the range  $n_0 \leq 10^{1.5} \text{cm}^{-3}$  and  $f < 1.5$ . This region is clearly as the result of the external radiation since such a region does not exist in diagram (a) with  $J_{21} = 0$ . With larger  $J_{21}$  in diagrams (c) and (d), it is seen that the region with massive fragment ( $> 10^4 M_\odot$ ) becomes larger in  $n_0 - f$  plane. In diagram (c), this region spreads up to  $n_0 \leq 10^2 \text{cm}^{-3}$  and  $f \leq 2.25$ . In diagram (d), this region spreads up to  $f \leq 2.5$ .

However, in the case with  $n_0 > 10^2 \text{cm}^{-3}$  or  $f \geq 2.5$ , it is seen that the fragment mass is hardly changed by the external radiation. This is explained as follows : as for the cases with large  $n_0$ , the filamentary clouds shield themselves from the dissociating radiation from the early stage of evolution. As for the cases with large  $f$ , as shown in figure 3.4, the filamentary clouds continue to collapse up to density high enough to shield themselves from the external radiation and to form  $\text{H}_2$  even if  $\text{H}_2$  is photodissociated in the early stage of collapse.

## 3.2 Analytic investigation

In this section, we analytically investigate the property shown in the numerical results in §3.1. To explain the property of the collapsing filamentary cloud, three criteria are considered in the view point whether or not the filamentary cloud can cool during collapse.

### 3.2.1 Cooling criterion 1 : whether cooling is effective or not

There is a critical value  $n_a$  of initial density that determines whether or not  $H_2$  cooling dominates adiabatic heating at the start of collapse. Before we consider the effect of the external radiation, we first derive  $n_a$  without the effect of the external radiation. If initial density is less than  $n_a$ . If  $H_2$  cooling dominates adiabatic heating at the start of collapse, the following inequality is satisfied :

$$-P \frac{d}{dt} \frac{1}{\rho} < \frac{\Lambda_{H_2}}{\rho}. \quad (3.1)$$

The rate of  $H_2$  cooling is approximated as

$$\Lambda_{H_2} \simeq \begin{cases} 2.5 \times 10^{-26} n^2 f_{H_2} \left( \frac{T}{300K} \right)^3 & n \ll 10^4 \text{cm}^{-3} \\ 8.0 \times 10^{-24} n f_{H_2} \left( \frac{T}{300K} \right)^{3.8} & n \gg 10^4 \text{cm}^{-3} \end{cases} \quad (3.2)$$

(Galli & Palla 1998), where  $\Lambda_{H_2}$  is in units of  $\text{erg cm}^{-3}\text{s}^{-1}$ . Assuming that the timescale of collapse is the free-fall time ( $1/\rho \cdot d\rho/dt = -t_{\text{ff}}^{-1}$ ), Eq.(3.1) gives

$$\frac{k_B T_0}{\mu m_H} \cdot \sqrt{2\pi G \rho} < \frac{\Lambda_{H_2}}{\rho}. \quad (3.3)$$

In the case for  $n \ll 10^4 \text{cm}^{-3}$  in Eq.(3.2) with  $f_{H_2} = 10^{-4}$  for the initial state, the cooling condition is found to be

$$n > n_a \equiv 1.9 \times 10^2 \left( \frac{T_0}{300K} \right)^{-6} \left( \frac{f_{H_2}}{10^{-4}} \right)^{-2} \text{cm}^{-3}. \quad (3.4)$$

In the case with  $n \gg 10^4 \text{cm}^{-3}$ , adiabatic heating always dominates  $H_2$  cooling. Thus,  $H_2$  cooling dominates adiabatic heating at the start of collapse for  $n_a < n_0 < 10^4 \text{cm}^{-3}$  if  $f_{H_2} = 10^{-4}$  and  $T_0 = 300K$  is assumed. In the case in figure 3.2, since the filamentary cloud has higher initial density than  $10^4 \text{cm}^{-3}$ , temperature increases at the early stage of collapse. Since this condition (Eq.3.4) does not include the effect of the external radiation, Eq.(3.4) should be accepted as a necessary condition for cooling.

### 3.2.2 Equilibrium fraction of H<sub>2</sub>

Let us investigate the condition whether or not H<sub>2</sub> cooling dominates adiabatic heating in the early stage with the effect of the external radiation. Since cooling rate depends on H<sub>2</sub> fraction, we first estimate the equilibrium fraction of H<sub>2</sub> which is attained when formation and photodissociation of H<sub>2</sub> balance under the external radiation. Assuming the chemical equilibrium between formation and photodissociation of H<sub>2</sub>, fraction of H<sub>2</sub> is found to be

$$f_{\text{H}_2} = \frac{n f_e k_{\text{H}^-}}{k_{2\text{step}}}, \quad (3.5)$$

where  $k_{\text{H}^-} = 1.0 \times 10^{-18} T \text{ cm}^3 \text{ s}^{-1}$  is the reaction rate for H<sup>-</sup> channel,



At the initial state in our model, timescale of formation of H<sub>2</sub>,  $t_{\text{form}}$ , is given by

$$t_{\text{form}} = \frac{1}{k_{\text{H}^-} n_0 f_e} = 3.33 \times 10^{18} \left( \frac{T}{300\text{K}} \right)^{-1} \left( \frac{n_0}{10\text{cm}^{-3}} \right)^{-1} \left( \frac{f_e}{10^{-4}} \right)^{-1} \text{ s}. \quad (3.7)$$

On the other hand, assuming that  $N_{\text{H}_2}$  is larger than  $10^{14} \text{ cm}^{-2}$ , timescale of photodissociation is given by

$$t_{\text{diss}} = \frac{1}{k_{2\text{step}} f_{\text{H}_2}} = 2.26 \times 10^{17} \left( \frac{J_{21}}{1} \right)^{-1} \left( \frac{N_{\text{H}_2}}{10^{14} \text{ cm}^{-2}} \right)^{3/4} \left( \frac{f_{\text{H}_2}}{10^{-4}} \right)^{-1} \text{ s}. \quad (3.8)$$

Equilibrium H<sub>2</sub> fraction,  $f_{\text{H}_2, \text{eq}}$ , can be estimated by the condition  $t_{\text{form}} = t_{\text{diss}}$ . Substituting the column density

$$\begin{aligned} N_{\text{H}_2} &= \frac{\pi}{2} n f_{\text{H}_2} R = \frac{\pi n^{1/2} f^{1/2} f_{\text{H}_2}}{2m_{\text{H}}} \sqrt{\frac{2k_{\text{B}}T}{\pi \mu G}} \\ &\sim 2.40 \times 10^{21} \left( \frac{n}{10\text{cm}^{-3}} \right)^{1/2} \left( \frac{T}{300\text{K}} \right)^{1/2} f^{1/2} f_{\text{H}_2} \text{ cm}^{-2} \end{aligned} \quad (3.9)$$

into Eq.(3.8), we have

$$f_{\text{H}_2, \text{eq}} = \min \left[ 2.88 \times 10^{-5} \left( \frac{n}{10\text{cm}^{-3}} \right)^{11/2} \left( \frac{T}{300\text{K}} \right)^{11/2} J_{21}^{-4} f^{3/2}, 1 \right]. \quad (3.10)$$

According to Eq.(3.10),  $f_{\text{H}_2,\text{eq}}$  is expected to be large for high density. In the cases with  $J_{21} = 1, 6.5,$  and  $10,$  Eq.(3.10) predicts  $f_{\text{H}_2,\text{eq}} \sim 1$  for  $n > 76.6\text{cm}^{-3}, 299\text{cm}^{-3},$  and  $409\text{cm}^{-3},$  respectively. In order to check the accuracy of Eq.(3.10), we compared  $f_{\text{H}_2,\text{eq}}$  with minimum of fraction of  $\text{H}_2$  of the numerical results. As a result, in the cases with  $J_{21} = 6.5$  and  $10,$  it is found that  $f_{\text{H}_2,\text{eq}}$  agrees with numerical results within error of 40 %. On the other hand, in the case with  $J_{21} = 1,$  it is found that  $f_{\text{H}_2}$  given by Eq.(3.10) is about 2.5 orders of magnitude smaller than the numerical result. This is because  $\text{H}_2$  formation dominates photodissociation.

### 3.2.3 Cooling criterion 2 : whether cooling becomes effective when formation and photodissociation of $\text{H}_2$ balance

In this subsection, we derive the condition whether  $\text{H}_2$  cooling dominates adiabatic heating in the early stage under the external radiation by assuming that the formation of  $\text{H}_2$  balances with photodissociation. Cooling time is estimated as

$$t_{\text{cool}} = \frac{3nk_B T}{2\Lambda_{\text{H}_2}}, \quad (3.11)$$

where Eq.(3.2) is used in  $\Lambda_{\text{H}_2}$ . On the other hand, free-fall time of the uniform filamentary cloud is given by

$$t_{\text{ff}} = \frac{1}{\sqrt{2\pi G\rho}}. \quad (3.12)$$

By equating  $t_{\text{cool}}$  and  $t_{\text{ff}}$  for  $n \ll 10^4\text{cm}^{-3}$  with assuming  $f_{\text{H}_2} < 1,$  we have the critical initial density  $n_b$  as

$$n_b = 78\text{cm}^{-3} \left( \frac{T}{300\text{K}} \right)^{-5/4} \left( \frac{J_{21}}{10} \right)^{2/3} f^{-1/4}. \quad (3.13)$$

In the case with  $n_0 > n_b,$   $\text{H}_2$  photodissociation is too weak to halt  $\text{H}_2$  cooling. On the other hand, the case with  $n_0 < n_b$  has a possibility to halt  $\text{H}_2$  cooling. In diagrams (b), (c), and (d) of figure 3.7, prediction by Eq.(3.13) is plotted by the dash-dotted lines<sup>2</sup>. Comparing

<sup>2</sup>The dash-dotted line is not drawn in diagram (a) of figure 3.7 since we are interested only in the case with the external radiation.

with numerical results, it is found that the dash-dotted line in figure 3.7 gives us a reasonable criterion for the formation of very massive fragments ( $M \geq 10^4 M_\odot$ ).

### 3.2.4 Cooling criterion 3 : whether cooling is effective with adiabatically increasing temperature

We investigate another criterion by which  $H_2$  cooling becomes effective during the hypothetical collapse with increasing temperature as a result of strong photodissociation of  $H_2$  in the early stage. There are numerical examples presented in figure 3.4/figure 3.5 where  $H_2$  cooling is effective/ineffective. Since most of  $H_2$  is once photodissociated in both examples, the difference between these two examples originates from the difference in line mass. Here, we derive the critical line mass  $f_c$  to enable effective  $H_2$  cooling after strong photodissociation from the condition that the filamentary cloud continues to collapse up to the density high enough to shield themselves from the dissociation photon. In the cases with  $f < f_c$ ,  $H_2$  cooling never dominates adiabatic heating and the filamentary clouds fragment into very massive fragments ( $\sim 10^{4-5} M_\odot$ ; c.f., figure 3.5).

We assume  $n = n_b \ll 10^4 \text{cm}^{-3}$  (see Eq.(3.13)). We define that  $H_2$  cooling is "effective" if  $H_2$  cooling dominates adiabatic heating when the condition  $l = l_c(T)$  is achieved (i.e., gravitational force balances with pressure gradient force). We assume that thermal evolution is adiabatic since initial density is low enough not to shield the filamentary cloud from the dissociation photon. In the adiabatic evolution, temperature  $T$  at the density  $n$  is given by

$$T = T_0 \left( \frac{n}{n_0} \right)^{2/3}. \quad (3.14)$$

In the initial state, we assume  $l > l_c(T)$ . As the filamentary cloud collapses  $l_c(T)$  increases, and  $l_c(T)$  becomes as large as  $l$ . Then, we have

$$\frac{2k_B T}{\mu m_H G} = l (= f l_c(T_0)). \quad (3.15)$$

Since the filamentary clouds mainly consist of hydrogen atom, we assume  $\mu \sim 1$ . Using Eqs.(3.14) and (3.15), we have

$$T = fT_0. \quad (3.16)$$

Using Eqs (3.13), (3.14), and (3.16), we have

$$f_c = 2.0 \left( \frac{n_0}{10\text{cm}^{-3}} \right)^{-1/3} \left( \frac{T_0}{300\text{K}} \right)^{-5/12} \left( \frac{J_{21}}{10} \right)^{2/9}. \quad (3.17)$$

In figure 3.7, the condition  $f = f_c$  is shown by dashed lines. It is seen that the dashed line in diagrams (c) and (d) approximately coincides with the solid line for fragment mass  $\sim 10^5 M_\odot$  given by numerical results of the collapsing filamentary cloud. Thus, we conclude that the condition  $f < f_c$  with Eq.(3.17) provides a useful criterion for the formation of very massive fragments. Assuming Eq.(3.10) in the case with  $J_{21} = 1$ , the criterion  $f_c$  has about factor 3 of error.

### 3.3 Discussion

Although initial  $\text{H}_2$  fraction is assumed to be  $10^{-4}$  at  $n = n_0 \geq 10\text{cm}^{-3}$ , this value of  $\text{H}_2$  fraction is expected to be affected by the external radiation before the density of the cloud reaches  $n_0$ . In previous papers without the external radiation,  $f_{\text{H}_2} = 10^{-4} - 10^{-3}$  is adopted as states for the filamentary cloud after virialization (e.g., Uehara et al. 1996; Nakamura & Umemura 1999, 2001, 2002). In this sense, our choice of initial value,  $f_{\text{H}_2} = 10^{-4}$ , should be regarded as the case where the external radiation turns on at the moment when the filamentary cloud forms.

Here we discuss the validity of our assumption that initial  $f_{\text{H}_2}$  is set to be  $10^{-4}$  when the external radiation turns on before the filamentary cloud forms. We investigate how much  $f_{\text{H}_2}$  is expected at  $n = 10\text{cm}^{-3}$  in the case where the external radiation turns on when  $n = n_{\text{UV}} < 10\text{cm}^{-3}$ . As a result of the evolution of  $\text{H}_2$  fraction started from sufficiently low initial density

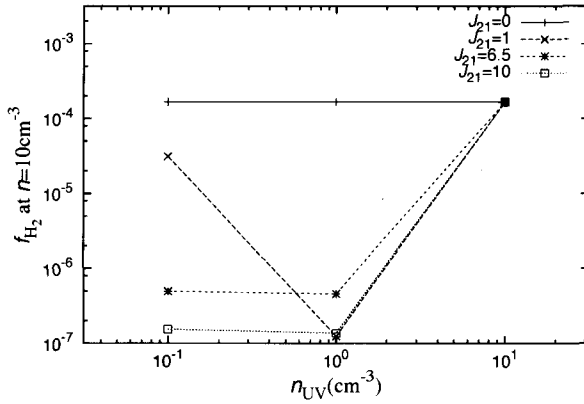


**Figure 3.8:** The fraction of  $\text{H}_2$  at  $n = 10\text{cm}^{-3}$ , as function of  $n_{\text{UV}}$  which is the density at which light sources turn on. Each line corresponds to various  $J_{21}$ . This figure is taken from Bessho & Tsuribe (2012a).

$n_0 = 0.1\text{cm}^{-3}$  with zero initial fraction of  $\text{H}_2$ , we show  $\text{H}_2$  fraction at  $n = 10\text{cm}^{-3}$  as a function of  $n_{\text{UV}}$  for the cases with different  $J_{21}$  in figure 3.8. It is seen that  $\text{H}_2$  fraction expected at  $n = 10\text{cm}^{-3}$  is much different in the cases with different  $J_{21}$  and  $n_{\text{UV}}$ . From figure 3.8, we concluded that initial fraction  $f_{\text{H}_2} = 10^{-4}$  at  $n = n_0$  is valid only when the external radiation turns on at the moment when the filamentary cloud forms.

### 3.4 Summary of uniform one-zone model

It is found that with initial  $\text{H}_2$  fraction  $f_{\text{H}_2} = 10^{-4}$ , the filamentary cloud with low initial density ( $n_0 \leq 10^2\text{cm}^{-3}$ ), and moderate line mass ( $f \leq 2$ ) loses its cooling ability as a result of photodissociation of  $\text{H}_2$  by the external radiation whose mean intensity is  $J_{21} \geq 6.5$ . In such a case, gravitational collapse proceeds adiabatically, and the filamentary clouds fragment into more massive fragments ( $\sim 10^{4-5}M_{\odot}$ ) than the case without the external radiation ( $\sim 0.1 - 50M_{\odot}$ ). In the cases with lower intensity of the external radiation, the filamentary cloud collapses without fragmentation to density which is high enough for  $\text{H}_2$  to form as a

result of self-shielding. In these cases, fragment mass is expected to be similar to the case without the external radiation. If the initial density is high ( $n_0 > 10^2 \text{cm}^{-3}$ ), the filamentary cloud shields itself from the dissociation photons. However, in such a high initial density case, adiabatic heating dominates cooling. As a result, they fragment into more massive fragments ( $\sim 100M_\odot$ ) than in the low initial density cases with effective  $\text{H}_2$  cooling. Summarizing the results of numerical calculations, figure 3.7 clearly shows that the effect of the external dissociating radiation increases fragment mass in low initial density cases. In §3.2, we derived an analytic criterion for the formation of very massive fragments via photodissociation. It is found that massive fragment is expected if the cooling time with equilibrium  $\text{H}_2$  fraction is longer than the free-fall time at the end of hypothetical adiabatic collapse (Eq.3.17).

### 3.5 Problem of uniform one-zone model

So far, we have assumed a uniform filamentary cloud where density of cloud is constant. However, fragment mass predicted by the uniform model of the filamentary cloud tends to be lower than the result with more realistic treatment such as one-dimensional calculation (Uehara & Inutsuka 2000). Although sub-solar fragments are found in figure 3.7, they are not found in the results of one-dimensional hydrodynamical calculations (see figure 3.9; Nakamura & Umemura 2002). Furthermore, fragment mass is determined by  $f$  in the present result (figure 3.7), although it also depends on  $n_0$  in one-dimensional calculations (figure 3.9). In the uniform one-zone model, collapse of the filamentary cloud is homologous, and line mass is constant. However, collapse of the filamentary cloud is actually a run-away collapse (Inutsuka & Miyama 1992), and line mass of the dense central region decreases as collapse proceeds. In order to take into account these effect, in Chapter 4, we develop the improved one-zone model which partly captures the effect of run-away collapse.

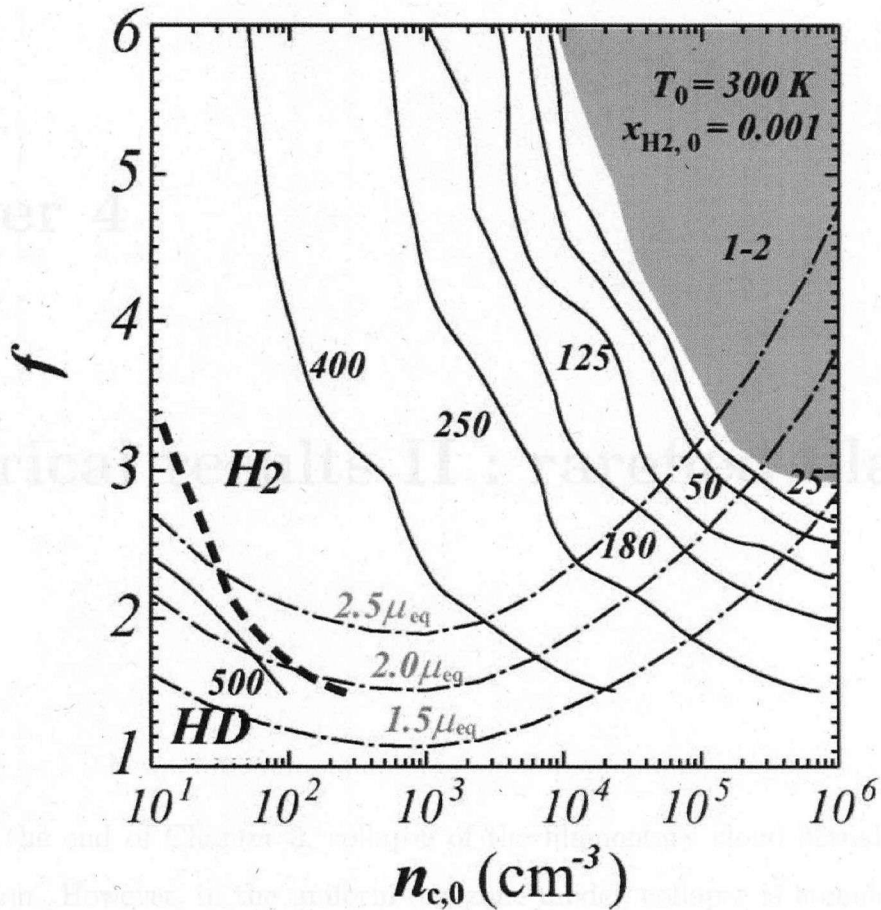


**Figure 3.9:** The contours maps for the fragment mass in  $n_0 - f$  plane for the case with  $(T_0, f_{H_2}) = (300\text{K}, 10^{-3})$ . The ordinate denotes the initial central density and the parameter  $f$ , respectively. The solid lines denote the contours of the fragment mass. The number attached to solid line is fragment mass in unit of  $M_{\odot}$ . Thick dashed-line is the line at which  $\Lambda_{H_2} = \Lambda_{HD}$  at the fragmentation. In the left region of the dashed-line, HD cooling is more efficient than  $H_2$  cooling. The symbol  $\mu_{eq}$  is line mass of equilibrium filamentary cloud. This figure is taken from Nakamura & Umemura (2002).



## Chapter 4

# Numerical results II : rarefied filament model

As pointed at the end of Chapter 3, collapse of the filamentary cloud actually collapses in run-away fashion. However, in the uniform one-zone model, collapse is homologous, and the filamentary cloud collapses up to higher density than in more realistic situation (e.g., one-dimensional calculations). We need to take into account the effect of run-away collapse and in this chapter we develop improved one-zone model. In order to include the effect of run-away collapse, we model decreasing of line mass as collapse proceeds. Hence, the filamentary cloud fragments at lower density than the uniform one-zone model. Smaller line mass at the moment of fragmentation predicts smaller fragment mass than in uniform one-zone model. However, lower density at the moment of fragmentation predicts larger fragment mass. As a result, whether fragment mass is smaller or larger than in uniform one-zone model is not obvious. The contents in this chapter are based on Bessho & Tsuribe (2012a).

## 4.1 Modification to the model

Consider a collapsing filamentary cloud with uniform initial density and pressure. As the cloud collapses, radius of the cloud decreases. In addition to this, the rarefaction wave propagates inward from the outer boundary according to

$$\frac{d\tilde{l}}{dt} = -2\pi\tilde{r}\rho c_s, \quad (4.1)$$

where  $\tilde{r}$  is the position of the rarefaction front,  $\tilde{l}$  is the line mass, and  $\rho$  is density inside  $\tilde{r}$ . Combining with the solution of density, velocity for homologous collapse, and  $\tilde{l} = \pi\tilde{r}^2\rho$ , we can calculate the evolution of  $\tilde{r}$  and  $\tilde{l}$ . Using  $\tilde{r}$  and  $\tilde{l}$ , we define and solve the modified virial equation instead of Eq.(2.5) as

$$\frac{d\tilde{v}}{dt} = -\frac{2G}{\tilde{r}}\{\tilde{l} - l_c(T)\}, \quad (4.2)$$

where  $\tilde{v}$  is the infall velocity at the rarefaction wave front. Hereafter we denote this model as the "rarefied filament model". Different from the uniform one-zone model in previous sections, in the rarefied filament model  $\tilde{l}$  decreases as the cloud collapses. Thus, in this model the right hand side of Eq.(4.2) becomes positive at lower density than the uniform one-zone model (Eq.(2.5)). Similarly, fragmentation is expected to occur at lower density in the rarefied filament model. These differences are originated from the property of run-away collapse. For fragmentation, the condition introduced in §2.3 is assumed. Mass of the fragment is calculated using  $M_{\text{frag}} = 2\pi\tilde{r}\tilde{l}$  instead of Eq.(2.21).

## 4.2 Numerical results

### 4.2.1 Cases without the external radiation

In order to clarify the effect of the external dissociating radiation, we first show the result in the case without the external radiation. Furthermore, we show the difference between the uniform filament model (Chapter 3) and rarefied filament model.

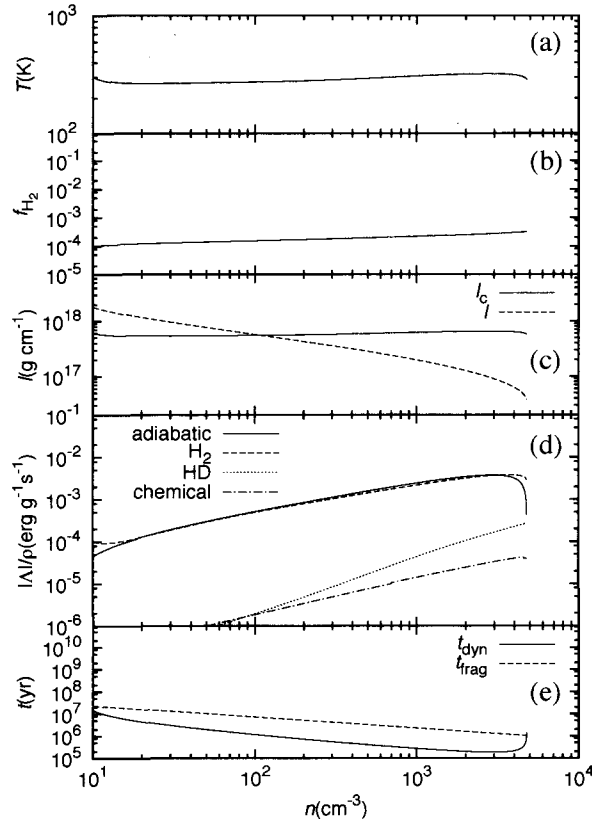


**Figure 4.1:** Evolution of the temperature (a),  $f_{\text{H}_2}$  (b),  $\tilde{l}$  and  $l_c$  (c), the heating and cooling rate (d), and  $t_{\text{dyn}}$  and  $t_{\text{frag}}$  (e), respectively, as a function of the density for model with  $(f, n_0, J_{21}) = (3, 10\text{cm}^{-3}, 0)$ , in which "adiabatic" denotes the adiabatic heating, "H<sub>2</sub>" does the H<sub>2</sub> line cooling, "HD" does the HD line cooling, and "chemical" does the chemical heating or cooling. We omit the continuum cooling because it is not effective. This figure is taken from Bessho & Tsuribe (2012a).

### Low initial density and large line mass

In figure 4.1, the result for the rarefied filament model is shown for the case with large line mass and low initial density,  $(f, n_0, J_{21}) = (3, 10\text{cm}^{-3}, 0)$ . Compared with the uniform one-zone model in figure 3.1, the cloud fragments at lower density as expected. Density at fragmentation is  $5.0 \times 10^{-12}$  times that in the uniform model and effective radius of the filamentary cloud at the

moment of fragmentation is larger by  $5.1 \times 10^5$ . On the other hand, line mass is  $\tilde{l} = 2.1 \times 10^{-2}l$  at the moment of fragmentation. As a result of combination of these effects, fragment mass ( $127M_{\odot}$ ) is  $1.1 \times 10^3$  time larger than in the uniform one-zone model. The result of fragment mass still differs by about factor 4 from the previous result of the one-dimensional calculation (e.g., Nakamura & Umemura (2002)<sup>1</sup>). This is because even with the rarefied filament model, complete property of run-away collapse cannot be captured for the filamentary cloud with initial density profile with the density central concentration.

### High initial density and small line mass

Next, in figure 4.2, the result is shown for the case with small line mass and high initial density,  $(f, n_0, J_{21}) = (1.25, 10^6 \text{cm}^{-3}, 0)$ . Compared with the uniform one-zone model in figure 3.2, in the rarefied filament model, fragmentation density is  $3.2 \times 10^{-2}$  of that in the uniform one-zone model. Effective radius of the filamentary cloud at the moment of fragmentation is 5.6 times larger, but line mass at that moment is  $0.25l$ . As a result, fragment mass ( $64M_{\odot}$ ) is 1.4 times larger than in the uniform model.

In summary, figure 4.3 shows the fragment mass for various  $n_0$  and  $f$  in the case without the external radiation. All lines are similar to each other and can be approximated as  $M_{\text{frag}} \sim 30000n_0^{-0.3}f^{-4}$  with an error at most factor 2 at  $f = 3$ . Although fragment mass is still determined mainly by  $f$ , dependence on  $n_0$  becomes stronger than the uniform one-zone model. This tendency is close to the result of Nakamura & Umemura (2002).

## 4.2.2 Case with the external radiation

### Low initial density and small line mass

Let us show the result in the case with the external radiation. In figure 4.4, the result is shown for the case with small line mass, high initial density, and strong external radiation,

---

<sup>1</sup>Note also that fragmentation timescale of Nakamura & Umemura (2002) is longer by factor 2.5 than ours.

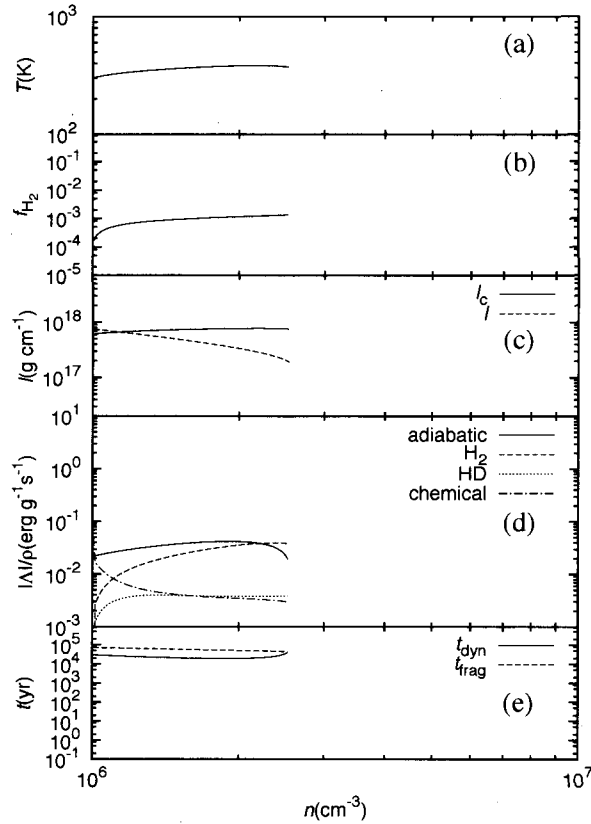


**Figure 4.2:** Same as figure 4.1, but  $(f, n_0, J_{21}) = (1.25, 10^6 \text{cm}^{-3}, 0)$ . This figure is taken from Bessho & Tsuribe (2012a).

$(f, n_0, J_{21}) = (1.25, 10 \text{cm}^{-3}, 10)$ . Compared with the uniform one-zone model in figure 3.5, in the rarefied filament model, fragmentation density is 0.65 of that in the uniform one-zone model. Effective radius of the filamentary cloud at the moment of fragmentation is 0.8 of the uniform filamentary cloud and the line mass at that moment is  $0.29l$ . As a result, fragment mass is 0.23 of that in the uniform one-zone model. Thus, fragment mass is smaller ( $\sim 2.6 \times 10^4 M_\odot$ ) due to smaller line mass, but is still larger than in the case without the external radiation.

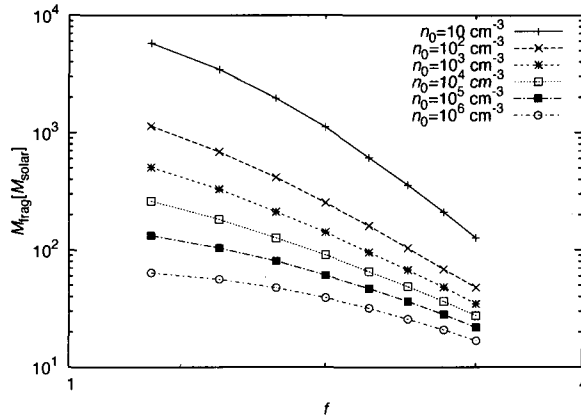


**Figure 4.3:** The fragment mass in the cases without the external radiation with various of  $n_0$  and  $f$  in rarefied filament model. This figure is taken from Bessho & Tsuribe (2012a).

### 4.2.3 Fragment mass

In summary, in figure 4.5 we plot contours maps of fragment mass in  $n_0 - f$  plane for the cases with  $J_{21} = 0, 1, 6.5,$  and  $10$ . Solid lines in each diagram represent constant fragment mass. Comparing diagram (b), (c), and (d) with diagram (a), it is seen that fragment mass for the cases with low initial density ( $n_0 < 10^{2-2.5} \text{cm}^{-3}$ ) is strongly affected by the external radiation. In the cases with these low  $n_0$ , fragment mass is mainly determined by  $n_0$  instead of  $f$  and massive fragments form in the cases with  $J_{21} \geq 1$ . In the cases with high initial density ( $n_0 > 10^3 \text{cm}^{-3}$ ), the fragment mass is approximately independent of the external radiation. In the cases with high initial density, the filamentary cloud shields itself from the dissociation photon from the early stage of collapse, and the effect of photodissociation is minor important.

We comment on the effects of run-away collapse. By comparing figure 4.5 with figure 3.7, these effects are clearly noticed. The most remarkable difference is that strong dependence on  $f$  in figure 3.7 becomes weaker in figure 4.5. Furthermore, sub-solar fragments seen in figure 3.7 are not found in figure 4.5. Thus, we suspect that too small mass of fragments in figure 3.7 is the result of too idealized modeling with the uniform filamentary cloud in previous sections.

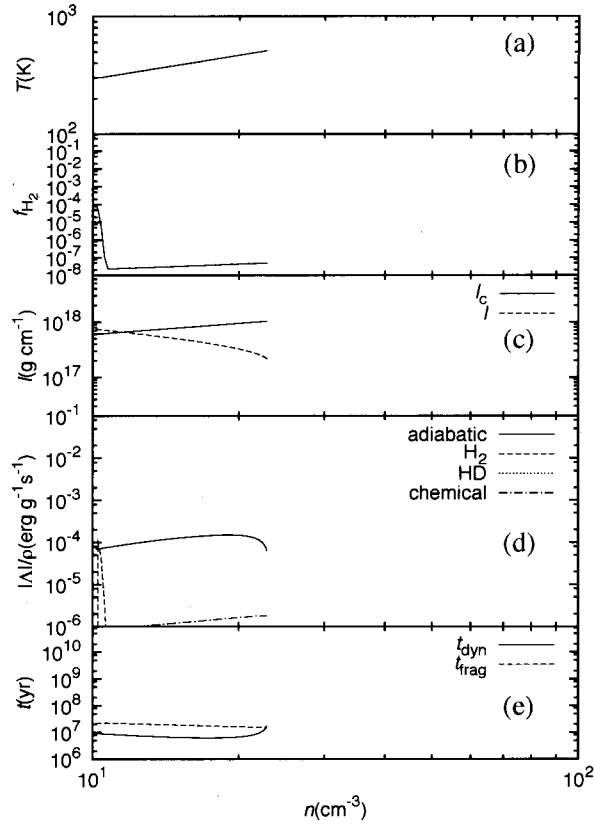


**Figure 4.4:** Same as figure 4.1, but for the rarefied filament model,  $(f, n_0, J_{21}) = (1.25, 10\text{cm}^{-3}, 10)$ . This figure is taken from Bessho & Tsuribe (2012a).

However, in both of figure 4.5 and figure 3.7, massive fragments are seen in the cases with low initial density ( $n_0 < 10^2\text{cm}^{-3}$ ) and  $J_{21} (> 1)$ . Thus, formation of massive fragment with the external radiation can be regarded as a robust result.

### 4.3 Summary of the rarefied filament model

With  $J_{21} \geq 1$ , the filamentary cloud with low initial density ( $n_0 \leq 10^2\text{cm}^{-3}$ ) fragments into very massive clouds with  $\sim 10^4 M_\odot$ . This feature was seen also in the uniform one-zone model (figure 3.7). However, only in the rarefied filament model, the filamentary cloud with

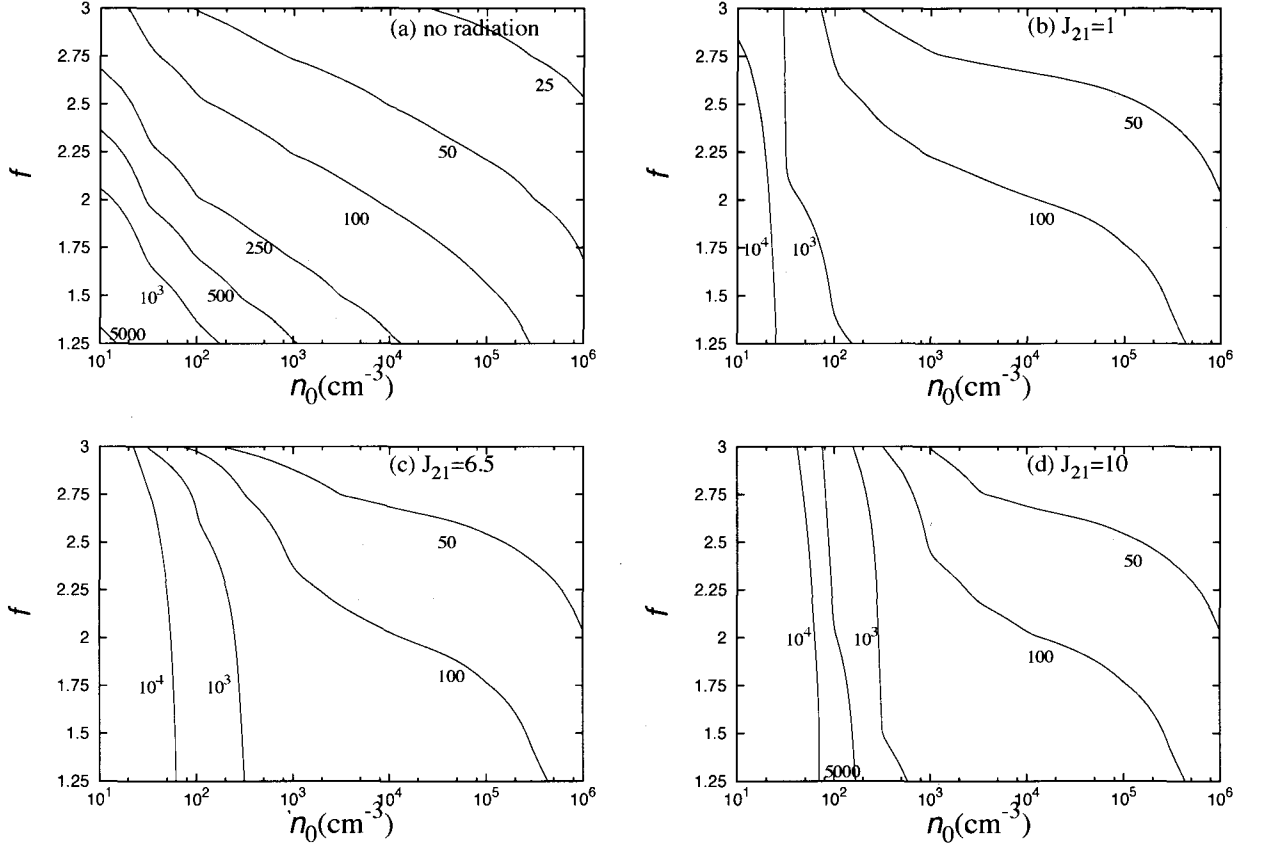


**Figure 4.5:** The contours maps for the fragment mass for the cases with (a)  $J_{21} = 0$ , (b)  $J_{21} = 1$ , (c)  $J_{21} = 6.5$ , and (d)  $J_{21} = 10$ . The number attached to each solid line is mass of fragment in units of  $M_{\odot}$ . This figure is taken from Bessho & Tsuribe (2012a).

low initial density and large  $f$  fragments into very massive clouds. With high initial density ( $n_0 > 10^2 \text{cm}^{-3}$ ), the evolution of the filamentary cloud is hardly affected by the external radiation both in the uniform and rarefied filament model since the filamentary cloud shields itself from the external radiation.

Since line mass decreases as rarefaction wave propagates, most of the rarefied filamentary clouds fragment at lower density than the uniform one-zone model. This effect is found to have stronger effect than the decreasing of line mass. Hence, fragment mass usually becomes larger.

As a result, sub-solar fragments seen in uniform one-zone model are not found in rarefied filament model. In addition, it is clearly seen that the difference between figure 4.5 and figure 3.9 (one-dimensional model; Nakamura & Umemura 2002) becomes much smaller than that between figure 3.7 (uniform model) and figure 3.9. Thus, in order to estimate fragment mass correctly, it is important to capture the effect run-away collapse.

## 4.4 Problems of rarefied filament model

In this chapter, we assumed that in initial state the filamentary cloud is uniform. However, this is not obvious, and the initial density profile of the filamentary cloud is more realistically expected to have core-envelope structure since the filamentary cloud forms as a result of dynamical evolution. Other than the initial condition, we approximate the speed of rarefaction wave to be the sound speed at the center. This may underestimate speed of rarefaction wave since the dense central region has stronger cooling ability than the outer envelope. Actually, speed of rarefaction wave depends on local temperature at rarefaction wave front. We also assumed that fraction of  $\text{H}_2$  in the filamentary cloud is uniform and decreases simultaneously in whole cloud when the filamentary cloud suffers photodissociation. Since the envelope actually suffers photodissociation earlier than the central region, fraction of  $\text{H}_2$  is expected not to be spatially uniform. In order to resolve the problems mentioned above, we need to use the one-dimensional hydrodynamical model as shown in the next chapter.



# Chapter 5

## Numerical results III : one-dimensional model

As pointed at the end of Chapter 4, the rarefied filament model still includes approximations in which density, fraction of H<sub>2</sub>, and temperature are treated as constant. In order to solve this problem, in this chapter, we use one-dimensional model. We can capture the full effect of run-away collapse and can estimate fragment mass quantitatively as well as Nakamura & Umemura (2001, 2002). The contents in this chapter are based on Bessho & Tsuribe (2012b).

### 5.1 Modification to the model

#### 5.1.1 Basic equations

Instead of the virial equation, we calculate dynamical evolution by solving hydrodynamical equation of motion in Lagrangian form,

$$\frac{Dv}{Dt} = -\frac{2Gl}{r} - 2\pi r \frac{\partial P}{\partial l}, \quad (5.1)$$

where  $v$  is the velocity in the cylindrical radial direction,  $l$  is the line mass within cylindrical radius  $r$ , and  $P$  is the pressure for ideal gas given by

$$P = \frac{\rho k_B T}{\mu m_H}. \quad (5.2)$$

We solve Eq.(5.1) in the 2nd-order finite-difference scheme with von Neumann Richtmyer artificial viscosity (cf. Thoul & Weinberg 1995). We test our code for one-dimensional model in Appendix G.

As for transfer of radiation, we consider that the escape probability for emission from the transition between level  $i$  and  $j$  is defined as

$$\beta_{ij} = \frac{1 - e^{-\tau_{ij}}}{\tau_{ij}}, \quad (5.3)$$

with assuming the velocity profile  $v_r(r) \propto r$  (Castor 1970). The cooling rate for optically thin medium is multiplied by this escape probability. Optical depth,  $\tau_{ij}$ , is given by

$$\begin{aligned} \tau_{ij} &= \int_r^{R_{\text{out}}} \kappa_{ij}(r') dr' \\ &= \int_r^{R_{\text{out}}} \frac{h\nu_{ij}}{8\pi\Delta\nu_{ij}} (n_j B_{ji} - n_i B_{ij}) dr', \end{aligned} \quad (5.4)$$

where  $R_{\text{out}}$  is radius of the outer boundary,  $\kappa_{ij}$  is opacity for lines,  $h\nu_{ij}$  is energy difference between levels  $i$  and  $j$ ,  $n_i$  ( $n_j$ ) is the level population at level  $i$  ( $j$ ),  $B_{ij}$  and  $B_{ji}$  are the Einstein  $B$ -coefficients, and  $\Delta\nu_{ij} = \nu_{ij}/c\sqrt{2k_B T/\mu m_H}$  is the thermal Doppler width of transition line  $i \rightarrow j$ .

We calculate Eq.(5.1), equation of thermal energy, non-equilibrium chemical reactions<sup>1</sup>, and escape probability using 200 spatial meshes in cylindrical radial direction. As for initial radius of meshes, we set to  $\Delta r_{i+1} = 1.01\Delta r_i$ , where  $\Delta r_i \equiv r_{i+1} - r_i$ . Hence, we calculate the central region in detail. The mesh size  $\Delta r_i$  is checked to be shorter than 1/4 of local Jeans

<sup>1</sup>As for chemical reactions associated with H and He, we consider 26 chemical reactions taken from Nakamura & Umemura (2001).

length at all times. We set outer boundary to be  $10R_0$  as a sufficiently large value, where  $R_0$  is the effective radius given by

$$R_0 = \sqrt{\frac{2fk_B T_0}{\pi G \mu m_H \rho_{0,c}}}, \quad (5.5)$$

where  $f$  is line mass parameter,  $T_0$  is initial temperature, and  $\rho_{0,c}$  is initial density at the center.

### 5.1.2 External radiation

We calculate the photodissociation reaction of  $H_2$  with self-shielding function (see Eq.(2.16)) at each point. For simplicity, we treat the external dissociating radiation in the radial direction using the column density given by

$$N_{H_2}(r) = \int_r^{R_{out}} n_{H_2}(r') dr'. \quad (5.6)$$

### 5.1.3 Fragmentation of the filamentary cloud

We modify the way to estimate fragment mass. We estimate fragment mass using line mass of the dense central region as

$$M_{frag} = \lambda_{frag} \int_0^{r(\rho=0.1\rho_c)} 2\pi r' \rho dr', \quad (5.7)$$

where

$$\lambda_{frag} = 2\pi \frac{\sqrt{\gamma_{adi}(\gamma_{adi} - 1)u}}{0.288\sqrt{4\pi G\rho}} \quad (5.8)$$

is the wave length of the fastest growing mode (Nagasawa 1987). Since  $\lambda_{frag} \propto \rho^{-1/2}$ , fragment mass is smaller when the filamentary cloud reaches higher density before fragmentation. Since interval of integration in Eq.(5.7) is approximately Jeans length, Jeans mass at fragmentation is close to fragment mass (see §5.2.3).

### 5.1.4 Parameters and initial conditions

In this chapter, we treat  $n_0$ ,  $f$ , and  $J_{21}$  as parameters. We consider cases with  $\log_{10} n_0 = 1, 1.5, 2, 2.5, 3, 3.5, 4, 4.5, 5, 5.5,$  and  $6$  and  $f = 1.5, 2, 2.5, 3, 3.5, 4, 5.5,$  and  $6$ . For  $J_{21}$ , we consider  $J_{21} = 0, 1, 6.5,$  and  $10$  as in Chapter 3 and 4. We assume that the external radiation turns on when the filamentary clouds form.

We set the initial density distribution as

$$\rho(r) = \rho(0) \left( 1 + \frac{r^2}{R_0^2} \right)^{-2} \quad (5.9)$$

with  $R_0$  given in Eq.(5.5). For  $f = 1$ , Eq.(5.9) represents dynamically equilibrium distribution for the isothermal filamentary cloud (Ostriker 1964; Appendix A). In this chapter, we restrict the case with  $f > 1$  since we are interested in collapsing filamentary clouds. Initial velocity distribution is assumed to be

$$v(r) = -\frac{c_s}{R_0 + \sqrt{R_0^2 + r^2}} r, \quad (5.10)$$

where  $c_s$  is sound speed. Although the actual initial velocity may depend on the formation process of the filamentary cloud, the results of the filament collapse will not change qualitatively unless initial velocity is much larger than a few times sound speed.

## 5.2 Numerical results

### 5.2.1 Cases without the external radiation

To investigate the effect of the external radiation, at first, we show the results of the cases without the external radiation.

#### Low initial density and small line mass

First, we show the results for the case with low initial density and small line mass,  $(f, n_0, J_{21}) = (1.5, 10\text{cm}^{-3}, 0)$  (figure 5.1). In the early stage of collapse,  $\text{H}_2$  cooling dominates adiabatic

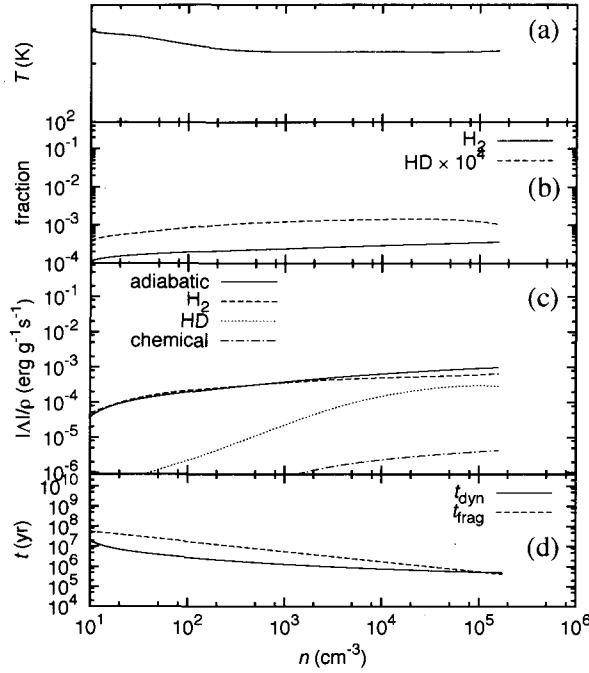


**Figure 5.1:** Evolution of the temperature (a),  $f_{\text{H}_2}$  and  $f_{\text{HD}} \times 10^4$  (b), the heating and cooling rate (c) (adiabatic heating,  $\text{H}_2$  cooling rate, HD cooling rate, and chemical heating/cooling rate), and  $t_{\text{dyn}}$  and  $t_{\text{frag}}$  (d), respectively, as a function of the central density for case with  $(f, n_0, J_{21}) = (1.5, 10\text{cm}^{-3}, 0)$ . This figure is taken from Bessho & Tsuribe (2012b).

heating a little, and temperature decreases. After the density reaches  $n \sim 10^3\text{cm}^{-3}$ , adiabatic heating dominates  $\text{H}_2$  cooling. In  $n > n_{\text{crit}} \sim 10^4\text{cm}^{-3}$ ,  $\text{H}_2$  cooling rate is proportional to  $n$  while it is proportional to  $n^2$  in  $n < n_{\text{crit}}$ . Hence, since cooling time becomes constant in  $n > n_{\text{crit}}$ <sup>2</sup>, dynamical time becomes constant and longer than fragmentation time. When  $n$  reaches  $\sim 2 \times 10^5\text{cm}^{-3}$ , condition for fragmentation is satisfied with  $M_{\text{frag}} \sim 1220M_{\odot}$ . To ensure that fragmentation occurs, we continue to calculate the evolution until free-fall time has past after the condition for fragmentation is first satisfied. We confirmed that once condition for fragmentation is satisfied, it is kept to be satisfied.

<sup>2</sup>Beyond critical density  $n_{\text{crit}}$ , LTE populations are achieved for the rotational levels of  $\text{H}_2$ .

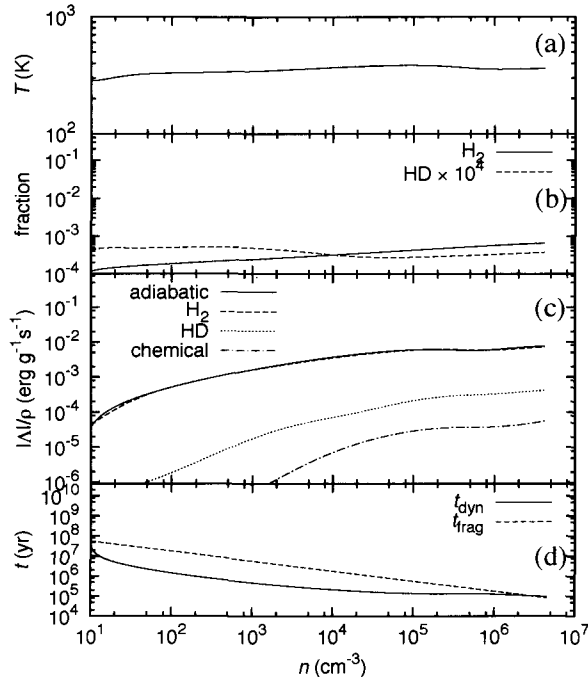


**Figure 5.2:** Same as figure 5.1, but  $(f, n_0, J_{21}) = (6, 10\text{cm}^{-3}, 0)$ . This figure is taken from Bessho & Tsuribe (2012b).

### Low initial density and large line mass

Next, we show the result for the case with low initial density and large line mass,  $(f, n_0, J_{21}) = (6, 10\text{cm}^{-3}, 0)$  (figure 5.2). Owing to larger line mass, the filamentary cloud collapses to higher density than in figure 5.1. Collapse continues up to high density ( $n \sim 10^6\text{cm}^{-3}$ ), and the filamentary cloud fragments. Fragment mass is  $\sim 490M_{\odot}$ . Until fragmentation, adiabatic heating and  $\text{H}_2$  cooling balance, and temperature is approximately constant ( $T \sim 350\text{K}$ ).

### High initial density and small line mass

As the final example, we show the result for the case with high initial density and small line mass,  $(f, n_0, J_{21}) = (1.5, 10^6\text{cm}^{-3}, 0)$  (figure 5.3). In the early stage of collapse, adiabatic

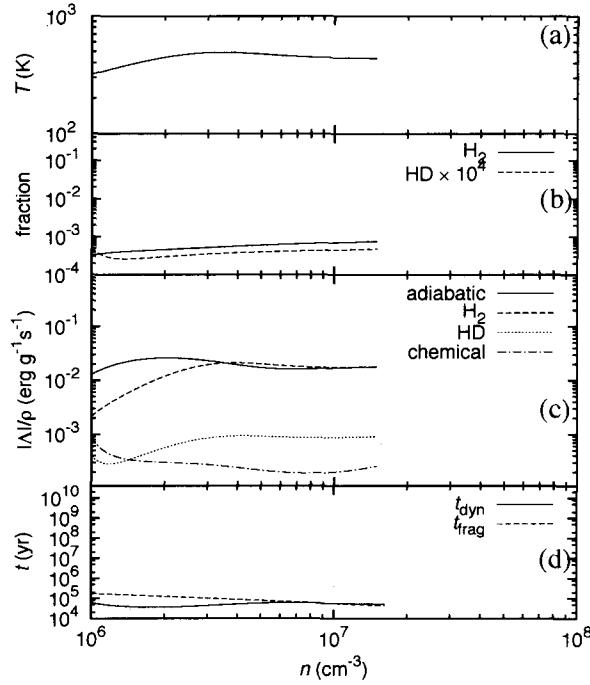


**Figure 5.3:** Same as figure 5.1, but  $(f, n_0, J_{21}) = (1.5, 10^6 \text{cm}^{-3}, 0)$ . This figure is taken from Bessho & Tsuribe (2012b).

heating dominates  $\text{H}_2$  cooling and temperature increases. During collapse,  $\text{H}_2$  cooling rate increases and approximately balances with adiabatic heating rate at  $n \sim 3 \times 10^6 \text{cm}^{-3}$ . After temperature decreases a little, fragmentation condition is satisfied at  $n \sim 10^7 \text{cm}^{-3}$  since collapse is suppressed owing to high temperature. Fragment mass is  $\sim 370 M_\odot$ .

In summary, in the cases without the external radiation, the filamentary cloud undergoes approximately isothermal states and fragments. This feature comes from the fact that  $\text{H}_2$  cooling and adiabatic heating compete each other. The results in this subsection are similar to previous works (Nakamura & Umemura 2001, 2002). For the same parameter set as figure 5.1, fragment mass was  $23 M_\odot$  in the uniform model and  $3500 M_\odot$  in rarefied filament model as shown in Chapters 3 and 4. Fragment mass  $1220 M_\odot$  in the one-dimensional model is close to the results of the rarefied filament model. This result indicates that the effect of run-away

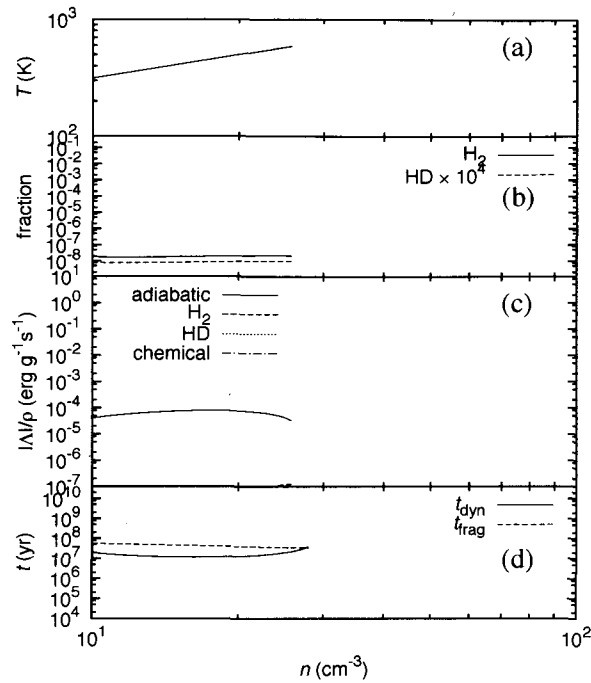


**Figure 5.4:** Same as figure 5.1, but  $(f, n_0, J_{21}) = (1.5, 10\text{cm}^{-3}, 10)$ . This figure is taken from Bessho & Tsuribe (2012b).

collapse is important to estimate fragment mass.

## 5.2.2 Cases with the external radiation

In this subsection, using the same parameters as figures 5.1-5.3, we investigate how the external radiation changes the thermal evolution and fragment mass of the filamentary cloud.

### Low initial density and small line mass with strong radiation

First, we show the result for the case with low initial density, small line mass, and strong external radiation,  $(f, n_0, J_{21}) = (1.5, 10\text{cm}^{-3}, 10)$  (figure 5.4), where the external radiation is added to the case of figure 5.1. This case would be affected by the external radiation because

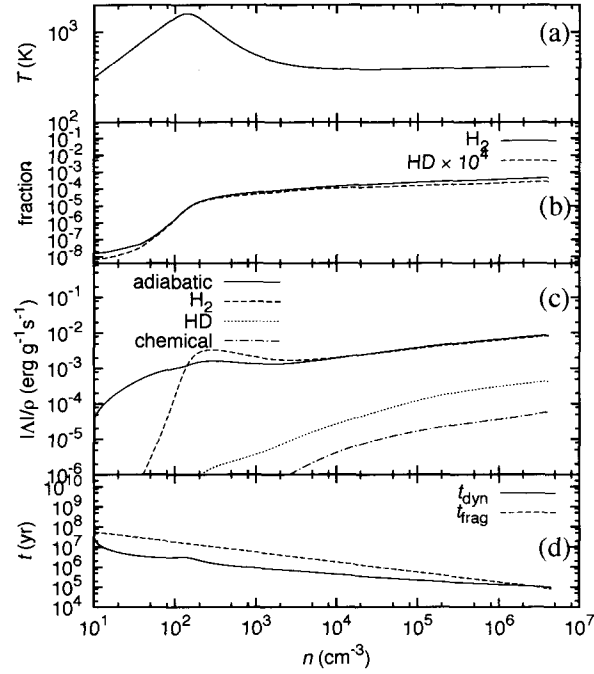


**Figure 5.5:** Same as figure 5.1, but  $(f, n_0, J_{21}) = (6, 10\text{cm}^{-3}, 10)$ . This figure is taken from Bessho & Tsuribe (2012b).

of low density. Most of  $\text{H}_2$  are photodissociated in the early stage of collapse, and temperature increases adiabatically. The filamentary cloud fragments into very massive fragments ( $\sim 2.4 \times 10^5 M_\odot$ ) at  $n \sim 30\text{cm}^{-3}$ . This result demonstrates that the filamentary cloud with low initial density and small line mass fragments into more massive fragments and its thermal evolution changes under the external dissociating radiation.

### Low initial density and large line mass with strong radiation

Next, we show the result for the case with low initial density, large line mass, and strong external radiation,  $(f, n_0, J_{21}) = (6, 10\text{cm}^{-3}, 10)$  (figure 5.5), where the external radiation is added to the case of figure 5.2. This case is also expected to be affected by the external radiation because of low density. However, the filamentary cloud may collapse up to higher

density than in figure 5.4 because of large line mass. In figure 5.5, it is seen that most of  $H_2$  is photodissociated in the early stage of collapse and temperature increases adiabatically as in figure 5.4. However, since the filamentary cloud is more massive than in figure 5.4, stronger gravity and large inertia help collapse. Fragmentation does not occur during early adiabatic phase, and collapse continues until the density becomes higher than in figure 5.4. At  $n \sim 10^2 \text{cm}^{-3}$ ,  $H_2$  starts to form and shields itself from the external radiation. Then, the filamentary cloud starts to cool owing to  $H_2$  cooling. After  $n \sim 10^3 \text{cm}^{-3}$ , since  $H_2$  cooling balances with adiabatic heating, temperature becomes nearly constant ( $T \sim 400\text{K}$ ). The filamentary cloud fragments into clouds with  $\sim 590M_\odot$  at  $n \sim 10^6 \text{cm}^{-3}$ . Fragment mass and density at fragmentation are similar to the case without the external radiation (figure 5.2). In the case with large line mass ( $f = 6$ ), it is found that fragment mass is hardly affected by the external radiation although the evolution of temperature is affected by the external radiation in the early stage of collapse.

### High initial density and small line mass with strong radiation

Finally, we show the result for the case with high initial density, small line mass, and strong external radiation,  $(f, n_0, J_{21}) = (1.5, 10^6 \text{cm}^{-3}, 10)$  (figure 5.6), where the external radiation is added to the case of figure 5.3. In this case, the thermal evolution may not be affected by the external radiation because of high density. Since initial density is high enough to shield the filamentary cloud from the external radiation, in figure 5.6,  $H_2$  near the center of cloud is not photodissociated. The evolution of temperature is similar to figure 5.3. Hence, in this case, it is found that the thermal evolution is hardly affected by the external radiation. The filamentary cloud fragments into clouds with  $\sim 400M_\odot$  at  $n \sim 10^7 \text{cm}^{-3}$ . It is found that the effect of the external radiation is not important in the case with high initial density ( $n_0 = 10^6 \text{cm}^{-3}$ ).

In summary, in the case with low initial density ( $n_0 < 10^2 \text{cm}^{-3}$ ), the filamentary cloud suffers photodissociation in the early stage of collapse. In such case, temperature increases adiabatically. The filamentary cloud with small line mass ( $f = 1.5$ ) fragments during adiabatic

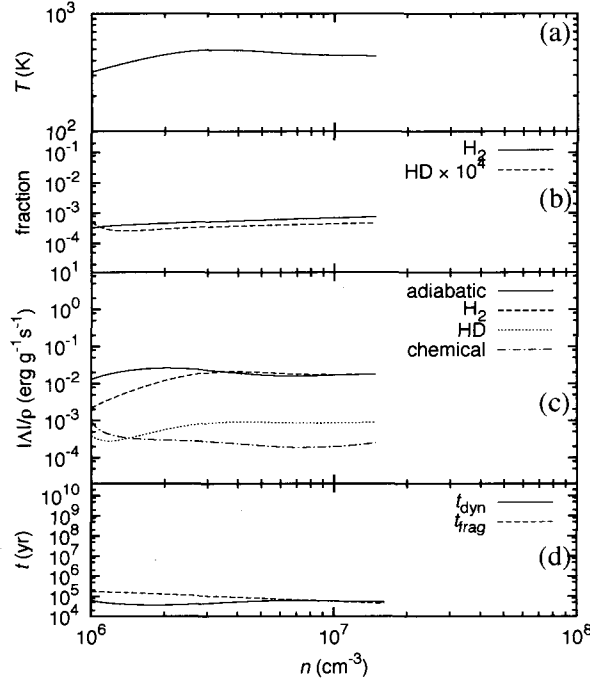


**Figure 5.6:** Same as figure 5.1, but  $(f, n_0, J_{21}) = (1.5, 10^6 \text{cm}^{-3}, 10)$ . This figure is taken from Bessho & Tsuribe (2012b).

phase. On the other hand, the filamentary cloud with large line mass ( $f = 6$ ) does not fragment during adiabatic phase and collapses with shielding itself from the external radiation. In this case, fragment mass is hardly affected by the external radiation. In the case with high initial density ( $n_0 = 10^6 \text{cm}^{-3}$ ), the thermal evolution of the filamentary cloud is hardly affected by the external dissociating radiation.

One-zone model predicts fragment mass different from what one-dimensional model predicts. For example, for the same parameter set as figure 5.4, uniform one-zone model predicted  $1.5 \times 10^5 M_\odot$  and rarefied model predicted  $2.7 \times 10^4 M_\odot$  as shown in Chapters 3 and 4. One-dimensional model predicts  $2.4 \times 10^5 M_\odot$ . Difference between one-zone models and one-dimensional model originates from difference of dynamical equation (virial equation in one-zone model and hydrodynamical equation of motion in one-dimensional model). In one-

dimensional model, collapse proceeds in run-away fashion, and fragmentation condition is satisfied at lower density since line mass of small central region decreases as cloud collapses. Hence, in one-dimensional model, fragment mass becomes larger than in uniform one-zone model.

### 5.2.3 Property of the filamentary cloud at fragmentation

In this subsection, we show the profile of physical quantities (density, temperature, in-fall velocity, and ratio of pressure gradient to gravitational force) at the moment of fragmentation. We focus on density profile and investigate whether or not the universal profile at the moment of fragmentation exists. Moreover, we compare fragment mass (Eq.5.7) with the Jeans mass estimated with the central density and temperature.

#### Case without the external radiation

We show the profiles of density, temperature, infall velocity, and ratio of pressure gradient to gravitational force at the moment of fragmentation in the case with  $(f, n_0, J_{21}) = (1.5, 10\text{cm}^{-3}, 0)$  in figure 5.7. In diagram (a) of figure 5.7, it is seen that dense central region within Jeans length ( $\lambda_J \sim 2.3 \times 10^{18}\text{cm}$ ) has uniform density, and the density profile in the outer envelope is proportional to  $r^{-4}$ . This density profile is similar to that of equilibrium solution for the isothermal filamentary cloud (Ostriker 1967). However, between  $r = 10^{19}\text{cm}$  and  $r = 10^{20}\text{cm}$ , slope of the density profile is shallower than  $r^{-4}$ . Temperature is highest outside  $r_{\text{cool}} \sim 2 \times 10^{18}\text{cm}$  where  $t_{\text{cool}} = t_{\text{ff}}$ , and pressure gradient force is stronger than gravitational force around  $r_{\text{cool}}$ . Hence, matter is pushed outwards and it is decelerated. Ratio of pressure gradient to gravity is nearly 1 ( $\sim 1.01$ ) inside  $r_{\text{cool}}$ . Velocity profile is in proportion to radius in the central dense region and is *constant* which is larger than sound speed in the outer envelope. In diagram (b), drop of temperature at the surface ( $r \sim 10^{21}\text{cm}$ ) is seen. Since we assume that the external pressure is zero, adiabatic cooling occurs at several meshes near the

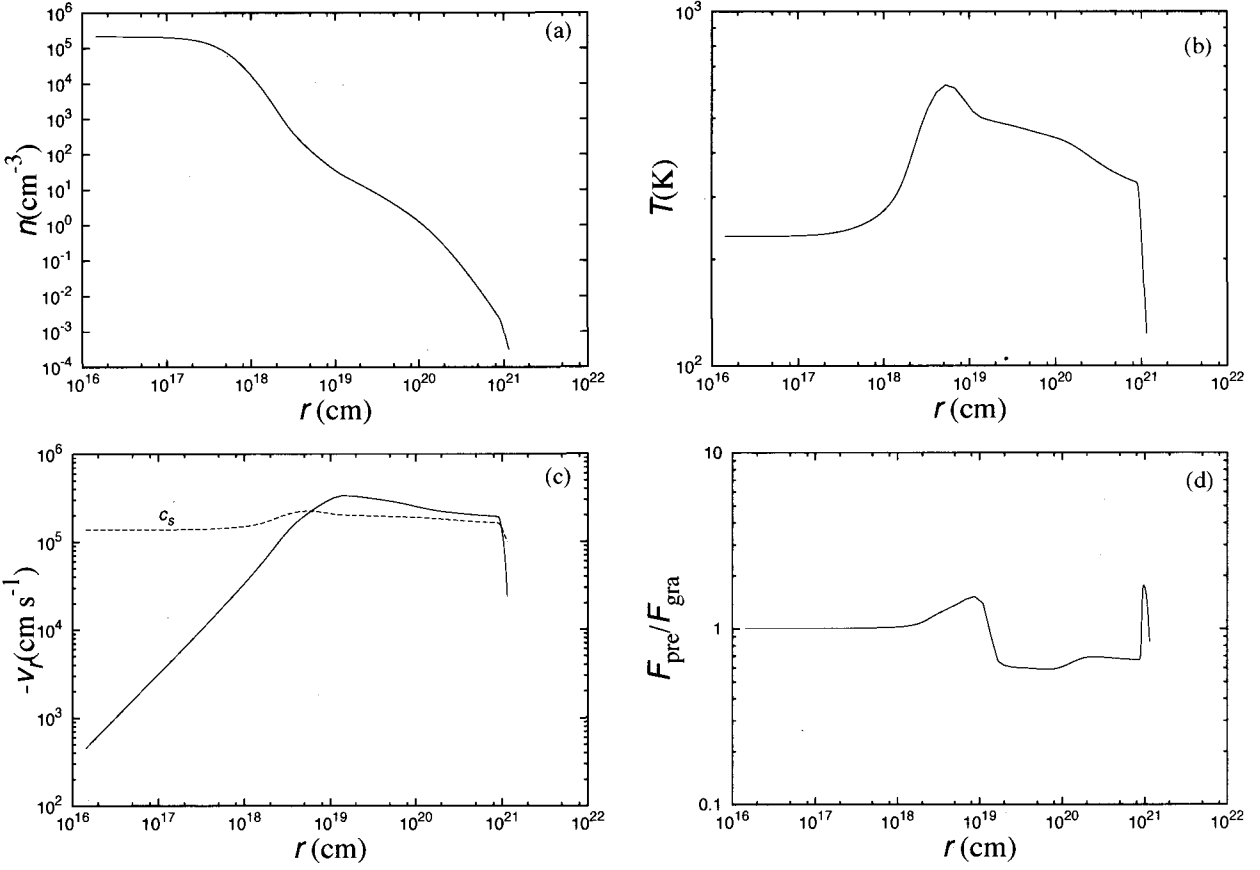


**Figure 5.7:** Density profile (a), profile of temperature (b), velocity profile (c), and ratio of pressure gradient to gravity (d) at the moment of fragmentation in the case with  $(f, n_0, J_{21}) = (1.5, 10\text{cm}^{-3}, 0)$ . This figure is taken from Bessho & Tsuribe (2012b).

surface. Moreover, these meshes are pushed outwards by inner meshes with higher pressure and fall more slowly than inner meshes. However, these effects do not affect the central region. Predicted mass of each fragment is  $1220M_{\odot}$  which is close to Jeans mass ( $1140M_{\odot}$ ) estimated from central density and temperature. Since  $t_{\text{dyn}}$  is found to be about 6 times of  $t_{\text{ff}}$  at the center when the filamentary cloud fragments, pressure gradient force has an important role in the further evolution of fragments. Further evolution of each fragment is shown in Chapter 6.

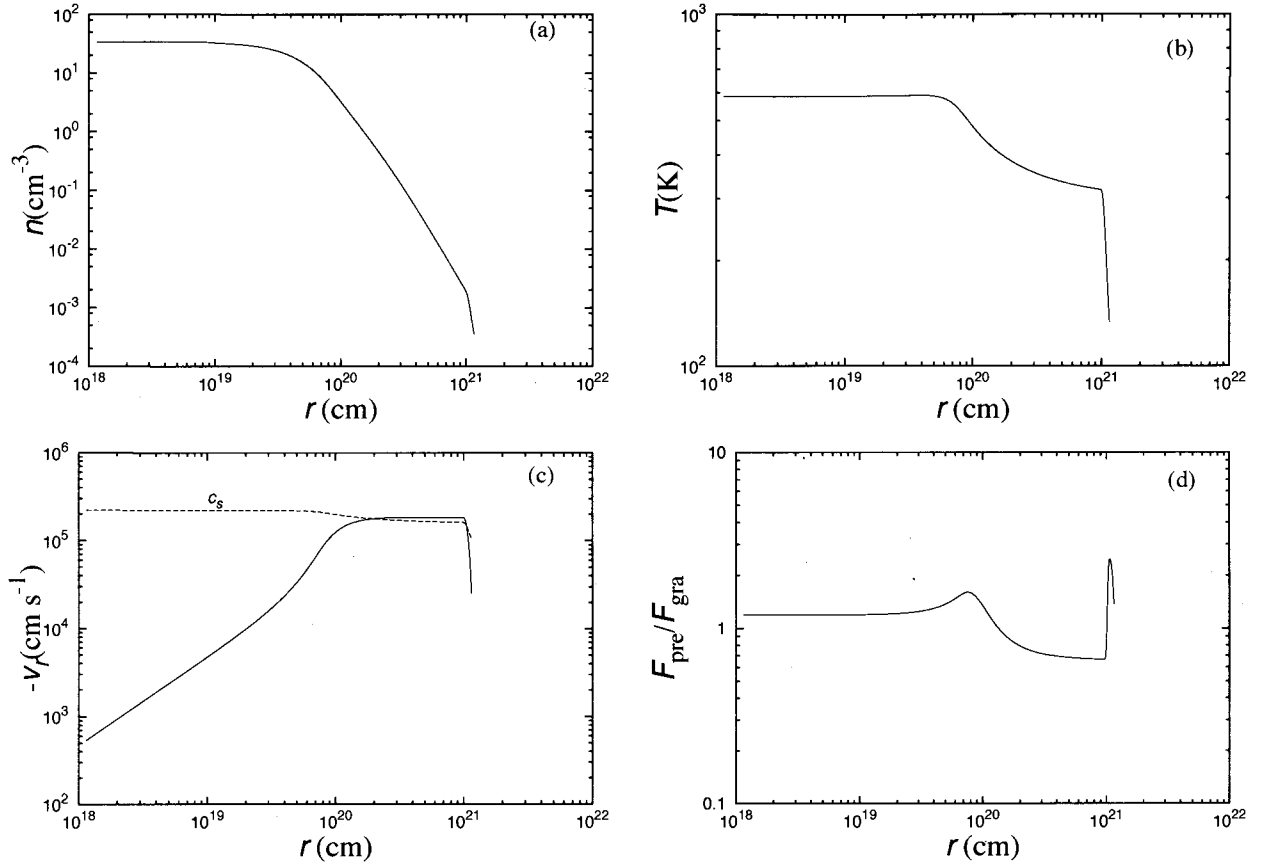


**Figure 5.8:** Same as figure 5.7, but  $(f, n_0, J_{21}) = (1.5, 10\text{cm}^{-3}, 10)$ . This figure is taken from Bessho & Tsuribe (2012b).

### Case with the external radiation

We show profiles of the same quantities as figure 5.7 for the case with  $(f, n_0, J_{21}) = (1.5, 10\text{cm}^{-3}, 10)$  in figure 5.8. In figure 5.8, it is seen that except for temperature, profiles of physical quantities are similar to figure 5.7. Most of  $\text{H}_2$  is photodissociated, and the filamentary cloud has lost the ability to cool. Hence, temperature is higher in the central dense region than in the outer envelope. Ratio of pressure gradient to gravity is larger than 1 ( $\sim 1.2$ ). Predicted mass of each fragment is  $2.4 \times 10^5 M_\odot$  which is close to Jeans mass ( $3.0 \times 10^5 M_\odot$ ) estimated from central density and temperature. In the case with the external radiation, since  $t_{\text{dyn}}$  is found to be

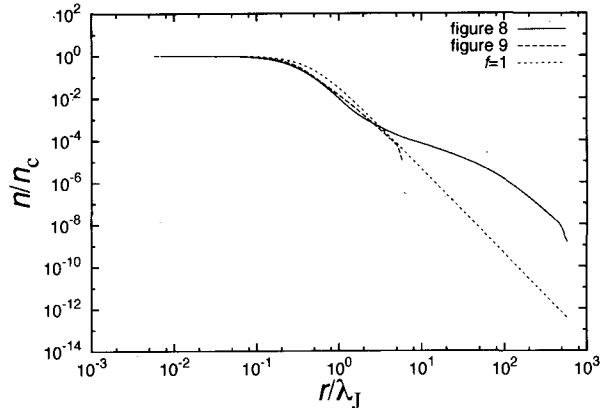


**Figure 5.9:** Normalized density profile for the case in figure 5.7 (solid line) and in figure 5.8 (dashed line). The initial density profile for the case with  $f = 1$  is also shown (dotted line). The symbol  $n_c$  is central density and  $\lambda_J$  is Jeans length at the center. This figure is taken from Bessho & Tsuribe (2012b).

about 5 times of  $t_{\text{ff}}$  at the center when the filamentary cloud fragments, pressure gradient force has an important role in the further evolution of fragments (see Chapter 6). In figure 5.9, the density profiles in figure 5.7 and 5.8 are simultaneously plotted with normalized  $n$  and  $r$ . Each profile is found to be similar to each other. The profiles at  $r/\lambda_J < 0.5$  are similar to the profile of isothermal filamentary cloud in equilibrium state.

#### 5.2.4 Fragment mass

We show how much the external dissociating radiation changes fragment mass. Figure 5.10 shows the fragment mass for all the parameters in  $n_0 - f$  plane using contours. Results for the cases with  $J_{21} = 0, 1, 6.5, \text{ and } 10$  are presented in different diagrams. In the case with the external radiation, it is seen that the filamentary clouds fragment into very massive clouds ( $> 10^5 M_\odot$ ) in the cases with low initial density ( $n_0 \leq 10^2 \text{ cm}^{-3}$ ). Since very massive fragments are not seen in the case without the external radiation, this can be regarded as a result of the effect of the dissociation photon. This feature is qualitatively the same as the result of the

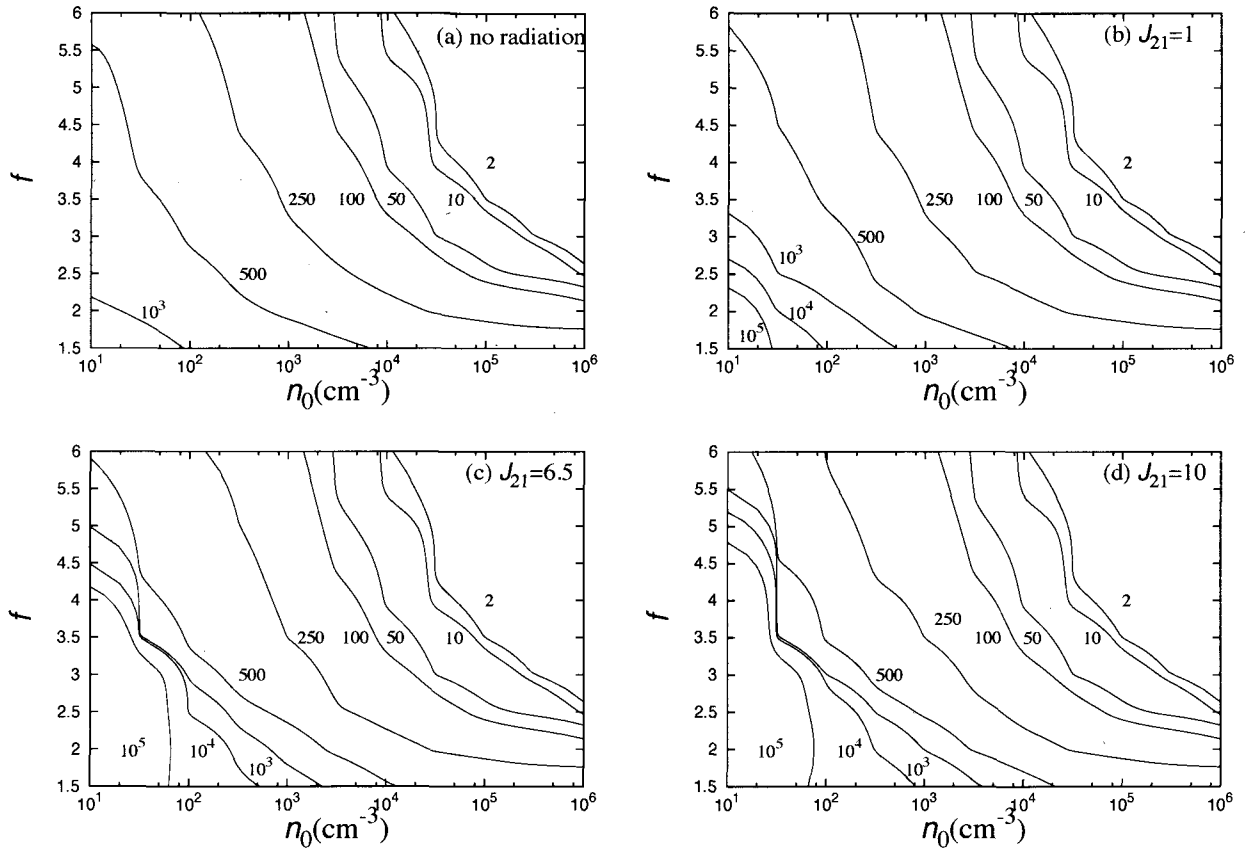


**Figure 5.10:** The contours maps for the fragment mass for the case with (a)  $J_{21} = 0$ , (b)  $J_{21} = 1$ , (c)  $J_{21} = 6.5$ , and (d)  $J_{21} = 10$ . The number near each solid line is mass of fragment in units of  $M_{\odot}$ . This figure is taken from Bessho & Tsuribe (2012b).

one-zone models in Chapter 3 and 4. Thus, formation of very massive fragments under the external radiation with moderate intensity can be regarded as the robust result, provided that the external radiation turns on when the filamentary cloud forms.

The diagram (a) of figure 5.10 is similar to figure 3.9. In the range of  $2 - 100M_{\odot}$ , the contours are dense. This is because the filamentary cloud becomes isothermal once  $H_2$  cooling becomes effective owing to three body reaction, and continues to collapse to high density ( $n \sim 10^{13}\text{cm}^{-3}$ ). In such a case, fragment mass is small ( $\sim 2 - 10M_{\odot}$ ). This feature is

consistent with the result of Nakamura & Umemura (2002).

Nakamura & Umemura (2002) concluded that there are some parameter sets where HD is main coolant. In our results, HD is found not to be important. Since initial  $\text{H}_2$  fraction in this paper is assumed to be small ( $10^{-4}$ ) and HD mainly forms from  $\text{H}_2$ ,<sup>3</sup> sufficient amount of HD to cool does not form even in the case without the external radiation. This result is consistent with Nakamura & Umemura (2002). In the case with the external radiation, since  $\text{H}_2$  is photodissociated, HD is less important.

We show the effect of the external radiation on fragment mass quantitatively. Figure 5.11 shows the similar contours in figure 5.10 but about the ratio of the fragment mass between the cases with and without the external radiation. In addition to figure 5.10, figure 5.11 clearly shows that the filamentary clouds with low initial density ( $n_0 \leq 10^2 \text{cm}^{-3}$ ) and moderate line mass ( $f < 4.5$ ) fragment into more massive fragments than the case without the external radiation. This feature agrees with the results of the rarefied filament model in Chapter 4.

In figure 5.11, it is seen that fragment mass for the case with high initial density ( $n_0 > 10^2 \text{cm}^{-3}$ ) does not increase owing to the external dissociating radiation. This is because the initial density is high enough for the filamentary cloud to shield itself from the external dissociating radiation. In this case, the evolution is similar to the case without the external radiation.

Recently, Wolcott-Green et al. (2011) have proposed the new self-shielding function. To discuss accuracy of the shielding function, we calculate the evolution of the filamentary cloud with this new shielding function in some cases (see Appendix H in detail). We found that the main conclusion in this chapter does not change by using different form of shielding function.

---

<sup>3</sup>Main chemical reaction of formation of HD is given by



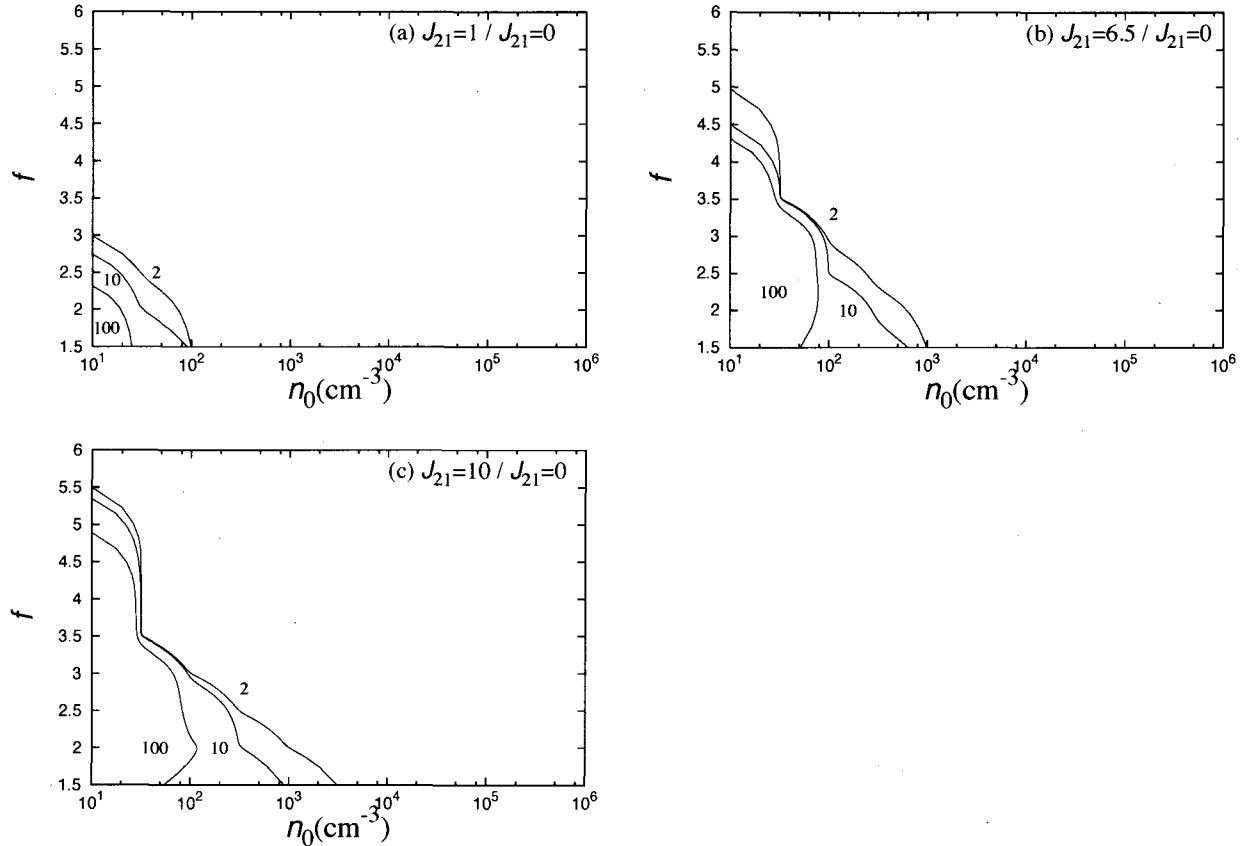


**Figure 5.11:** The ratio of the fragment mass with the external radiation ((a)  $J_{21} = 1$ , (b)  $J_{21} = 6.5$ , and (c)  $J_{21} = 10$ ) to that without the external radiation ( $J_{21} = 0$ ). The number near each solid line is the ratio of fragment mass. This figure is taken from Bessho & Tsuribe (2012b).

### 5.3 Summary of the one-dimensional model

In this chapter, collapse and fragmentation of primordial filamentary cloud is investigated using one-dimensional hydrodynamical calculations with the effect of the external dissociating radiation. Especially, the effect of run-away collapse to fragment mass is considered by comparing with previous results with one-zone models. Results are summarized as follows :

- Comparing with the uniform one-zone model in Chapter 3, one-dimensional model pre-

dicts lower fragmentation density and larger fragment mass. This is because fragmentation occurs in smaller central region with lower virial temperature than uniform one-zone model.

- Comparing with the rarefied filament model in Chapter 4, one-dimensional filament model predicts similar fragment mass. This explains that the discrepancy between the uniform filament model and one-dimensional filament model mainly comes from the runaway collapse which is partly induced by the pressure effect.
- As long as the external radiation is assumed to turn on when the filamentary clouds form, low density ( $n_0 \leq 10^2 \text{cm}^{-3}$ ) filamentary clouds with moderate line mass are expected to fragment into very massive clumps ( $\sim 10^5 M_\odot$ ) as a result of dissociation of molecular hydrogen by the effect of the external radiation. This result which is originally indicated in Chapter 3 is confirmed in this chapter using hydrodynamical calculations.

## 5.4 One unresolved question

It is found that the filamentary cloud with low initial density ( $n_0 < 10^{2.5} \text{cm}^{-3}$ ) and moderate line mass ( $f < 4.5$ ) fragments into more massive fragments under the external dissociating radiation than in the case without the external radiation. On the other hand, Omukai & Yoshii (2003) calculated the evolution of the filamentary cloud under the external dissociating radiation assuming free-fall. They assumed that fragmentation occurs at density 100 times higher than the loitering point where temperature is a local minimum in  $\rho - T$  plane owing to  $\text{H}_2$  cooling and concluded that the effect of the external dissociating radiation *decreases* fragment mass. This conclusion apparently disagrees with our results in Chapter 3-5. In order to clarify whether or not fragment mass increases when the filamentary cloud reaches the loitering point as a result of the dissociating radiation, in the next chapter, we consider wider parameter range for line mass including very large case (e.g.,  $f = 30$ ) which corresponds to the

case in Omukai & Yoshii (2003). We change line mass ( $f$ ) and the density when the external radiation turns on, and clarify dependence of fragment mass on this density and line mass.

# Chapter 6

## Criterion for increase of fragment mass

As pointed at the end of Chapter 5, our result apparently disagrees with Omukai & Yoshii (2003). In this chapter, we consider the possibility that the effect of the external radiation decreases fragment mass as indicated by Omukai & Yoshii (2003) using our model with pressure effect. Initial density of the filamentary cloud is assumed to be very low ( $n_0 = 0.1\text{cm}^{-3}$ ). As for the timing when the external radiation turns on, we consider various cases. The investigation in this chapter provides systematic study which includes the situation both of Bessho & Tsuribe (2012a) and Omukai & Yoshii (2003). The contents in this chapter are based on Bessho & Tsuribe (2012b).

### 6.1 Whether the filament reaches the loitering point

Suppose a filamentary cloud with  $n_0 = 0.1\text{cm}^{-3}$  and the external radiation turning on when density reaches  $n_{\text{UV}}$ . We consider the cases with  $n_{\text{UV}} = 0.1\text{cm}^{-3}$ ,  $1\text{cm}^{-3}$ , and  $10\text{cm}^{-3}$ . We also assume  $T_0 = 300\text{K}$  and  $f_{\text{H}_2} = 0$  at  $n = n_0$ . As for the evolution of the filamentary cloud, we solve one-dimensional hydrodynamics as in Chapter 5. Radiative transfer is treated by the same method as in Chapter 5 except that we use the new self-shielding function (Wolcott-Green et al. 2011; Appendix H). Chemical reactions are calculated with implicit integrator.

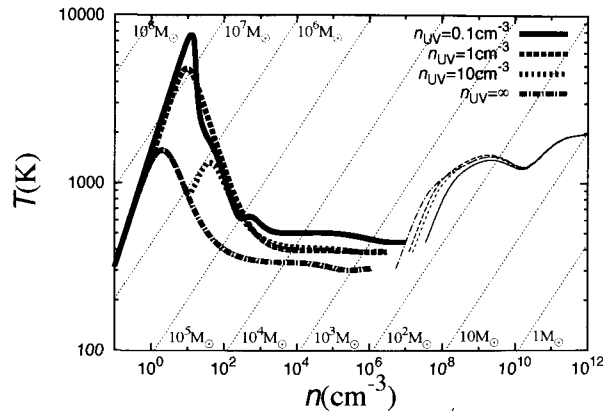


**Figure 6.1:** Thermal evolution of the filamentary cloud with  $f = 30$ ,  $n_0 = 0.1\text{cm}^{-3}$ ,  $J_{21} = 10$ , and various  $n_{\text{UV}}$  where the external radiation turns on ;  $n_{\text{UV}} = 0.1\text{cm}^{-3}$  (thick solid line)  $n_{\text{UV}} = 1\text{cm}^{-3}$  (thick long-dashed line),  $n_{\text{UV}} = 10\text{cm}^{-3}$  (thick short-dashed line),  $n_{\text{UV}} = \infty$  (thick dash-dotted line). Thin lines show the thermal evolution of fragments. Dotted lines indicate the constant Jeans masses. This figure is taken from Bessho & Tsuribe (2012b).

We calculate the evolution of the filamentary cloud with various values of  $f$ . In order for the filamentary cloud not to fragment during adiabatic phase in the case with  $J_{21} = 10$ , it is found that  $f$  is required to be larger than 30, 25, 10, and 5 for the case with  $n_{\text{UV}} = 0.1\text{cm}^{-3}$ ,  $1\text{cm}^{-3}$ ,  $10\text{cm}^{-3}$ , and  $\infty$ , respectively. Hence, we focus on the cases with  $f = 30, 25, 10$ , and 5 and investigate how massive fragments are.

First, we show the case with  $f = 30$  where the filamentary cloud reaches the loitering point for any  $n_{\text{UV}}$ . Figure 6.1 shows the thermal evolution of the filamentary cloud with  $f = 30$ ,  $n_0 = 0.1\text{cm}^{-3}$ ,  $J_{21} = 10$ , and various  $n_{\text{UV}}$ . Thick lines indicate thermal evolution from the initial state to the moment of fragmentation. Thin lines indicate thermal evolution of each clump after fragmentation (see §6.2). Fragment mass is seen from Jeans mass at the points that connect thick and thin lines of each kind. Fragment mass is smaller in the case with low  $n_{\text{UV}}$  (fragment mass are  $340M_{\odot}$ ,  $500M_{\odot}$ , and  $440M_{\odot}$  for  $n_{\text{UV}} = 0.1\text{cm}^{-3}$ ,  $1\text{cm}^{-3}$ , and  $10\text{cm}^{-3}$ , respectively) and largest ( $550M_{\odot}$ ) in the case with  $n_{\text{UV}} = \infty$ . From this result, it is found that

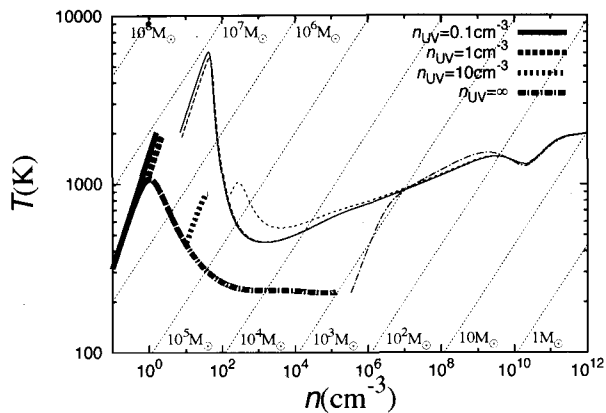


Figure 6.2: Same as figure 6.1, but  $f = 5$ . This figure is taken from Bessho & Tsuribe (2012b).

the effect of the external radiation decreases fragment mass. This result also indicates that all the filamentary clouds fragments at the density which is roughly 1000 times higher than the loitering point ( $n \sim 10^{3.5} \text{cm}^{-3}$ ). This indication is qualitatively consistent with Omukai & Yoshii (2003).

Next, we investigate the case with  $f = 5$  where the filamentary cloud fragments before it reaches the loitering point. Figure 6.2 shows the same figure as figure 6.1 except for the value of  $f$ . In figure 6.2, it is seen that the filamentary cloud except for the case with  $n_{\text{UV}} = \infty$  fragments into more massive clouds during adiabatic phase than in the case with  $n_{\text{UV}} = \infty$ . Fragment mass are  $4.6 \times 10^6 M_{\odot}$ ,  $3.8 \times 10^6 M_{\odot}$ , and  $2.9 \times 10^5 M_{\odot}$  for  $n_{\text{UV}} = 0.1 \text{cm}^{-3}$ ,  $1 \text{cm}^{-3}$ , and  $10 \text{cm}^{-3}$ , respectively. These fragment mass are larger than fragment mass in the case with  $n_{\text{UV}} = \infty$  ( $1000 M_{\odot}$ ). This feature agrees with our result of Chapter 5. Also in the cases with  $f = 25$  and  $10$ , it is found that the filamentary cloud fragments into more massive clouds than the case without the external radiation ( $n_{\text{UV}} = \infty$ ) when it does not reach the loitering point ( $n_{\text{UV}} \leq 0.1 \text{cm}^{-3}$  for  $f = 25$  and  $n_{\text{UV}} \leq 1 \text{cm}^{-3}$  for  $f = 10$ ). Whether or not the external radiation increases fragment mass is determined by the condition whether or not line mass is small enough for the filamentary cloud not to reach the loitering point.

Here, we discuss the physical reason for the fact that fragment mass decreases under the

external radiation : as Omukai & Yoshii (2003) indicated, sufficient amount of  $\text{H}_2$  forms and  $\text{H}_2$  cooling becomes effective at higher density under stronger radiation. After  $\text{H}_2$  cooling becomes effective, the evolution of the filamentary cloud is similar to the case without the external radiation. Hence, as shown in figure 6.1, the filamentary cloud fragments at the density which is 1000 times larger than the loitering point. Decrease of fragment mass results from higher density at the loitering point. This tendency is qualitatively the same as Omukai & Yoshii (2003) who assumed that the filamentary cloud fragments at the density which is 100 times larger than the loitering point.

## 6.2 Effect of sub-fragmentation

So far, it is found that the external radiation increases fragment mass when a filamentary cloud fragments before the loitering point. However, sub-fragmentation<sup>1</sup> may occur in each fragment. In such a case, mass of the final outcome may be as small as fragment mass in the case without the external radiation. To discuss mass of final outcome including the effect of sub-fragmentation, we consider the further evolution of each fragment.

We use one-zone model for each fragment. We assume that each fragment is spherical and has mass with  $M_{\text{frag}}$  (see Eq.5.7), chemical composition same as at the center of the filamentary cloud, and radius  $r_{0.1}$  where  $n(r_{0.1}) = 0.1n_c$ . As the infall velocity of each fragment, infall velocity at  $r_{0.1}$  is used. The density of fragment is estimated from the mass and radius as

$$\rho_{\text{frag}} = \frac{M_{\text{frag}}}{\frac{4\pi}{3}r_{0.1}^3}. \quad (6.1)$$

This density,  $\rho_{\text{frag}}$ , is different from the density of the filamentary cloud before fragmentation and is regarded as the one at the end of fragmentation. Temperature and fraction of each fragment are approximated by the value when the filamentary cloud fragments. According to

---

<sup>1</sup>”Sub-fragmentation” means that fragmentation occurs again in each clump which forms as a result of fragmentation of the filamentary cloud.

the result in §5.2.3, in the view point of dynamical evolution, we should consider the effect of pressure gradient force. Hence, we treat pressure effect explicitly using the virial equation for a uniform sphere. The virial equation is given by

$$\frac{dv}{dt} = \frac{10}{3} \frac{k_B T}{\mu m_H} \frac{1}{R} - \frac{GM}{R^2}, \quad (6.2)$$

where  $R$  is radius and  $M$  is mass of the cloud (see Appendix I). Radiative transfer is treated by the same method as in Omukai (2001) except that we use the new self-shielding function (Wolcott-Green et al. 2011; Appendix H) instead of  $f_{\text{sh}}$ . The same routine as in Chapter 2 is used for chemical reactions.

We show thermal evolution of each fragment by thin lines in figure 6.1 and 6.2. In the case in figure 6.1, each fragment hardly cools and sub-fragmentation may not occur. On the other hand, in the case in figure 6.2, each fragment cools owing to  $\text{H}_2$  cooling and reaches the loitering point. Jeans mass at the loitering point is  $2.6 \times 10^4 M_\odot$  for  $n_{\text{UV}} = 0.1 \text{cm}^{-3}$  and  $1 \text{cm}^{-3}$  and  $2.2 \times 10^4 M_\odot$  for  $n_{\text{UV}} = 10 \text{cm}^{-3}$ . In this thesis, these masses are regarded as mass of the final outcome. In figure 6.2, it is seen that these masses are larger than fragment mass in the case without the external radiation. Hence, even if sub-fragmentation occurs, mass of the final outcome is still larger than in the case without the external radiation. This tendency is also found in the other cases with  $f = 25$  and 10.

## 6.3 Summary

In this chapter, collapse and fragmentation of primordial filamentary cloud with lower density and larger line mass than previous chapters are investigated using one-dimensional hydrodynamical calculations with the effect of the external dissociating radiation. It is found that the filamentary cloud fragments into more massive clumps under the external dissociating radiation in the case where the filamentary cloud fragments during adiabatic phase after the external radiation turns on. On the other hand, when the filamentary cloud reaches the loitering point before fragmentation, the effect of the dissociating radiation decreases fragment

mass. The former corresponds to the conclusion in Chapter 3-5. The latter is consistent with Omukai & Yoshii (2003). Difference between above two cases originates from the value of line mass which reflects the contribution of pressure effect.

## 6.4 Discussion

### 6.4.1 Application to cosmological simulation

In the previous section, we focus on the filamentary cloud with large line mass. Here, we discuss possible value of  $f$  in the result of a cosmological three-dimensional calculations for density perturbations (Greif et al. 2008) shown in figure 6.3. In figure 6.3, the filamentary cloud with density  $n \sim 10^{-2}\text{cm}^{-3}$  and radius  $\sim 7\text{kpc}$  is seen at the upper right. Line mass of this filamentary cloud is estimated as  $\sim 7.8 \times 10^{18}\text{g/cm}$ . With approximating temperature to be 300K, the critical line mass is estimated to be  $l_{\text{crit}} \sim 3.5 \times 10^{17}\text{g/cm}$ . Hence,  $f = l/l_{\text{crit}}$  is found to be  $\sim 22$ . According to the result in §6.3, we can predict that fragment mass is expected to be larger if the external radiation turns on at the moment with  $n \leq 1\text{cm}^{-3}$ .

### 6.4.2 Thermal evolution of filament and sphere after the loitering point

As seen in figure 6.1 and 6.2, the thermal evolution of the filamentary cloud (thick lines in figure 6.1) and spherical cloud (thin lines in figure 6.2) after they reach the loitering point is different. The thermal evolution of the filamentary cloud is approximately isothermal, and temperature of spherical cloud increases. This difference is explained as follows : in the case of the filamentary cloud, since the central region is approximately in dynamical equilibrium (§5.2.3), we have

$$\begin{aligned} \frac{1}{\rho} \frac{P}{r} &\sim \frac{Gl}{r} \\ T &\sim \mu m_{\text{H}} Gl \propto \text{const.} \end{aligned} \tag{6.3}$$

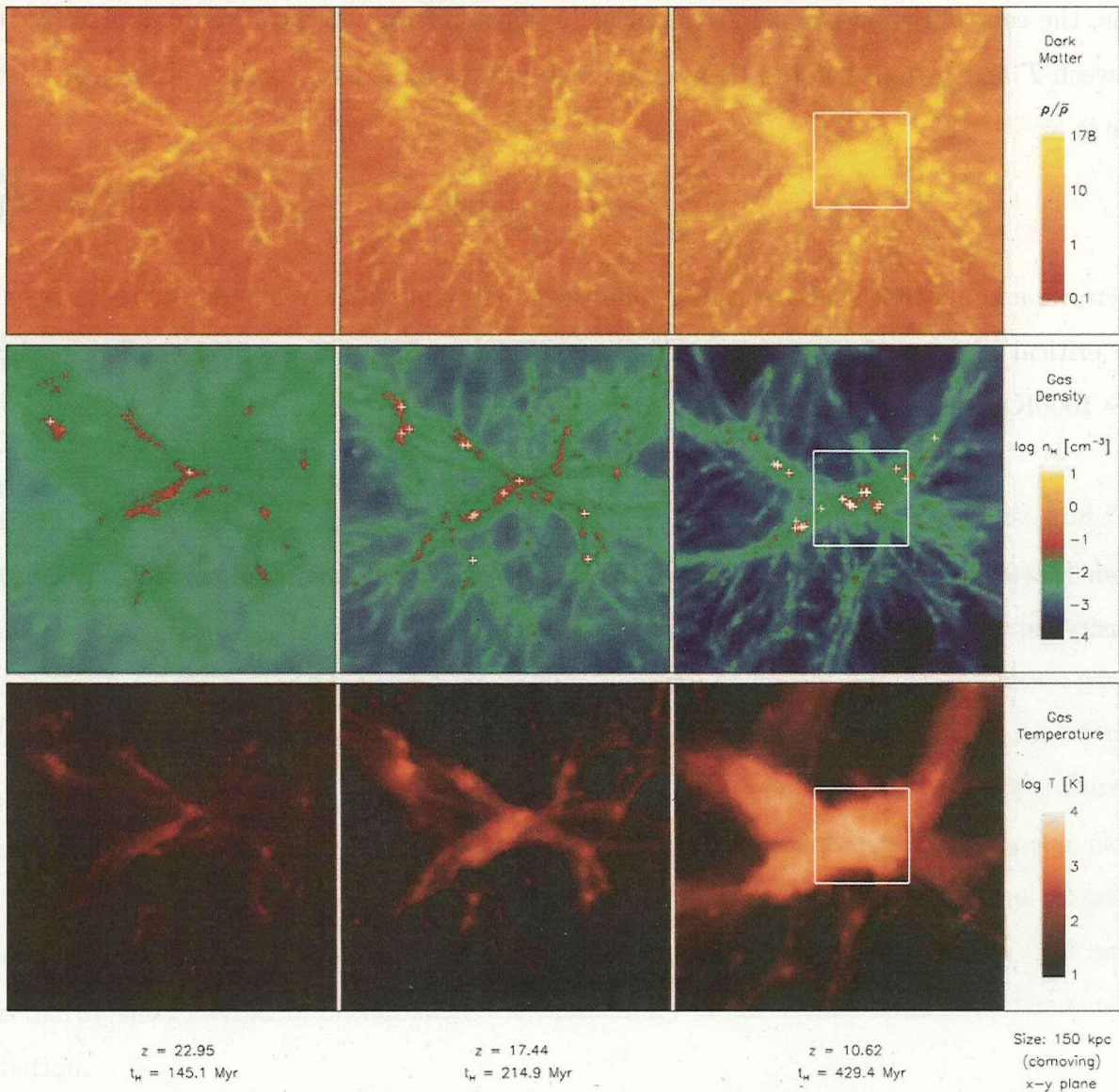


**Figure 6.3:** Dark matter overdensity, hydrogen number density, and temperature averaged along the line of sight within the central  $\sim 150$  kpc (comoving) at  $z \sim 23$ ,  $z \sim 17.5$ , and  $z \sim 10.5$  in the three-dimensional cosmological calculation by Greif et al. (2008). White crosses denote Pop III.1 star formation sites in miniharos. This figure is taken from Greif et al. (2008).

On the other hand, in the case of spherical cloud, since dynamical time is shorter than cooling time, the central region is not in dynamical equilibrium state. Hence, we investigate relation between  $T$  and  $n$  from balance between adiabatic heating and  $H_2$  cooling. Adiabatic heating rate is

$$-P \frac{d}{dt} \frac{1}{\rho} \sim P \frac{1}{t_{ff} \rho} \propto T \rho^{1/2} \quad (6.4)$$

where we assume that spherical cloud collapses in free-fall state. When density is larger than the critical density of  $H_2$ , we have  $\Lambda_{H_2} \propto n T^\alpha$  ( $\alpha \sim 3.8$  at  $T \sim 300K$  and  $\alpha \sim 4.8$  at  $T \sim 1000K$ ). Thus, we have

$$\frac{\Lambda_{H_2}}{\rho} \propto \frac{n T^\alpha}{n} \propto T^\alpha. \quad (6.5)$$

From Eq.(6.7) and Eq.(6.8), we have  $T \propto \rho^{1/2(\alpha-1)}$ . In summary, temperature depends on density as,

$$T \propto \begin{cases} \rho^{1/2(\alpha-1)} & \text{sphere} \\ \text{const.} & \text{filament.} \end{cases} \quad (6.6)$$

# Chapter 7

## Conclusions

In this thesis, as one of paths to primordial star formation, we investigate collapse and fragmentation of primordial filamentary cloud under the external dissociating radiation with two types of one-zone models and one-dimensional hydrodynamical model. We consider the redshift  $z \sim 10$  and the region where photoionization does not occur but photodissociation occurs. In all the models, owing to photodissociation, the filamentary cloud with low initial density ( $n_0 \leq 10^2 \text{cm}^{-3}$ ) and moderate line mass ( $f \sim 2$ ) loses main coolant. Hence, temperature increases adiabatically. As a result, such a filamentary cloud fragments into very massive clouds ( $\sim 10^5 M_\odot$ ). Thus, formation of such a very mass fragments can be regarded as a robust result. The evolution of the filamentary cloud with high initial density ( $n_0 > 10^2 \text{cm}^{-3}$ ) is hardly affected by the external radiation since the filamentary cloud shields itself from the external radiation.

We investigate the case with large line mass ( $f = 30, 25, 10, \text{ and } 5$ ) in Chapter 6. It is found that in the case where the filamentary cloud does not fragment during adiabatic phase, fragment mass becomes smaller under the external radiation. This result is consistent with Omukai & Yoshii (2003). In the case where the filamentary cloud fragments during adiabatic phase, fragment mass becomes larger under the external radiation. In such a case, if sub-fragmentation occurs in each fragment, mass of the final outcome is larger than in the

case without the external radiation. Our investigation includes the situations of Nakamura & Umemura (2002) and Omukai & Yoshii (2003) as a part. Thus, it gives us understanding of more general case than previous studies.

For further collapse, spherical clouds are possible to be the filamentary cloud again or may become disk-like cloud if it rotates. Although we discuss a possible sub-fragmentation at the loitering point for each clumps in §6.2, the final fate of the cloud is still open question. Furthermore, if the filamentary cloud with large line mass is not axisymmetric, it may become sheet-like cloud. Such a cloud may collapse and fragment into many filamentary clouds.

In this thesis, the external dissociating radiation is assumed to be uniform, and the intensity does not depend on time. Moreover, we do not consider photoionization. For simplicity, the model and numerical calculations in this thesis are one-dimensional and one-zone model. In order to discuss fragmentation, we assume the condition for fragmentation (Chapter 2). In order to treat fragmentation completely, we need three-dimensional calculations. As for three-dimensional simulation with the external radiation, Susa (2007) investigated collapse of spherical cloud under the single light source. However, further investigations with three-dimensional simulation which statistically investigate fragment mass of the filamentary cloud under the external radiation will be desirable. Despite simplicity, one-dimensional hydrodynamical calculations in this paper are useful in the view point of extracting physical processes which are important in formation of the astronomical objects. These one-dimensional calculations and the realistic three-dimensional calculations may be complementary.

# Appendix A

## On the formation and fragmentation of the filamentary cloud

In this appendix, we summarize formation and fragmentation of the filamentary cloud. We introduce the isothermal equilibrium state for the filamentary cloud. In cosmological simulations, the filamentary structure form from density perturbation (Abel et al. 1998; Bromm et al. 1999; Greif et al. 2008). The filamentary cloud is possible to forms by fragmentation of sheet-like cloud (Miyama et al. 1987). Such filamentary cloud tends to fragment into spherical clouds (Nagasawa 1987; Nakamura et al. 1993). Finally, we investigate the dispersion relation for the filamentary cloud.

### A.1 The density profile and line mass of the isothermal equilibrium filamentary cloud

In this section, we derive the density profile and line mass of the isothermal equilibrium filamentary cloud according to Ostriker (1964).

Equation of state for ideal gas

$$P = \frac{k_B T}{\mu m_H} \rho \equiv K \rho \quad (\text{A.1})$$

is assumed. At dynamical equilibrium, the following equation is satisfied :

$$\nabla \Psi = \nabla K \ln \rho, \quad (\text{A.2})$$

where  $\Psi$  is gravitational potential. By differentiating Eq.(A.2) and using Poisson equation  $\nabla^2 \Psi = -4\pi G \rho$ , we have

$$\nabla^2 \Psi = \nabla^2 K \ln \rho = -4\pi G \rho. \quad (\text{A.3})$$

By defining  $\vec{\xi}$ ,  $\psi$ , and  $V$  as follows :

$$\vec{r} \equiv \sqrt{\frac{K}{4\pi G \rho_0}} \vec{\xi}, \quad (\text{A.4})$$

$$\rho \equiv \rho_0 e^{-\psi}, \quad (\text{A.5})$$

$$\Psi \equiv KV, \quad (\text{A.6})$$

we can write Poisson equation as follows :

$$\nabla^2 \left( \frac{K}{4\pi G \rho_0} \ln \rho \right) = -e^{-\psi} \quad (\text{A.7})$$

$$\nabla'^2 \psi = e^{-\psi} \quad (\text{A.8})$$

$$\psi'' + \frac{1}{\xi} \psi' = e^{-\psi}, \quad (\text{A.9})$$

where  $'$  denotes the partial derivative with respect to  $\xi$ . This equation is Lane-Emden equation for the isothermal equilibrium of filamentary cloud. The boundary conditions are

$$\psi'(0) = \psi(0) = 0. \quad (\text{A.10})$$

We define  $z$  and  $t$  as

$$z \equiv -\psi + 2 \ln \xi \quad (\text{A.11})$$

$$t \equiv \sqrt{2} \ln \xi. \quad (\text{A.12})$$

Then we can express Lane-Emden equation as

$$2\frac{d^2z}{dt^2} + e^z = 0. \quad (\text{A.13})$$

We multiply both hands of Eq.(A.13) by  $dz/dt$ , integrate with respect to  $t$ , and have

$$\left(\frac{dz}{dt}\right)^2 + e^z + C_1 = 0 \quad (\text{A.14})$$

$$\frac{dz}{dt} = \pm\sqrt{C_1 - e^z} \quad (\text{A.15})$$

where  $C_1$  is a constant of integration. From boundary conditions,  $C_1 = 2$ . By defining  $y$  as  $y \equiv e^z$  and  $y$ -integrating Eq.(A.15), we have

$$\int \frac{dy}{y\sqrt{2-y}} = \pm \int dt \quad (\text{A.16})$$

$$\frac{1}{2} \ln \left| \frac{\sqrt{2} - \sqrt{2-y}}{\sqrt{2} + \sqrt{2-y}} \right| = \pm(t + \sqrt{2} \ln C_2). \quad (\text{A.17})$$

By using  $\psi$  and  $\xi$ , we can write Eq.(A.17) as

$$e^{-\psi} = \frac{8}{\xi^2} \frac{(\xi C_2)^{\pm 2}}{\{(\xi C_2)^{\pm 2} + 1\}^2}. \quad (\text{A.18})$$

In order for central region to have higher density than outer region, we take plus of plus-minus. From boundary conditions,  $C_2 = 1/\sqrt{8}$ . Hence we have

$$\psi = 2 \ln \left( 1 + \frac{\xi^2}{8} \right) \quad (\text{A.19})$$

and

$$\rho = \rho_0 \left( 1 + \frac{1}{8} \xi^2 \right)^{-2} = \rho_0 \left( 1 + \frac{\pi G \mu m_{\text{H}} \rho_0}{2k_B T} r^2 \right)^{-2}. \quad (\text{A.20})$$

This is the density profile of the isothermal equilibrium filamentary cloud. Line mass of such a cloud is,

$$l(\xi) = 2\pi \frac{K}{4\pi G \rho_0} \int_0^\xi \xi' \left( 1 + \frac{1}{8} \xi'^2 \right)^{-2} d\xi' = \frac{2k_B T}{G \mu m_{\text{H}}} \frac{1}{1 + 8/\xi^2}. \quad (\text{A.21})$$

As  $\xi$  approaches infinity, the critical line mass is,

$$l_c = \frac{2k_B T}{G \mu m_{\text{H}}}. \quad (\text{A.22})$$

## A.2 Formation of the filamentary cloud

### A.2.1 Density perturbation

Abel et al. (1998) found with three-dimensional simulation that the filamentary structure is formed as a result of dynamical evolution of density perturbations in the early universe. In Figure A.1, dynamical evolution is shown by contours of dark matter density and baryon density. It is seen that dark matter forms the filamentary structure at  $z = 35$ . (Baryon) gas is pulled by dark matter gravity. During collapse,  $H_2$  forms in gas, and temperature decreases. Since gas pressure decreases, gas evolves mainly by gravity and forms the filamentary structure.

### A.2.2 Sheet-like cloud

Miyama et al. (1987a) derived the dispersion relation for the isothermal sheet-like cloud into the filamentary clouds. By their work, it was found that the sheet-like cloud tends to fragment into filamentary clouds.

In this subsection, we summarize this dispersion relation according to Miyama et al. (1987a). The density profile of sheet-like cloud in dynamical equilibrium is given by

$$\rho(z) = \frac{\rho_{00}}{\cosh^2(z/z_0)}, \quad (\text{A.23})$$

where

$$\rho_{00} = \rho_0(0) \quad (\text{A.24})$$

$$z_0 = \frac{c_s}{\sqrt{2\pi G\rho_{00}}}, \quad (\text{A.25})$$

$G$  is gravitational constant,  $c_s$  is sound speed. Density  $\rho$ , velocity  $\vec{v}$ , and gravitational potential  $\Psi$  are perturbed as follows :

$$\rho = \rho_0 + \rho_1, \quad (\text{A.26})$$

$$\vec{v} = \vec{v}_1, \quad (\text{A.27})$$

$$\Psi = \Psi_0 + \Psi_1, \quad (\text{A.28})$$

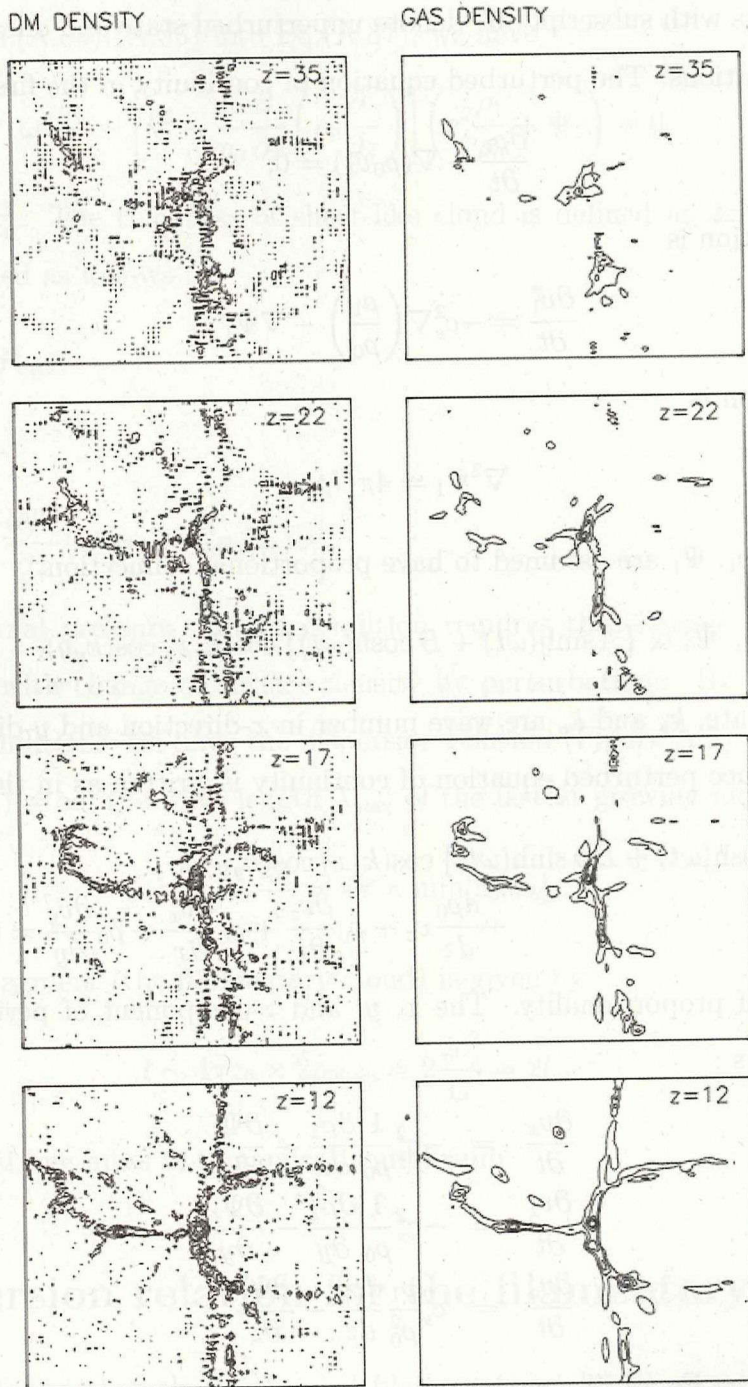


**Figure A.1:** The contours showing evolution of dark matter density and baryon density at  $z = 35$ , 22, 17, and 12. Five levels (0.5, 1, 1.5, 2, and 2.5) are displayed for  $\log \rho/\bar{\rho}$ , in which  $\bar{\rho}$  is background density. This figure is taken from Abel et al. (1998).

where the quantities with subscript "0" denote unperturbed state and ones with subscript "1" denote the perturbations. The perturbed equation of continuity in the first order is given by

$$\frac{\partial \rho_1}{\partial t} + \nabla(\rho_0 \vec{v}_1) = 0, \quad (\text{A.29})$$

the equation of motion is

$$\frac{\partial \vec{v}_1}{\partial t} = -c_s^2 \nabla \left( \frac{\rho_1}{\rho_0} \right) - \nabla \Psi_1 \quad (\text{A.30})$$

and Poisson equation is

$$\nabla^2 \Psi_1 = 4\pi G \rho_1. \quad (\text{A.31})$$

The perturbations  $\rho_1$ ,  $\Psi_1$  are assumed to have proportional connection,

$$\rho_1, \Psi_1 \propto \{A \sinh(\omega t) + B \cosh(\omega t)\} \cos(k_x x) \cos(k_y y), \quad (\text{A.32})$$

where  $\omega$  is growth rate,  $k_x$  and  $k_y$  are wave number in  $x$ -direction and  $y$ -direction, and  $A$  and  $B$  are constant. Hence perturbed equation of continuity is written as in the form

$$\begin{aligned} & \{A\omega \cosh(\omega t) + B\omega \sinh(\omega t)\} \cos(k_x x) \cos(k_y y) \rho_1' \\ & + \frac{d\rho_0}{dz} v_z + \rho_0 \frac{\partial v_z}{\partial z} + \rho_0 \frac{\partial v_x}{\partial x} + \rho_0 \frac{\partial v_y}{\partial y} = 0, \end{aligned} \quad (\text{A.33})$$

where  $\rho_1'$  is factor of proportionality. The  $x$ ,  $y$ , and  $z$ -component of perturbed equation of motion are as follows :

$$\frac{\partial v_x}{\partial t} = -c_s^2 \frac{1}{\rho_0} \frac{\partial \rho_1}{\partial x} - \frac{\partial \Psi_1}{\partial x}, \quad (\text{A.34})$$

$$\frac{\partial v_z}{\partial t} = -c_s^2 \frac{1}{\rho_0} \frac{\partial \rho_1}{\partial y} - \frac{\partial \Psi_1}{\partial y}, \quad (\text{A.35})$$

$$\frac{\partial v_z}{\partial t} = c_s^2 \frac{\rho_1}{\rho_0^2} \frac{d\rho_0}{dz} - \frac{\partial \Psi_1}{\partial z}. \quad (\text{A.36})$$

By time-differentiating Eq.(A.33), we have

$$\begin{aligned} & \{A\omega^2 \sinh(\omega t) + B\omega^2 \cosh(\omega t)\} \cos(k_x x) \cos(k_y y) \rho_1' \\ & + \frac{d\rho_0}{dz} \frac{\partial v_z}{\partial t} + \rho_0 \frac{\partial}{\partial z} \frac{\partial v_z}{\partial t} + \rho_0 \frac{\partial}{\partial x} \frac{\partial v_x}{\partial t} + \rho_0 \frac{\partial}{\partial y} \frac{\partial v_y}{\partial t} = 0. \end{aligned} \quad (\text{A.37})$$

By substituting Eqs.(A.34)-(A.36) into Eq.(A.37), we have

$$\omega^2 \frac{\rho_1}{\rho_0} + \left[ k^2 - \frac{1}{\rho_0} \frac{\partial}{\partial z} \left( \rho_0 \frac{\partial}{\partial z} \right) \right] \left( c_s^2 \frac{\rho_1}{\rho_0} + \Psi_1 \right) = 0, \quad (\text{A.38})$$

where  $k^2 \equiv k_x^2 + k_y^2$ . The thickness of sheet-like cloud is defined as  $2z_b$  and the boundary conditions is assumed as follows :

1.  $P(z_b + z_1) = P_{\text{ext}}$ ,
2.  $\frac{dz_1}{dt} = v_{1,z}(z_b)$ ,
3.  $-|k|\Psi_1(z_b) - \frac{\partial \Psi_1}{\partial z}(z_b) = 4\pi G \rho_0(z_b) z_1$ ,

where  $P_{\text{ext}}$  is external pressure. Third condition requires that change of the gravitational potential balances with change of surface density by perturbations. By using Eq(A.38) and above boundary conditions, we have the dispersion relation (Figure A.2).

When  $\rho_{00}/\rho_0(z_b) = \infty$ , the wave length  $\lambda_{\text{max}}$  of the fastest growing mode is

$$\lambda_{\text{max}} = \frac{2\pi}{k} = 4\pi \times \min[z_0, z_b]. \quad (\text{A.39})$$

Line mass of the fragment (the filamentary cloud) is given by

$$l \sim 4\pi z_0 \times 2\rho_{00} z_0 = 2 \frac{2c_s^2}{G} = 2l_c, \quad (\text{A.40})$$

where  $l_{\text{crit}}$  is critical line mass in dynamical equilibrium.

### A.3 Dispersion relation for the filamentary cloud

Nagasawa (1987) found that the isothermal filamentary cloud is unstable for axisymmetric perturbations of wave length  $\lambda > \lambda_{\text{crit}} = 11.2H$  where  $H \equiv c_s/\sqrt{4\pi G\rho_c}$  and  $\rho_c$  is the density at the center. In this appendix, we summarize the dispersion relation and the fragmentation timescale according to Nagasawa (1987).

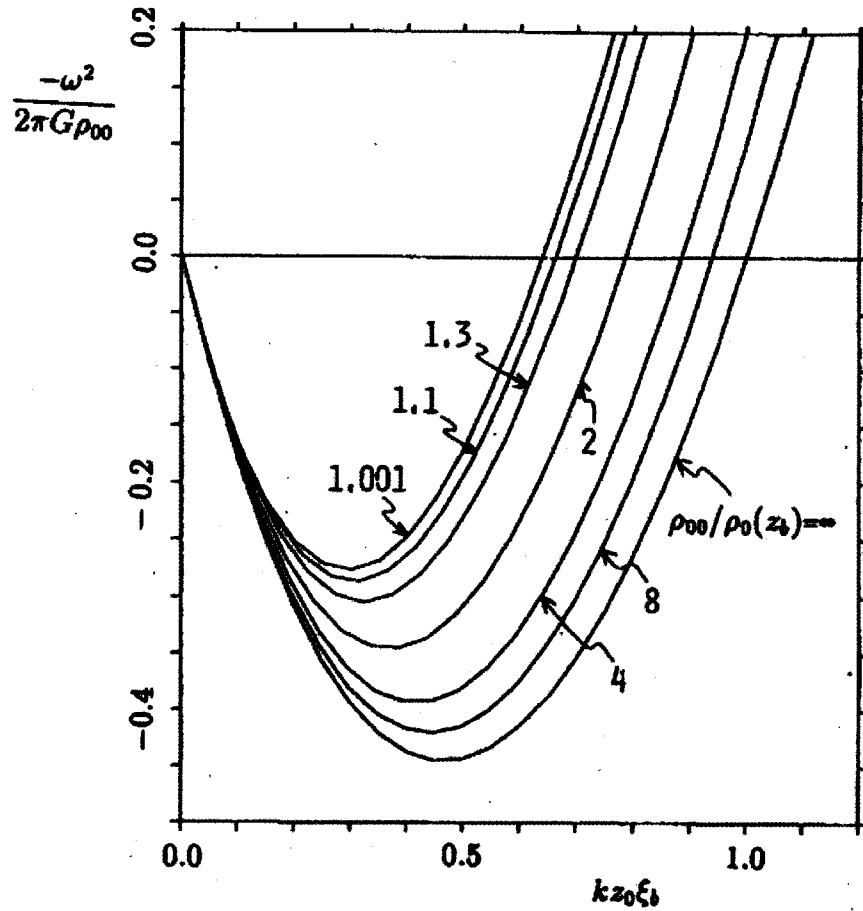


**Figure A.2:** The dispersion relation of fragmentation of the isothermal sheet-like cloud. This figure is taken from Miyama et al. (1987a).

We denote the equilibrium value with the subscript "0" and the first-order perturbations with "1". Then, perturbed equation of continuity, perturbed equation of motion, and perturbed Poisson equation in the first order are as follows :

$$\frac{\partial \rho_1}{\partial t} + \nabla(\rho_0 \vec{v}_1) = 0, \quad (\text{A.41})$$

$$\frac{\partial \vec{v}_1}{\partial t} = -c_s^2 \nabla \left( \frac{\rho_1}{\rho_0} \right) - \nabla \Psi_1, \quad (\text{A.42})$$

$$\nabla^2 \Psi_1 = 4\pi G \rho_1. \quad (\text{A.43})$$

The perturbations are assumed to have a common form,

$$q_1(r, \phi, z; t) = q_1(r) \exp(ikz + im\phi - i\omega t), \quad (\text{A.44})$$

where  $k$  is the wave number in  $z$ -direction,  $m = 0$  represents axisymmetric mode, and  $m = 1$  represents non-axisymmetric mode. By substituting Eq.(A.44) into Eq.(A.42) and differentiating Eq.(A.42) with respect to  $t$ , we have

$$\omega^2 v_r = -i\omega \frac{d}{dr} \chi_1, \quad (\text{A.45})$$

$$\omega^2 v_\phi = \omega \frac{m}{r} \chi_1, \quad (\text{A.46})$$

$$\omega v_z = k \chi_1 \quad (\text{A.47})$$

where

$$\chi_1 \equiv c_s^2 \frac{\rho_1}{\rho_0} + \Psi_1. \quad (\text{A.48})$$

By substituting Eq.(A.44) into Eqs.(A.41) and (A.43), we have

$$-i\omega \frac{\rho_1}{\rho_0} + \frac{1}{\rho_0} \left( \frac{d}{dr} + \frac{1}{r} \right) (\rho_0 v_r) + i \frac{m}{r} v_\phi + ik v_z = 0, \quad (\text{A.49})$$

$$\left( \frac{d^2}{dr^2} + \frac{1}{r} \frac{d}{dr} - k^2 - \frac{m^2}{r^2} \right) \Psi_1 = 4\pi G \rho_1. \quad (\text{A.50})$$

Nagasawa (1987) solved Eqs.(A.45)-(A.50) as an eigenvalue problem for  $\omega$  for given set of  $(k, m)$  with boundary conditions by numerical method. Boundary conditions are as follows :

1.  $v_r, v_\phi, \frac{dv_z}{dr}, \frac{d\chi_1}{dr}$  and  $\frac{d\Psi_1}{dr} \rightarrow 0$  for  $r \rightarrow 0$ ,
2.  $\frac{dv_r}{dr}, \frac{dv_\phi}{dr}, \frac{dv_z}{dr}, \frac{d\chi_1}{dr}$  and  $\frac{d\Psi_1}{dr} \rightarrow 0$  for  $r \rightarrow \infty$ .

In Figure A.3, we show the dispersion relation in the case of  $m = 0, 1$ . Axisymmetric mode is able to grow. However,  $m = 1$  mode (non-axisymmetric mode) never grows. In the case of  $m = 0$ , the most unstable wave number is

$$k_m = 0.284 \frac{\sqrt{4\pi G \rho_c}}{c_s}, \quad (\text{A.51})$$

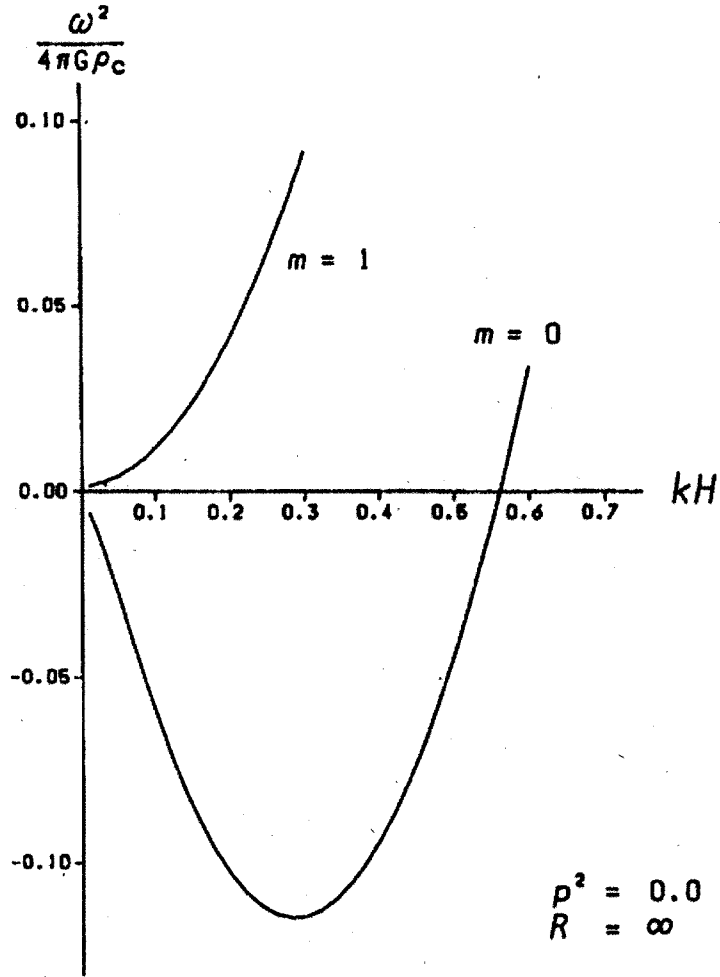


**Figure A.3:** Dispersion relation of the isothermal filamentary cloud in the case of  $m = 0, 1$ . This figure is taken from Nagasawa (1987)..

where  $\rho_c$  is the density at the center. The highest growth rate is,

$$|\omega_m| = 0.339\sqrt{4\pi G\rho_c}. \quad (\text{A.52})$$

This value determines fragmentation timescale.

# Appendix B

## Line cooling and Continuum processes

In this appendix, we summarize cooling rate of lines according to Palla et al. (1983), Omukai(2001), and Appendix C.

### B.1 H lines

Hydrogen atom H is modeled as a five-level system. According Eq.(C.10), in the case of the uniform model, the radiative cooling rate due to H lines per unit volume is given by

$$\Lambda_{\text{H lines}} = \sum_{u,l} h\nu_{ul} A_{ul} n_u(\text{H}) \frac{1}{k_\nu} 2\Delta\nu_D \frac{2}{R} f(2k_{ul}R) \quad (\text{B.1})$$

where  $n_u(\text{H})$  is population density of H in the upper level  $u$ ,  $A_{ul}$  is Einstein  $A$ -coefficient,  $h\nu_{ul}$  is energy difference between the upper level  $u$  and the lower level  $l$ ,  $f$  is function defined in Eq.(C.8), and  $k_{ul}$  is opacity between  $u$  and  $l$ .

Relative populations of each energy level are obtained with the detailed balance between levels,

$$n_i(\text{H}) \sum_{j \neq i}^n R_{ij} = \sum_{j \neq i}^n n_j(\text{H}) R_{ji}. \quad (\text{B.2})$$

The relation rate  $R_{ij}$  from level  $i$  to level  $j$  is given by

$$R_{ij} = \begin{cases} A_{ij}\beta_{\text{esc},ij}(1 + Q_{ij}) + C_{ij} & i > j \\ (g_j/g_i)A_{ji}\beta_{\text{esc},ij}Q_{ji} + C_{ij} & i < j \end{cases} \quad (\text{B.3})$$

where  $g_i$  is statistical weight of level  $i$  of H,  $C_{ij}$  is collisional transition rate, and

$$Q_{ij} = \frac{c^2}{2h\nu_{ij}^3} J_{\text{cont}}(\nu_{ij}). \quad (\text{B.4})$$

The relative population within the first excited states (i.e.,  $2p$  and  $2s$  states) is obtained from statistical equilibrium (Spitzer & Greenstein 1951)

$$\frac{n_{2s}}{n_{2p}} = \frac{g_{2s}}{g_{2p}} \left( \frac{C_{2s2p}}{C_{2s2p} + A_{2s1s}} \right), \quad (\text{B.5})$$

where  $g_{2s} = 2$ ,  $g_{2p} = 6$ ,  $A_{2s1s} = 8.23\text{s}^{-1}$ , and

$$C_{2s2p} = 6.21 \times 10^{-4} T^{-1/2} [\ln(5.7T) + 0.78] n(e) \text{s}^{-1}. \quad (\text{B.6})$$

Using  $n_{2p}$  obtained above, we have

$$A_{21} = \frac{n_{2p}}{n_2} A_{2p1s}, \quad (\text{B.7})$$

where  $A_{2p1s} = 6.27 \times 10^8 \text{s}^{-1}$ . We assume local thermal equilibrium (LTE) within levels of the same principal quantum number for  $n \geq 3$ . We average  $A_{ij}$  over angular quantum numbers. Then,  $A_{31} = 5.575 \times 10^7$ ,  $A_{41} = 1.278 \times 10^7$ ,  $A_{51} = 4.125 \times 10^6$ ,  $A_{32} = 4.410 \times 10^7$ ,  $A_{42} = 8.419 \times 10^6$ ,  $A_{52} = 2.530 \times 10^6$ ,  $A_{43} = 8.986 \times 10^6$ ,  $A_{53} = 2.201 \times 10^6$ , and  $A_{54} = 2.699 \times 10^6$  (Janev et al. 1987).

The collisional de-excitation rate originates in collisions with  $e^-$  and H itself,

$$C_{ul} = \gamma_{ul}(e)n(e) + \gamma_{ul}(\text{H})n(\text{H}), \quad (\text{B.8})$$

where  $\gamma_{ul}$  is collisional de-excitation rate coefficient, which is given by

$$\gamma_{ul}(e) = 10^{-8} \left( \frac{l^2}{u^2 - l^2} \right)^{3/2} \frac{l^4}{u^2} \alpha_{lu} \frac{\sqrt{\beta(\beta + 1)}}{\beta + \xi_{lu}}, \quad (\text{B.9})$$

(Sobelman et al. 1981), where  $\alpha_{12} = 24$ ,  $\alpha_{13} = 22$ ,  $\alpha_{14} = 22$ ,  $\alpha_{15} = 21$ ,  $\alpha_{23} = 67$ ,  $\alpha_{24} = 58$ ,  $\alpha_{25} = 56$ ,  $\alpha_{34} = 124$ ,  $\alpha_{35} = 101$ ,  $\alpha_{45} = 185$ ,  $\xi_{12} = 0.28$ ,  $\xi_{13} = 0.37$ ,  $\xi_{14} = 0.39$ ,  $\xi_{15} = 0.41$ ,  $\xi_{23} = 0.30$ ,  $\xi_{24} = 0.45$ ,  $\xi_{25} = 0.52$ ,  $\xi_{34} = 0.26$ ,  $\xi_{35} = 0.42$ ,  $\xi_{45} = 0.21$ , and  $\beta = h(\nu_l - \nu_u)/k_B T$ . For collision with H (Drawin 1969),

$$\gamma_{ul}(\text{H}) = 7.86 \times 10^{-15} \left(\frac{l}{u}\right)^2 \left(\frac{1}{l^2} - \frac{1}{u^2}\right)^{-2} f_{lu} T^{1/2} \frac{1 + 1.27 \times 10^{-5} (1/l^2 - 1/u^2)^{-1} T}{1 + 4.76 \times 10^{-17} (1/l^2 - 1/u^2)^{-2} T^2}, \quad (\text{B.10})$$

where  $f_{12} = 0.4162$ ,  $f_{13} = 7.910 \times 10^{-2}$ ,  $f_{14} = 2.899 \times 10^{-2}$ ,  $f_{15} = 1.394 \times 10^{-2}$ ,  $f_{23} = 0.6407$ ,  $f_{24} = 0.1193$ ,  $f_{25} = 4.467 \times 10^{-2}$ ,  $f_{34} = 0.8421$ ,  $f_{35} = 0.1506$ , and  $f_{45} = 1.038$ . The collisional excitation rate is obtained from the detailed balance,

$$C_{lu} = C_{ul} \frac{g_u}{g_l} e^{-h\nu_{ul}/k_B T}. \quad (\text{B.11})$$

The optical depth is given by

$$\tau_{ul} = \frac{A_{ul} c^3}{8\pi \nu_{ul}^3} \left[ \frac{g_u}{g_l} n_l(\text{H}) - n_u(\text{H}) \right] \frac{l_{\text{sh}}}{v_D}, \quad (\text{B.12})$$

where

$$v_D = \sqrt{\frac{2k_B T}{m_{\text{H}}}} \quad (\text{B.13})$$

and

$$l_{\text{sh}} = \min \left[ R, \frac{v_D}{dv/dr} \right] \quad (\text{B.14})$$

is shielding length, which is included to take into account the effect of velocity gradient<sup>1</sup>.

## B.2 H<sub>2</sub> lines

The radiative cooling rate  $\Lambda_{\text{H}_2 \text{ lines}}$  due to H<sub>2</sub> can be represented by equation similar to Eq.(B.1). We compute the population of vibrational levels by the way similar to the way in the previous

<sup>1</sup>When the velocity changes by more than  $v_D$ , line photon is not absorbed because of Doppler shift.

section. We use collisional rate coefficients of Hollenbach & McKee (1989) and spontaneous radiative decay rate of Turner et al. (1977). The effect of the external radiation is also included. After we determined the population of each vibrational levels, we compute rovibrational population  $n_j^v$  of  $\text{H}_2$  by using following relation (Palla et al. 1983):

$$n_{j+2}^v = n_j^v \frac{2j+5}{2j+1} \frac{C_{j+2 \rightarrow j}^v}{C_{j+2 \rightarrow j}^v + A_{j+2 \rightarrow j}^v} \exp\left(-\frac{h(\nu_{j+2}^v - \nu_j^v)}{k_B T}\right), \quad (\text{B.15})$$

where  $h\nu_j^v$  is level energy,  $C_{j+2 \rightarrow j}^v$  is downward collisional transition rate (Hollenbach & McKee 1989), and  $A_{j+2 \rightarrow j}^v$  is downward radiative transition rate (Turner et al. 1977). We take into account the first three vibrational states ( $v = 0 - 2$ ) with rotational levels up to  $J = 20$  in each vibrational states. We assume the ortho to para ratio of  $\text{H}_2$  to be the equilibrium value 3 : 1. We determine the rovibrational energies  $h\nu_j^v$  according to Borysow et al. (1989).

### B.3 HD lines

The radiative cooling rate  $\Lambda_{\text{HD lines}}$  due to HD can be represented by equation similar to Eq.(B.1). We model HD as a ten-level system. The downward collisional and radiative transition rate is taken from Flower et al. (2000) and Abgral et al. (1982). The population of each level is determined by the way same as in B.1.

### B.4 Continuum processes

We consider eight absorption processes and two scattering processes according to Omukai (2001) and four absorption processes associated with D (see Table B.1). According to Appendix C, we can write the cooling rate  $\Lambda_{\text{conti}}$  with emissivity  $\eta_\nu = \sum_{a1-a12} \eta_{\nu,ai}$  and opacity  $\kappa_\nu = \sum_{a1-a12,s1,s2} \eta_{\kappa,ai,si}$  :

$$\Lambda_{\text{conti}} = \frac{\eta_\nu}{\kappa_\nu} 2\Delta\nu_D \frac{2}{R} f(2k_\nu R). \quad (\text{B.16})$$

Number	Name	Process	Cross Section (cm <sup>-2</sup> )	Reference
a1	H bound-free	$H(n) + \gamma \rightarrow H^+ + e$	$7.909 \times 10^{-18} n(\nu/\nu_n)^{-3}; h\nu_n = 13.598\text{eV}/n^2$	1
a2	He bound-free	$He + \gamma \rightarrow He^+ + e$	$7.83 \times 10^{-18} [1.66(\nu/\nu_T)^{-2.05} - 0.66(\nu/\nu_T)^{-3.05}]; h\nu_T = 24.586\text{eV}$	2
a3	H <sup>-</sup> bound-free	$H^- + \gamma \rightarrow H + e$	$10^{-18} \lambda^3 (1/\lambda - 1/\lambda_0)^{3/2} f(\lambda), \lambda_0 = 1.6419\mu\text{m}, f(\lambda)$ from Eq.(5) of reference	3
a4	H <sub>2</sub> <sup>+</sup> bound-free	$H_2^+ + \gamma \rightarrow H + H^+$	see table2 of reference	4
a5	H <sup>-</sup> free-free	$H + e + \gamma \rightarrow H + e$	$k_\lambda^{\text{ff}}(T) k_B T n_e; k_\lambda^{\text{ff}}$ from Eq.(6) of reference	3
a6	H free-free	$H^+ + e + \gamma \rightarrow H^+ + e$	$3.692 \times 10^8 g_{\text{ff}}(\nu, T) \nu^{-3} T^{-1/2} n_e; \text{we take } g_{\text{ff}}(\nu, T) = 1$	
a7	H <sub>2</sub> -H <sub>2</sub> CIA	$H_2(v, J) + H_2 + \gamma \rightarrow H_2(v', J') + H_2$	see Figure 1 of reference	5
a8	H <sub>2</sub> -He CIA	$H_2(v, J) + He + \gamma \rightarrow H_2(v', J') + He$	see Figure 2 of reference	5
a9	D bound-free	$D + \gamma \rightarrow D^+ + e$	same as a1	6
a10	HD <sup>+</sup> bound-free	$HD^+ + \gamma \rightarrow D + H^+$	same as a4	6
a11	HD <sup>+</sup> bound-free	$HD^+ + \gamma \rightarrow D^+ + H$	same as a4	6
a12	D <sup>-</sup> bound-free	$D^- + \gamma \rightarrow D + e$	same as a3	7
s1	H Rayleigh	$H + \gamma \rightarrow H + \gamma'$	$5.799 \times 10^{-29} \lambda^{-4} + 1.422 \times 10^{-30} \lambda^{-6} + 2.784 \times 10^{-32} \lambda^{-8}$	8
s2	Tomson	$e + \gamma \rightarrow e + \gamma'$	$6.65 \times 10^{-25}$	1

**Table B.1:** a1-a8, s1, and s2 are considered in Omukai 2001. REFERENCES-(1) Rybicki & Lightman 1979; (2) Osterbrock 1989; (3) John 1988; (4) Stancil 1994; (5) Borysow, Jorgensen, & Zheng 1997; (6) Galli & Palla 1998; (7) Frolov 2004; (8) Kurucz 1970.

In the following subsections, we describe how to calculate emissivity and opacity with cross section.

### B.4.1 Bound-Free Absorption and Free-bound Emission(a1 – a4, a9 – a12)

We consider the radiative association RA(*i*) of species *A* and *B* into *i*th state of *C*, whose binding energy is  $h\nu_i$ , and resulting free-bound emission,

$$\text{RA}(i) : A + B \rightarrow C(i) + h\nu, \quad (\text{B.17})$$

and its inverse reaction PD(*i*). The cross section of this (and its inverse) reaction is  $\sigma_{\text{RA}i}$  ( $\sigma_{\text{PD}i}$ ).

From the Milne reaction,

$$\sigma_{\text{RA}i} = \sigma_{\text{PD}i} \left( \frac{h\nu}{m_r c\nu} \right)^2 \frac{2g_{Ci}}{z_A z_B}, \quad (\text{B.18})$$

where  $m_r = m_A m_B / m_C$  is reduced mass,  $z_A$  ( $z_B$ ) is the partition function of *A* (*B*, respec-

tively),  $g_{Ci}$  is the statical weight of the  $i$ th state of  $C$ , and

$$\frac{1}{2}m_r v^2 = h(\nu - \nu_i). \quad (\text{B.19})$$

We consider the energy emission over all the azimuth angle;

$$4\pi\eta_{RAi}(\nu)d\nu = h\nu\sigma_{RAi}n(A)n(B)vf(v)dv, \quad (\text{B.20})$$

where the distribution function of the relative velocity between particles  $A$  and  $B$ ,  $f(v)$ , is given by

$$f(v) = 4\pi\left(\frac{m_r}{2\pi k_B T}\right)^{3/2} \exp\left(-\frac{m_r v^2}{2k_B T}\right)v^2. \quad (\text{B.21})$$

Thus, we have the emissivity of  $RA(i)$ ,

$$\eta_{RAi} = \frac{h\nu}{4\pi}\sigma_{RAi}n(A)n(B)vf(v)\frac{dv}{d\nu} \quad (\text{B.22})$$

$$= \frac{2h\nu^3}{c^2} \frac{g_{Ci}}{z_A z_B} \left(\frac{h^2}{2\pi m_r k_B T}\right)^{3/2} \sigma_{PDi} \exp\left[-\frac{h(\nu - \nu_i)}{k_B T}\right] n(A)n(B). \quad (\text{B.23})$$

The opacity of  $PD(i)$  is given by

$$\kappa_{PDi}(\nu) = \sigma_{PDi}n_i(C) - \frac{c^2}{2h\nu^3}\eta_{RAi} \quad (\text{B.24})$$

$$= \sigma_{PDi}n_i(C) - \frac{g_{Ci}}{z_A z_B} \left(\frac{h^2}{2\pi m_r k_B T}\right)^{3/2} \sigma_{PDi} \exp\left[-\frac{h(\nu - \nu_i)}{k_B T}\right] n(A)n(B). \quad (\text{B.25})$$

The second term in above equation represents the induced emission.

Summing over all levels, we have the emissivity and opacity owing to the reaction



and its inverse reaction  $PD$ ,

$$\eta_{RA}(\nu) = \sum_i \eta_i(\nu) \quad (\text{B.27})$$

$$= \frac{2h\nu^3}{c^2} \sigma_{PD}^* n(C) \exp\left(-\frac{h\nu}{k_B T}\right) \left[ K(T)^{-1} \frac{n(A)n(B)}{n(C)} \right], \quad (\text{B.28})$$

and

$$\kappa_{\text{PD}}(\nu) = \sum_i \kappa_i(\nu) \quad (\text{B.29})$$

$$= \sigma_{\text{PD}} n(C) \left\{ 1 - \exp\left(-\frac{h\nu}{k_B T}\right) \left[ \frac{\sigma_{\text{PD}}^*}{\sigma_{\text{PD}}} K(T)^{-1} \frac{n(A)n(B)}{n(C)} \right] \right\}, \quad (\text{B.30})$$

where  $K(T)$  is the equilibrium constant

$$K(T) \equiv \left[ \frac{n(A)n(B)}{n(C)} \right]^* = \frac{z_A z_B}{z_C} \left( \frac{2\pi m_r k_B T}{h^2} \right)^{3/2} \exp\left(-\frac{h\nu_1}{k_B T}\right), \quad (\text{B.31})$$

and

$$\sigma_{\text{PD}} = \sum_i c_i \sigma_{\text{PD}i}, \quad \sigma_{\text{PD}}^* = \sum_i c_i^* \sigma_{\text{PD}i}. \quad (\text{B.32})$$

The relative population of level  $i$  is  $c_i = n_i(C)/n(C)$ , and its LTE value is  $c_i^* = g_{Ci} \exp[-h(\nu_1 - \nu_i)/k_B T]/z_C$ .

### B.4.2 Free-Free Absorption/Emission (a5, a6)

We consider the free-free emission and absorption,



The absorption cross section for  $A$  is  $\sigma_{\text{FF}}$ , and  $\sigma_{\text{FF}} \propto n(e)$  (see Table B.1). Since this process is collisional, it occurs at LTE rate. Thus, we have

$$\eta_{\text{FF}}(\nu) = \frac{2h\nu^3}{c^2} \sigma_{\text{FF}} n(A) \exp\left(-\frac{h\nu}{k_B T}\right), \quad (\text{B.34})$$

and

$$\kappa_{\text{FF}}(\nu) = \sigma_{\text{FF}} n(A) \left[ 1 - \exp\left(-\frac{h\nu}{k_B T}\right) \right]. \quad (\text{B.35})$$

### B.4.3 H<sub>2</sub> Collision-Induced Absorption/Emission(a7, a8)

We consider H<sub>2</sub> collision induced absorption,



The absorption cross section for H<sub>2</sub> is  $\sigma_{\text{CI}}$ . This process occurs only at such a high density that  $\sigma_{\text{CI}} = \sigma_{\text{CI}}^*$ . Then, in the same way as B.4.2,

$$\eta_{\text{CI}}(\nu) = \frac{2h\nu^3}{c^2} \sigma_{\text{CI}} n(\text{H}_2) \exp\left(-\frac{h\nu}{k_B T}\right), \quad (\text{B.37})$$

and

$$\kappa_{\text{CI}}(\nu) = \sigma_{\text{CI}} n(\text{H}_2) \left[1 - \exp\left(-\frac{h\nu}{k_B T}\right)\right]. \quad (\text{B.38})$$

### B.4.4 Scattering(s1, s2)

We consider the scattering,



The scattering cross section is  $\sigma_{\text{SC}}(\nu)$ . The opacity is given by

$$\kappa_{\text{SC}}(\nu) = \sigma_{\text{SC}}(\nu) n(A). \quad (\text{B.40})$$

## Appendix C

# The effect of radiative transfer in the uniform filamentary cloud

In this appendix, we introduce the solution of transfer equation in the uniform filamentary cloud according to Susa et al. (1996).

The transfer equation along the  $s$ -direction is given by

$$\frac{dI_\nu}{ds} = -k_\nu I_\nu + j_\nu, \quad (\text{C.1})$$

where  $I_\nu$  is the intensity of radiation,  $k_\nu$  is the opacity, and  $j_\nu$  is the volume emissivity. The transfer equation is formally integrated,

$$I_\nu(\tau_\nu) = I_\nu(0)e^{-\tau_\nu} + \int_0^{\tau_\nu} e^{-(\tau_\nu - \tau')} S_\nu(\tau') d\tau', \quad (\text{C.2})$$

where

$$S_\nu \equiv \frac{j_\nu}{k_\nu} \quad (\text{C.3})$$

is source function and

$$\tau \equiv \int^s k_\nu ds \quad (\text{C.4})$$

is optical depth. If the filamentary cloud is uniform,  $k_\nu$ ,  $j_\nu$ , and  $S_\nu$  must be spatially constant. Then Eq.(C.2) is simplified,

$$I_\nu(\tau_\nu) = S_\nu + e^{-\tau_\nu} \{I_\nu(0) - S_\nu\}. \quad (\text{C.5})$$

If the filamentary cloud can be approximated as infinitely long cylinder, we can calculate the cooling rate per unit volume  $\Lambda_{\text{rad}}(\nu)$ . The energy flux,

$$F_\nu = \int d\Omega I_\nu(\theta, \phi) \cos \theta, \quad (\text{C.6})$$

is written in case of the cylinder as

$$\begin{aligned} F_\nu &= S_\nu \left\{ \pi - \int_0^{2\pi} d\phi \int_0^{\pi/2} d\theta \sin \theta \cos \theta \exp\left(-\frac{2k_\nu R \cos \theta}{\cos^2 \theta + \sin^2 \theta \sin^2 \phi}\right) \right\} \\ &= S_\nu f(2k_\nu R), \end{aligned} \quad (\text{C.7})$$

where  $R$  is the radius of the cylinder and

$$f(x) = \begin{cases} 2\pi \left(x - \frac{2}{3}x^2\right) & x < 0.01 \\ \text{dex}[0.40793 + 0.308611 \log_{10} x - 0.344113(\log_{10} x)^2 \\ \quad + 0.0673944(\log_{10} x)^3 + 0.057328(\log_{10} x)^4] & 0.01 \leq x \leq 10 \\ \pi & 10 < x. \end{cases} \quad (\text{C.8})$$

This equation is obtained by fitting the numerically integrated solution. The cooling function is given by

$$\Lambda_{\text{rad}}(\nu) = \frac{(\text{Area})}{(\text{Volume})} F_\nu = \frac{2\pi R}{\pi R^2} F_\nu = \frac{2F_\nu}{R}. \quad (\text{C.9})$$

Now, we know the expression of  $\Lambda_{\text{rad}}(\nu)$ . Thus, we can calculate the cooling rate by integrating Eq.(C.9). For example, the cooling rate of  $\text{H}_2$  cooling is given by

$$\Lambda_{\text{rad}} = \sum_{i,j} \Lambda_{\text{rad}}(\nu_{i,j}) 2\Delta\nu_D f, \quad (\text{C.10})$$

where  $i$  and  $j$  denote the rotational and vibrational levels,  $\Delta\nu_D$  is the Doppler width. Although the Doppler broadening is expressed by gaussian  $e^{-(\nu/\Delta\nu_D)^2}$  in practice, we approximate integral value of gaussian by  $2\Delta\nu_D f$ . The factor  $f$  is set to unity since it is always close to unity.

# Appendix D

## Mean intensity of the external radiation

In this appendix, we summarize estimation of the mean intensity of Far-UV radiation at  $z = 10$  by Dijkstra et al. (2008) (hereafter D08).

### D.1 Model

The average number  $N(m, r)dmdr$  of haloes within the mass range  $m \pm dm/2$  that populate a surrounding spherical shell of physical radius  $r$  and thickness  $dr$ , is given by

$$N(m, r)dmdr = 4\pi r^2 dr (1+z)^3 \frac{dn_{\text{ST}}(m, z)}{dm} dm [1 + \xi(M, m, z, r)]. \quad (\text{D.1})$$

Here  $dn_{\text{ST}}(m, z)/dm$  is the Press-Schechter mass function with the modification of Sheth et al. (2001), which gives the number density of haloes which have mass  $m$  in units of comoving  $\text{Mpc}^{-3}$ . The factor  $(1+z)^3$  converts the number density of haloes into proper  $\text{Mpc}^{-3}$ . The quantity  $\xi(M, m, z, r)$  denotes two-point correlation function, which gives the excess probability of finding a halo of mass  $m$  at distance  $r$  from the central halo. Since the high end tail of  $\xi$  makes big impact of probability distribution of radiation, D08 used the analytic formulation

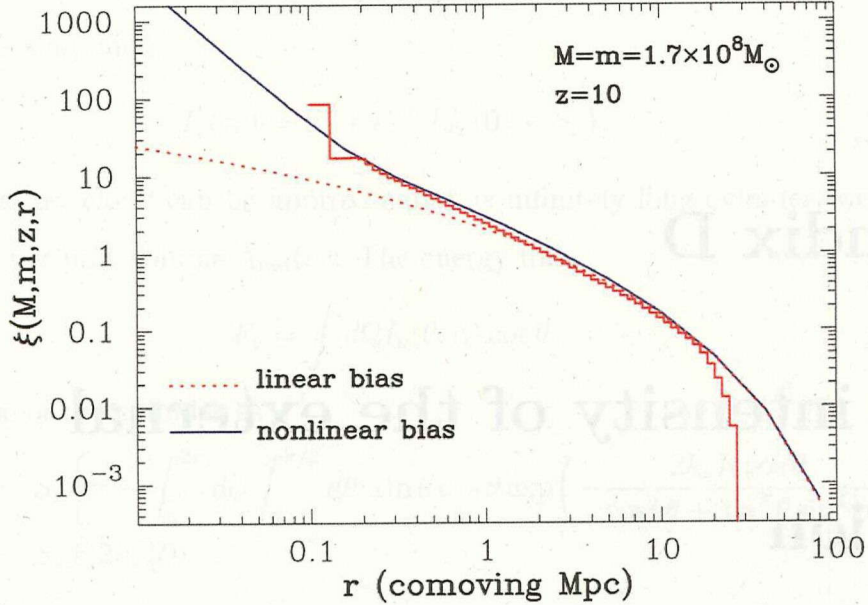


**Figure D.1:** Two-point correlation function  $\xi(M, m, z, r)$  is shown for redshift  $z = 10$  and halo masses  $M = m = 1.7 \times 10^8 M_\odot$ . The solid (dashed) line shows  $\xi(M, n, z, r)$  obtained using the non-linear (linear) bias formalism according to Iliev et al. (2003) (Scannapieco & Barkana 2002). This figure is taken from D08.

of non-linear Eulerian bias (Iliev et al. 2003; see Figure D.1)

For UV luminosity of a halo, D08 adopted the empirical relation  $L_{\text{LW}} \sim 8 \times 10^{27} \dot{M}_* \text{erg s}^{-1}$  (Kennicutt 1998), where  $\dot{M}_*$  is star formation rate in the halo in units of  $M_\odot \text{yr}^{-1}$ . The goal of D08 is to estimate mean intensity of UV radiation at  $z = 10$ . However, the star formation rate at  $z = 10$  is uncertain. D08 used the star formation rate at  $z = 6$ , which is estimated by observations. Hence, D08 used the best constrains on the star formation rate at which 10% of all halos form stars which have mass of 0.1 of the total mass of a halo over their duty cycle of  $0.1 t_{\text{Hubble}}$ . Thus, we have

$$\dot{M}_* \sim \frac{0.1m}{0.1t_{\text{Hubble}}} = \frac{1}{54} \left( \frac{m}{10^8 M_\odot} \right) \left( \frac{1+z}{1+10} \right)^{-3/2} \quad (\text{D.2})$$

Then, we have

$$\langle L_{\text{LW},26} \rangle (m) = 2.8 \left( \frac{m}{10^8 M_\odot} \right) \left( \frac{1+z}{1+10} \right)^{-3/2} \quad (\text{D.3})$$

where  $L_{\text{LW},26} = L/10^{26} \text{erg s}^{-1}$  and 'LW' denotes Lyman-Werner band<sup>1</sup>. D08 assumed lognormal distribution  $P(\log_{10} L_{\text{LW},26}, m)$  of UV luminosity, whose average is set to  $\langle L_{\text{LW},26} \rangle$ . The probability that a halo of mass  $m$  has UV luminosity in the range  $\log_{10} L_x \pm d \log_{10} L_x/2$  ('x' denotes 'LW, 26') is given by

$$P(\log_{10} L_x, m) d \log_{10} L_x = \frac{d \log_{10} L_x}{\sigma_x \sqrt{2\pi}} \exp \left[ -\frac{(\log_{10} L_x - \log_{10} [0.38 \langle L_x \rangle])^2}{2\sigma_x^2} \right], \quad (\text{D.4})$$

where  $\sigma_x$  is dispersion set to 0.5<sup>2</sup>.

Whether or not halo shines is determined by whether or not the following inequality is satisfied :

$$R \equiv \int_{-\infty}^{\log_{10} L_x(m_i)} P(u, m_i) du \geq 0.1, \quad (\text{D.5})$$

where the number 0.1 originates in how massive a halo uses mass to form stars.

## D.2 The UV flux at a halo

Using prescription of the previous section, we can calculate the LW flux that is seen from 'a halo' with

$$J_{\text{LW}} = \frac{1}{4\pi} \sum_{i=1}^{N_m} \sum_{j=1}^{N_r} \sum_{k=1}^{N(m_i, r_j)} \frac{L_{\text{LW},k}(m_i)}{4\pi r_j^2} \Delta(R - 0.1), \quad (\text{D.6})$$

where  $\Delta(x)$  is heavy-side step function. The symbol  $J_{\text{LW}}$  is the mean intensity of the radiation from the surrounding halos to the central halo. D08 repeated Monte Carlo calculation  $N_m$  times to derive the accurate probability distribution function of the mean intensity. Figure

<sup>1</sup>Photon in Lyman-Werner band dissociates H<sub>2</sub>.

<sup>2</sup>The factor 0.38 is determined in order to reproduce the observed  $z = 6$  UV luminosity function.

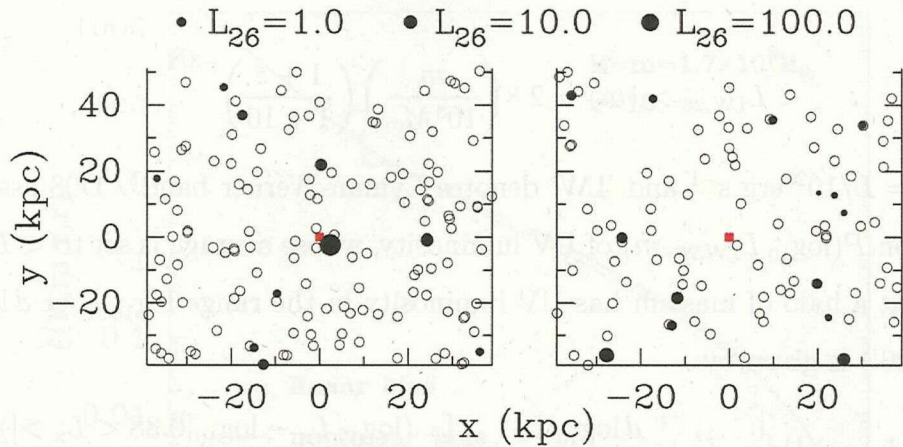


**Figure D.2:** Two realizations of the environment of a  $M = 4 \times 10^7 M_{\odot}$  halo at  $z = 10$ . The central halo is represented by the filled square at  $x = y = 0$ pc. Open circles denote surrounding halos that are not forming stars. Solid circles denote halos that are forming stars. This figure is taken from D08.

D.2 shows the examples of realizations of environment of  $M = 4 \times 10^7 M_{\odot}$  halo at  $z = 10$ . The left/right panel in Figure D.2 shows large ( $J_{LW} = 10^3$ )/average ( $J_{LW} = 6.5$ ) mean intensity situation. When mean intensity is large, the shining halo exists near the central halo.

### D.3 Results

D08 set  $M = m_{\min} = 4 \times 10^7 M_{\odot}$ ,  $r_{\min} = 2r_{\text{vir}}$  in order for halos not to bump against each other, and  $r_{\max} = 18$  proper Mpc over which the light leaves Lyman-Werner band due to Doppler shift. Moreover, D08 took into account absorption of photon by inter galactic matter and the light which enter the LW band due to Doppler shift. In other words, D08 took into account radiative transfer.

Figure D.3 shows the probability distribution function with/without radiative transfer (dashed/solid line). The most probable mean intensity with radiative transfer is very dif-

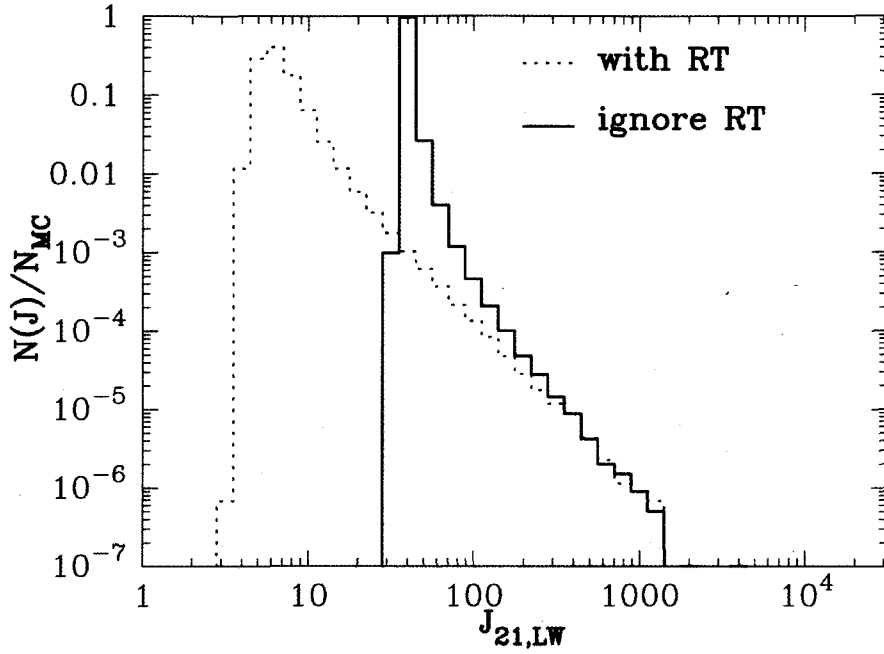


**Figure D.3:** The probability distribution function of the mean intensity of the Lyman-Werner band. The solid/dashed line shows probability distribution function without/with radiative transfer. This figure is taken from D08.

ferent from that without radiative transfer. This is because distant halos contribute to the most probable mean intensity. On the other hand, the probability of large mean intensity ( $J_{LW} = 10^3$ ) is almost same as that without radiative transfer since a single near halo mainly contributes to the mean intensity.



# Appendix E

## The integral value of Eq.(2.15)

The integrated value of Eq.(2.15) can be approximated by

$$S(x) = \begin{cases} 4\pi & x < 0.01 \\ -4.10915x^3 + 12.579x^2 - 17.5787x + 12.5392 & 0.01 < x < 1 \\ 3.48330x^{-0.398517x-0.884854} & 1 < x < 5 \\ 7.57551x^{-0.264805x-1.93051} & 5 < x < 10 \\ 18.3238x^{-0.236295x-0.258468} & 10 < x < 20 \\ 48.3927x^{-0.213846x-3.28825} & 20 < x < 30 \\ 54.4202x^{-0.202620x-3.61369} & 30 < x < 40 \\ 54.8962x^{-0.201651x-0.361636} & 40 < x \end{cases} \quad (\text{E.1})$$

where  $x \equiv k_\nu R$ . Error is smaller than 10%.



# Appendix F

## Self-shielding factor

In this appendix, we summarize estimation of the self-shielding factor  $f_{\text{sh}}$  according to Draine & Bertoldi (1996) (hereafter DB96).

DB96 defined  $N$  rovibrational levels of  $\text{H}_2$  by the index  $l = 1, \dots, N$ . Then, the following equation is satisfied :

$$\begin{aligned} \frac{dn_l}{dt} = & Rn_{\text{H}}n(\text{H})\delta_l + \sum_{m \neq l} \left( A_{ml} + \beta_{ml} + \sum_c n_c C_{ml} \right) \\ & - n_l \sum_{m \neq l} \left( A_{lm} + \sum_c n_c C_{lm} \right) - n_l \left( \beta_{\text{diss},l} + \sum_c n_c C_{\text{diss},l} \right), \end{aligned} \quad (\text{F.1})$$

where  $R$  is  $\text{H}_2$  formation rate via grain catalysis,  $\delta_l$  is the fraction of  $\text{H}_2$  in level  $l$ ,  $A_{ml}$  is Einstein  $A$ -coefficient for spontaneous decay  $m \rightarrow l$ ,  $\beta_{ml}$  is the effective rate for transition  $m \rightarrow l$  via ultraviolet pumping,  $\beta_{\text{diss},l}$  is photodissociation rate out of level  $l$ ,  $C_{ml}$  is the rate coefficient for transition  $m \rightarrow l$  due to collisions with collision partner  $c$ , and  $C_{\text{diss},l}$  is the rate coefficient for collisional dissociation out of level  $l$ . It is convenient to define the diagonal

elements  $A_{ll}$ ,  $\beta_{ll}$ , and  $C_{ll}$  to be

$$A_{ll} \equiv - \sum_{m \neq l} A_{lm}, \quad (\text{F.2})$$

$$\beta_{ll} \equiv - \sum_{m \neq l} \beta_{lm} - \beta_{\text{diss},l}, \quad (\text{F.3})$$

$$C_{ll} \equiv - \sum_{m \neq l} C_{lm} - C_{\text{diss},l}. \quad (\text{F.4})$$

Then, Eq.(E.1) becomes

$$\frac{dn_l}{dt} = Rn_{\text{H}}n(\text{H})\delta_l + \sum_m D_{ml}n_m, \quad (\text{F.5})$$

where

$$D_{ml} \equiv A_{ml} + \beta_{ml} + \sum_c n_c C_{ml}. \quad (\text{F.6})$$

DB96 assumed plane-parallel geometry with UV radiation propagating in the  $+x$  direction. The UV intensity at  $x = 0$  is specified by the parameter,

$$\chi \equiv \frac{(\lambda u_{\lambda})_{1000\text{\AA}}}{4 \times 10^{-14} \text{erg cm}}. \quad (\text{F.7})$$

At each point DB96 assumed equilibrium between  $\text{H}_2$  formation on grains<sup>1</sup> and  $\text{H}_2$  photodissociation. DB96 defined

$$y_l \equiv \frac{2n_l}{n_{\text{H}}} \quad (\text{F.8})$$

and required  $\dot{y}_l = 0$  (i.e.,  $dn_l/dt = 0$ ; detailed balance). Since  $n(\text{H}) = n_{\text{H}}(1 - x_{\text{H}} - \sum_{l=1}^N y_l)$ , the vector  $y_l$  satisfy the system of  $N$  inhomogeneous equations

$$\sum_{m=1}^N (2Rn_{\text{H}}\delta_l - D_{ml})y_m = 2Rn_{\text{H}}(1 - x_{\text{H}})\delta_l. \quad (\text{F.9})$$

This equations is equivalent to  $dn_l/dt = 0$ . DB96 solved this equation and estimated total photodissociation rate.

<sup>1</sup>In the primordial cloud, we assume  $\text{H}_2$  formation owing to collisional reaction.

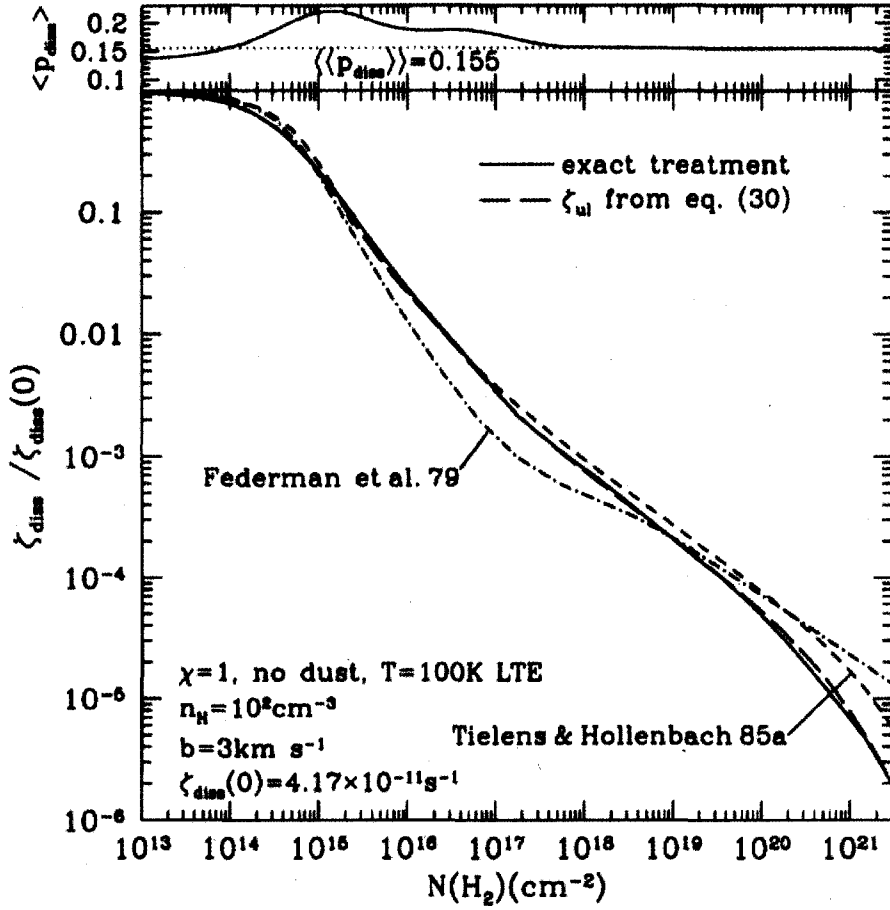


**Figure F.1:** Ratio of the total dissociation rate via UV pumping to that in the cloud without extinction of photon by  $\text{H}_2$  dissociation for  $T = 100\text{K}$  LTE level populations.  $\text{H}_2$  is assumed to have a Doppler broadening parameter  $b = 3\text{km s}^{-1}$ . This figure is taken from DB96.

Figure E.1 shows the ratio of the total dissociation rate via UV pumping to that in the cloud without extinction of photon by  $\text{H}_2$  dissociation. The ratio is nearly unity up to the column density  $N_{\text{H}_2} \sim 10^{14}\text{cm}^{-2}$  and is proportional to  $N_{\text{H}_2}^{-3/4}$  at the column density higher than  $10^{14}\text{cm}^{-2}$ . Thus, the self-shielding factor  $f_{\text{sh}}$  is defined as,

$$f_{\text{sh}} = \min \left[ 1, \left( \frac{N_{\text{H}_2}}{10^{14}\text{cm}^{-2}} \right)^{-3/4} \right]. \quad (\text{F.10})$$



# Appendix G

## Test of numerical code for one-dimensional hydrodynamical calculations

In this appendix, we check the numerical code used for calculation in this paper.

We solve equation of motion in the second-order-accurate finite-difference scheme with the artificial viscosity (Richtmyer & Morton 1967). We calculate in the same way as Thoul & Weinberg (1995), except for cylindrical geometry. To check accuracy of our code, first, we calculate the density distribution of isothermal equilibrium filamentary cloud ( $T = 300\text{K}$ ) with 100 and 200 meshes, and fixed time step. Drag term  $-2v(r)/dt$  is added to equation of motion and is eliminated after the step number reaches 125 for case with 100 meshes and 250 for case with 200 meshes. After 250 steps (100 meshes) and 500 steps (200 meshes), we have error of density distribution shown in figure G.1. Error for case with 100 meshes is 4 times of error for case with 200 meshes. Hence, our code is second-order-accurate in space.

Second, we check temporal accuracy of our code in time. We calculate collapse of pressure-

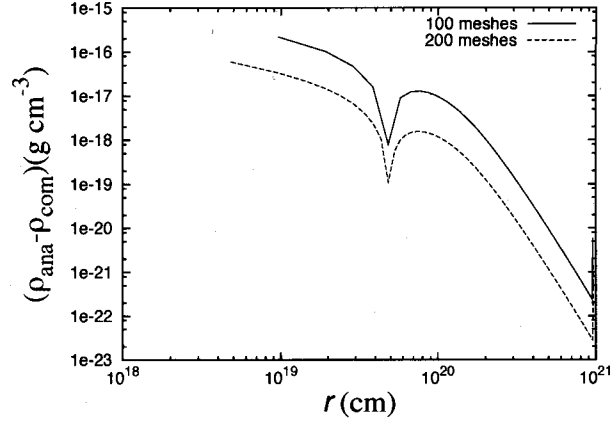


**Figure G.1:** Error of density distribution of isothermal equilibrium filamentary cloud ( $T = 300\text{K}$ ) for the numerical results with 100 meshes and 200 meshes. The symbol  $\rho_{\text{ana}}$  is analytic solution, and  $\rho_{\text{com}}$  is numerical results.

less uniform filamentary cloud in free-fall state. Analytic solution is given by

$$\int_0^{\sqrt{-\log F(t)}} e^{-x^2} dx = \sqrt{\pi G \rho(0) t}, \quad (\text{G.1})$$

where  $F(t) = r(t)/r(0)$ ,  $\rho(0)$  is the initial density. Time step is set to be  $\Delta t = 10^{-4} t_{\text{ff}}(t = 0)$  and  $2\Delta t$ . Calculation is continued until the density becomes 100 times of the initial density. In the case with  $\Delta t$ ,  $F$  at the end of calculation is 0.0913290. In the case with  $2\Delta t$ ,  $F$  at the end of calculation is 0.09132307. Analytic solution predicts  $F = 0.9132284$ . Error with  $2\Delta t$  is 4 times larger than  $\Delta t$ . Hence, our code has second-order-accuracy in time.

# Appendix H

## Self-shielding function of Wolcott-Green et al. (2011)

Wolcott-Green et al. (2011) have recently suggested self-shielding function indicated by three-dimensional radiative transfer. In this appendix, we investigate dependence of fragment mass on the self-shielding function quantitatively. The new self-shielding function is given by,

$$f_{\text{sh,WG}} = \frac{0.965}{(1 + x/b_5)^{1.1}} + \frac{0.035}{(1 + x)^{0.5}} \exp[-8.5 \times 10^{-4}(1 + x)^{0.5}], \quad (\text{H.1})$$

where

$$x \equiv \frac{N_{\text{H}_2}}{5 \times 10^{14} \text{cm}^{-2}}, \quad (\text{H.2})$$

and

$$b_5 \equiv \frac{b}{10^5 \text{cm/s}} = \frac{1}{10^5 \text{cm/s}} \sqrt{\frac{2k_B T}{\mu m_{\text{H}}}}. \quad (\text{H.3})$$

Since  $f_{\text{sh,WG}}$  is 1 – 10 times larger than original  $f_{\text{sh}}$  (Eq.2.16), Wolcott-Green et al. (2011) suggested that the effect of photodissociation is actually stronger than the result with  $f_{\text{sh}}$ . Thus, the results which we have ever considered are expected to be modified quantitatively.

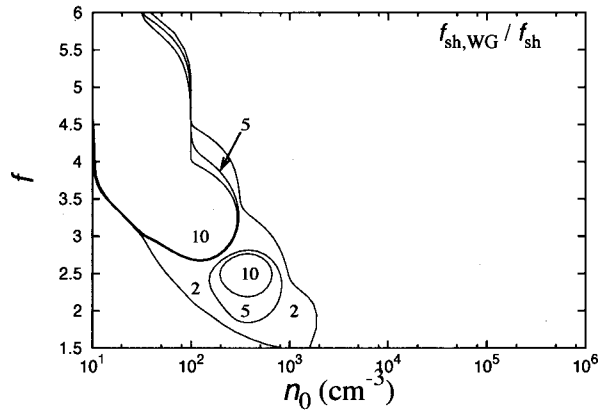


**Figure H.1:** The ratio of the fragment mass with  $f_{\text{sh,GW}}$  to that with  $f_{\text{sh}}$  in the case with  $J_{21} = 10$ . The number near each solid line is the ratio of fragment mass.

To see the difference between shielding function, we calculate fragment mass using  $f_{\text{sh,GW}}$  in the case with  $J_{21} = 10$ . Figure H.1 shows the ratio of fragment mass between the cases with  $f_{\text{sh,GW}}$  and with  $f_{\text{sh}}$ . When we use  $f_{\text{sh,GW}}$ , fragment mass increases compared with the case with  $f_{\text{sh}}$  especially for the cases with  $n_0 = 10 - 10^3 \text{ cm}^{-3}$  and  $f \geq 2$ . This feature is consistent with the relation,  $f_{\text{sh,GW}} \geq f_{\text{sh}}$ .

# Appendix I

## Virial equation for uniform sphere

In this appendix, we investigate virial equation for uniform sphere. We multiply  $4\pi r^3$  by both hands of equation of motion,

$$\rho \frac{Dv}{Dt} = -\frac{dP}{dr} - \frac{GM}{r^2} \rho, \quad (\text{I.1})$$

and integrate over  $r$ . Then, the left side hand of equation (I.1) is

$$\begin{aligned} \int 4\pi r^3 \rho \frac{Dv}{Dt} dr &= \int r \frac{Dv}{Dt} dM \\ &= \int \left( \frac{1}{2} \frac{D^2}{Dt^2} r^2 - v^2 \right) dM \\ &= \frac{1}{2} \frac{D^2}{Dt^2} \int r^2 dM - \int v^2 dM. \end{aligned} \quad (\text{I.2})$$

About the first term of right side hand of equation (I.2),

$$\begin{aligned} \int r^2 dM &= \int 4\pi r^4 \rho dr \\ &= \frac{4\pi \rho}{5} R^5 \\ &= \frac{3}{5} MR^2, \end{aligned} \quad (\text{I.3})$$

and

$$\begin{aligned}\frac{1}{2} \frac{D^2}{Dt^2} \int r^2 dM &= \frac{1}{2} \frac{D^2}{Dt^2} \left( \frac{3}{5} MR^2 \right) \\ &= \frac{3}{5} M \left( \frac{DR}{Dt} \right)^2 + \frac{3}{5} MR \frac{D^2 R}{Dt^2}.\end{aligned}\quad (\text{I.4})$$

About the second term,

$$\begin{aligned}\int v^2 dM &= \int 4\pi r^2 \rho v^2 dr \\ &= \int 4\pi \rho r^2 \left( \frac{DR}{Dt} \right)^2 \frac{r^2}{R^2} dr \\ &= \frac{4\pi \rho}{5} R^3 \left( \frac{DR}{Dt} \right)^2 \\ &= \frac{3}{5} M \left( \frac{DR}{Dt} \right)^2,\end{aligned}\quad (\text{I.5})$$

where we use the following relation,

$$v = \left( \frac{DR}{Dt} \right) \frac{r}{R}, \quad (\text{I.6})$$

since velocity is in proportion to  $r$  because of uniform density. Hence, the left side hand of equation (I.2) is

$$\int 4\pi r^3 \rho \frac{Dv}{Dt} dr = \frac{3}{5} MR \frac{D^2}{Dt^2} R. \quad (\text{I.7})$$

On the other hand, about the right side hand of equation of motion, term of pressure gradient is

$$\begin{aligned}- \int 4\pi r^3 \frac{dP}{dr} dr &= \int 12\pi r^2 P dr \\ &= 3(\gamma_{\text{adi}} - 1) \frac{k_B T}{\mu m_{\text{H}}} M,\end{aligned}\quad (\text{I.8})$$

where  $\gamma_{\text{adi}}$  is adiabatic index. The second term is

$$\begin{aligned}- \int 4\pi r^3 \frac{GM}{r^2} \rho dr &= \int (4\pi \rho)^2 \frac{G}{3} r^4 dr \\ &= - \frac{(4\pi \rho)^2}{15} GR^5 \\ &= - \frac{3}{5} \frac{GM^2}{R}.\end{aligned}\quad (\text{I.9})$$

Finally, we have virial equation for uniform sphere,

$$\frac{3}{5}MR\frac{Dv}{Dt} = 3(\gamma_{\text{adi}} - 1)\frac{k_B T}{\mu m_H} \frac{1}{R} - \frac{3GM}{5R} \quad (\text{I.10})$$

$$\frac{Dv}{Dt} = \frac{10}{3} \frac{k_B T}{\mu m_H} \frac{1}{R} - \frac{GM}{R^2}, \quad (\text{I.11})$$

where we use  $\gamma_{\text{adi}} = 5/3$ .



# Bibliography

Abel, T., Anninos, P. A., Norman, M. L., & Zhang, Y., 1998, *ApJ*, 508, 518

Abel, T., Bryan, G. L., & Norman, M. L., 2000, *ApJ*, 540, 39

———, 2002, *Science*, 295, 93

Allison, A. A. & Dalgarno, A., 1969, *Atomic Data*, 1, 91

Bessho, S., & Tsuribe, T. 2012a, accepted by *PASJ* (arXiv:1203:6484)

Bessho, S., & Tsuribe, T. 2012b, accepted by *PASJ* (arXiv:1209:1898)

Bromm, V., Coppi, P. S., & Larson, R. B., 1999, *ApJ*, 527, L5

———, 2002, *ApJ*, 564, 23

Bromm, V., & Loeb, A., 2003, *ApJ*, 596, 34

Bron, J., Chang, F. C., & Wolfsberg, M., 1973, *Zeitschrift für Naturforschung. A, Astrophysik, Physik und Physikalische Chemie*, 28, 129

Borysow, A., Jorgensen, U. G., & Zheng, C., 1997, *A&A*, 324, 185

Castor, J. I. 1970, *MNRAS*, 149, 111

Dijkstra, M., Haiman, Z., Mesinger, A., & Whythe, J. S. B., 2008, *MNRAS*, 391, 1961

- Draine, B. T., & Bertoldi, F., 1996, *ApJ*, 468, 269
- Flower, D. R., 2002, *MNRAS*, 333, 763
- Frolov, M. A., 2004, *J.Phys.B:At.Mol.Opt.Phys.*, 37, 853
- Galli, D., & Palla, F., 1998, *A & A*, 335, 403
- Greif, T. H., Johnson, J. L., Klessen, R. S., Bromm, V., 2008, *MNRAS*, 387, 1021
- Haiman, Z., Rees, J. M., & Loeb, A., 1997, *ApJ*, 476, 458
- Hasegawa, K., Umemura, M., & Susa, H., 2009a, *MNRAS*, 395, 1280
- Hasegawa, K., Umemura, M., & Kitayama, T., 2009b, *MNRAS*, 397, 1338
- Heger, A., Fryer, C. L., Woosley, S. E., Langer, N., & Hartmann, D. H., 2003, *ApJ*, 591, 288
- Iliev, I. T., Scannapieco, E., Martel, H., & Shapiro, P. R. 2003, *MNRAS*, 341, 81
- Inutsuka, S., & Miyama, M. S., 1992, *ApJ*, 388, 392
- , 1997, *ApJ*, 480, 681
- Izotov, Yu., & Thuan, T. X., 1998, *ApJ*, 500, 188
- John, T. L., 1988, *A&A*, 193, 189
- Kitayama, T., Yoshida, N., Susa, H., & Umemura, M. 2004, *ApJ*, 613, 631
- Kurucz, R. L., 1970, *Smithsonian Observatory Special Report* 309
- Larson, R. B., 1969, *MNRAS*, 145, 271
- Larson, R. B., 1985, *MNRAS*, 214, 379
- Miyama, M. S., Narita, S., & Hayashi, C., 1987a, *Prog.Theor.Phys.*, 78, 1051

- Miyama, M. S., Narita, S., & Hayashi, C., 1987b, *Prog.Theor.Phys.*, 78, 1273
- Nagasawa, M., 1987, *Prog.Theor.Phys.*, 77, 635
- Nakamura, F., Hanawa, T., & Nakano, T. 1993, *PASJ*, 45, 551
- Nakamura, F., & Umemura, M., 1999, *ApJ*, 515, 239
- ., 2001, *ApJ*, 548, 19
- ., 2002, *ApJ*, 569, 549
- O'Meara, J. M., Tytler, D., Kirkman, D., Suzuki, N., Prochaska, J. X., Lubin, D., & Wolfe, A. M., 2001, *ApJ*, 552, 718
- Omukai, K., 2001, *ApJ*, 546, 635
- Omukai, K., & Nishi, R., 1998, *ApJ*, 508, 141
- ., 1999, *ApJ*, 518, 64
- Omukai, K., & Yoshii, Y., 2003, *ApJ*, 599, 746 (OY03)
- Osterbrack, D. E., 1989, *Astrophysics of Gaseous Nebulae and Active Galactic Nuclei* (Mill Valley:University Science Books)
- Ostriker, J., 1964, *ApJ*, 140, 1056
- Penston, M. V., 1969, *MNRAS*, 144, 425
- Press, W. H. & Schechter, P. 1974, *ApJ*, 187, 425
- Ripamonti, E., & Abel, T., 2004, *MNRAS*, 348, 1019
- Rybicki, G. B., & Lightman, A. P., 1979, *Radiative Processes in Astrophysics* (New York:Wiley)

- Scannapiero, E., & Barkana, R. 2002, *ApJ*, 571, 585
- Schaerer, D., 2002, *A & A*, 382, 28
- Stancil, P. C., 1994, *ApJ*, 430, 360
- Susa, H., 2007, *ApJ*, 659, 908
- Susa, H., Uehara, H., & Nishi, R., 1996, *Prog.Theor.Phys*, 96, 1073
- Susa, H., Umemura, M., & Hasegawa, K., 2009, *ApJ*, 702, 480
- Tegmark, M., Silk, J., Rees, J. M., Blanchard, A., Abel, T., & Palla, F., 1997, *ApJ*, 474, 1
- Thoul, A. A., & Weinberg, D. H. 1995, *ApJ*, 442, 480
- Tsuribe, T., & Inutsuka, S., 1999, *ApJ*, 526, 307
- Uehara, H., Susa, H., Nishi, R., Yamada, M., & Nakamura, T., 1996, *ApJ*, 473, L95
- Uehara, H., & Inutsuka, S., 2000, *ApJ*, 531, L91
- Whalen, D., Abel, T., & Norman, L. M., 2004, *ApJ*, 610, 14
- Wolcott-Green, J., Haiman, Z., & Bryan, G. L. 2011, *MNRAS*, 418, 838
- Yoshida, N., Omukai, K., & Hernquist, L., 2008, *Science*, 321, 669
- Yoshida, N., Omukai, K., Hernquist, L., & Abel, T., 2006, *ApJ*, 652, 6

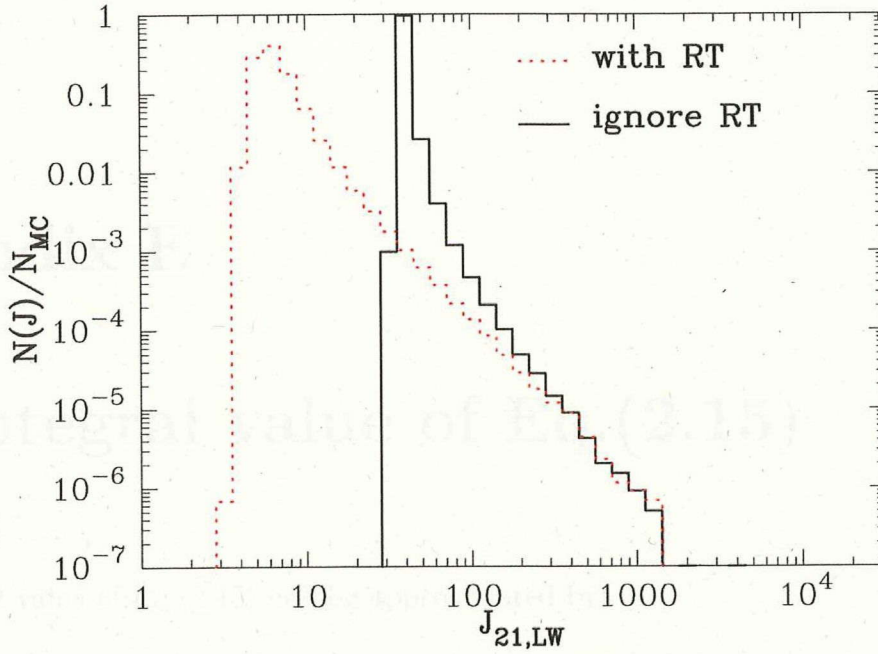


**Figure D.3:** The probability distribution function of the mean intensity of the Lyman-Werner band. The solid/dashed line shows probability distribution function without/with radiative transfer. This figure is taken from D08.

ferent from that without radiative transfer. This is because distant halos contribute to the most probable mean intensity. On the other hand, the probability of large mean intensity ( $J_{\text{LW}} = 10^3$ ) is almost same as that without radiative transfer since a single near halo mainly contributes to the mean intensity.